Coherent control of electron spins in diamond for quantum information science and quantum sensing

by

Alexandre Cooper-Roy

B.Eng., École Polytechnique de Montréal (2008)
Ingénieur Polytechnicien, École Polytechnique (2009)
M.Eng., The University of Tokyo (2010)
Submitted to the Department of Nuclear Science and Engineering
in partial fulfillment of the requirements for the degree of

Doctor of Philosophy

at the

MASSACHUSETTS INSTITUTE OF TECHNOLOGY

September 2016

Author . . . .
Department of Nuclear Science and Engineering
July 22nd, 2016

Certified by . . . .
Paola Cappellaro
Associate Professor
Thesis Supervisor

Accepted by . . . .
Ju Li
Chairman, Department Committee on Graduate Theses

Coherent control of electron spins in diamond for quantum information science and quantum sensing

by

Alexandre Cooper-Roy

Submitted to the Department of Nuclear Science and Engineering
on July 22nd, 2016, in partial fulfillment of the
requirements for the degree of
Doctor of Philosophy

Abstract

This thesis introduces and experimentally demonstrates coherent control techniques to exploit electron spins in diamond for applications in quantum information processing and quantum sensing. Specifically, optically-detected magnetic resonance measurements are performed on quantum states of single and multiple electronic spins associated with nitrogen-vacancy centers and other paramagnetic centers in synthetic diamond crystals.

We first introduce and experimentally demonstrate the Walsh reconstruction method as a general framework to estimate the parameters of deterministic and stochastic fields with a quantum probe. Our method generalizes sampling techniques based on dynamical decoupling sequences and enables measuring the temporal profile of time-varying magnetic fields in the presence of dephasing noise.

We then introduce and experimentally demonstrate coherent control techniques to identify, integrate, and exploit unknown quantum systems located in the environment of a quantum probe. We first locate and identify two hybrid electron-nuclear spins systems associated with unknown paramagnetic centers in the environment of a single nitrogen-vacancy center in diamond. We then prepare, manipulate, and measure their quantum states using cross-polarization sequences, coherent feedback techniques, and quantum measurements. We finally create and detect entangled states of up to three electron spins to perform environment-assisted quantum metrology of time-varying magnetic fields. These results demonstrate a scalable approach to create entangled states of many particles with quantum resources extracted from the environment of a quantum probe. Applications of these techniques range from real-time functional imaging of neural activity at the level of single neurons to magnetic resonance spectroscopy and imaging of biological complexes in living cells and characterization of the structure and dynamics of magnetic materials.

Thesis Supervisor: Paola Cappellaro
Title: Associate Professor

Acknowledgments

This thesis has been made possible by the financial support from the Fulbright Scholar Program and the Natural Sciences and Engineering Research Council of Canada. A very special thank you goes to all of my mentors, colleagues, and friends at MIT, Harvard, and elsewhere in the world who have helped me become the person I am today.

First and foremost, Professor Paola Cappellaro has been very keen on supervising my research activities and guiding my scientific growth during my tenure within her group. Paola has provided me with a tremendous amount of freedom to explore creative approaches to identifying and solving problems in science and engineering. She has always been very open to discuss new ideas and provide feedback on my progress towards reaching my goals. Paola is a very dedicated and thoughtful mentor with an inspiring motivation to better understand the quantum world and a great ability to combine a deep understanding of theoretical concepts with insightful experimental evidences.

Professor Ju Li has provided me with many valuable advice as the chairman of the committees of both my qualifying exam and my thesis defense, including the importance of making connections with the work of others and focusing on solutions that enable discoveries and new technologies.

Professor Dirk Englund has provided me with many valuable advice about my scientific research and career goals as an academic advisor and member of my thesis committee. I very much admire the ability of Dirk to carry out collaborative research projects on multidisciplinary fronts at the confluence of scientific disciplines and thank him for providing me with such great opportunities to learn from the numerous members of his group.

Professor Ronald Walsworth from the Center for Astrophysics (CFA) at Harvard University has been an inspiring role model who taught me by example about the importance and excitement of building strong collaborative teams and tackling challenging problems at the intersection of multiple fields of research. Ron has sig-

nificantly contributed to the success of my research by encouraging me to attend his group meetings and exchange (classical) information and matter with his postdocs and students.

Professor Ed Boyden from the Media Lab at MIT has taught me through many intense discussions about the importance of maximizing impact by solving the most important problems facing humanity, identifying valuable opportunities by using a wide variety of cognitive tools, and maintaing strong collaborative ties with experts across disciplines.

Many other professors have also helped shaping my scientific growth, including Professors Lorenza Viola from Dartmouth University, Dmitry Pushin from University of Waterloo, Nir Bar-Gill from the Hebrew University of Jerusalem, and Michael Biercuk from the University of Sydney.

Second, I would like to acknowledge the help and friendship of all of the postdocs that have spent time with me discussing about Science, have taught me experimental skills and theoretical concepts, and have encouraged my quest for knowledge with key insights and pieces of equipment.

HoNam Yum has taught me valuable experimental skills in optics and electronics as we worked together on designing and building our first confocal microscope.

Easwar Magesan has cheerfully joined my efforts to work out the theory of the Walsh reconstruction method and compressed sensing approach to quantum parameter estimation. Easwar's enthusiasm for solving tough mathematical problems has positively influenced my approach to research.

Gerardo Paz-Silva from Dartmouth University has taught me a lot about noise spectroscopy and the Magnus expansion during many of our visits and video calls.

Chinmay Belthangady from Walsworth group at Harvard has spent a great deal of his time at MIT to help me set up the electronics for driving electron spins in diamond as we launched our new project on environment-assisted quantum metrology. Chinmay's positive and generous attitude has inspired me to become a better person.

Huiliang Zhang from Walsworth group at Harvard has answered many of my questions about diamond fabrication and has patterned and implanted the diamond sample in which we ended up identifying two unknown paramagnetic centers.

Many other postdocs have contributed to my theoretical and experimental research work. David Gelbwaser from Aspuru-Guzik group at Harvard has spent many hours with me discussing about quantum thermodynamics and the efficiency of quantum engines. Jean-Christophe Jaskula has taught me about super-resolution microscopy and has helped me resolving technical issues with our confocal microscope. Luca Marseglia has helped out fabricating new coplanar waveguides and acid cleaning our diamond samples. David Le Sage taught me about aligning an acousto-optic modulator in the bow-tie configuration. David Glenn has provided me with technical guidance in building our first confocal microscope and has fueled my interest in biophysics. Alexei Trifonov has helped diagnosing issues in our optical setup. Linh Pham has answered many of my questions about handling diamond samples and performing magnetometry experiments; her lablog posts have always been a great source of inspiration. Ulf Bissbort has taught me about solving algebraic expressions in spin physics using the C programming language. Kasturi Saha has helped fixing issues in our optical setup. Gurneet Kaur has provided me with great advice about recording scientific information and experimental measurements.

Third, I would like to acknowledge the friendship of my student colleagues from the Quantum Engineering Group, which have played an important role in shaping my experience at MIT.

Clarice Aiello wrote the first version of our control software and provided valuable support in designing and building our control electronics to manipulate the quantum state of single nitrogen-vacancy centers in diamond.

Masashi Hirose provided me with the source code to simulate the dynamics of confined ensembles of interacting electron spins and engaged me in many discussions about understanding new sets of experimental data.

Ashok Ajoy provided support on automating the alignment of the static magnetic field and contributed to many discussions on performing spectral measurements on ensembles of electron spins.

Ken Xuan Wei provided me with the source code to simulate the average Hamiltonian of multi-resonance pulse sequences and engaged me in many interesting discussions about many-body physics and nonequilibrium spin dynamics.

Akira Sone stimulated my interest in algebraic geometry during many interesting discussions about his projects on system identification. Calvin Sun and Mo Chen have helped me upgrading our experimental system and took over the measurements after my departure to Caltech. Yixiang Liu has helped me simulating the implantation profile of nitrogen ions in diamond. Gary Wolfowicz, Joe Smith and Scott Alsid has brought great energy to our group and positively contributed to its cohesion.

I would also like to thank my student colleagues from the Walsworth group for invaluable discussions, including Emma Rosenfeld, Paul Junghyun Lee, Erik Bauch, and Keigo Arai; my student colleagues from the Dirk's group, especially Edward Chen who helped me upgrading our confocal microscope and leading the iQuISE student program and Matt Trusheim who provided answers to my questions about diamond fabrication; Jonathan Welch from Asupuru-Guzik's group who encouraged my study of Walsh analysis; and my friends from the iQuISE leadership team, especially Kristin Beck, Zheshen Zhang, and Sara Mouradian. I would also like to thank my friends from Boston Team Handball, especially Nader Shaar who acted as a great personal mentor. Special thanks go to Laura von Bosau, Teresa Avila, Heather Barry and Clare Egan for administrative support and Kurt Broderick for technical support in the clean room.

Finally, I would like to thank my family, my parents, and my wife for their care, support, and kind devotion. Thank you very much!

Contents

1 Introduction 13

1.1 Conceptual framework 14

1.2 Outline of this thesis 15

2 Time-resolved magnetic sensing with electronic spins in diamond 17

2.1 Quantum parameter estimation with quantum probes 19

2.1.1 Understand the Walsh reconstruction method 21

2.1.2 Quantify the performance of the Walsh reconstruction method 24

2.2 Demonstrate the Walsh reconstruction method experimentally with a single nitrogen-vacancy center in diamond 34

2.2.1 Reconstruct the temporal profile of sinusoidal fields 34

2.2.2 Reconstruct the temporal profile of bichromatic fields 37

2.2.3 Reconstruct the temporal profile of arbitrary time-varying fields 38

2.3 Conclusion and outlook 42

2.3.1 Comparison with existing techniques 42

2.3.2 Applications to sensing neural activity 44

3 Spectral reconstruction of stochastic fields with Walsh sequences 47

3.1 Noise spectroscopy with single quantum probes 47

3.1.1 Discrete representation of the autocorrelation function 50

3.1.2 Continuous representation of the autocorrelation function . . . 54

4 Environment-assisted quantum metrology with entangled states of electron spins in diamond **61**
4.1 Quantum system identification 63
4.1.1 Identify two unknown paramagnetic centers in the environment of a single nitrogen-vacancy center in diamond 63
4.1.2 Estimate the parameters of the internal spin Hamiltonian of two unknown paramagnetic centers in diamond 65
4.2 Quantum system integration 74
4.2.1 Initialize quantum systems using coherent feedback control . . 74
4.2.2 Initialize quantum systems using cross-polarization 83
4.3 Quantum system exploitation 89
4.3.1 Understand entangled states of electron spins 89
4.3.2 Create and detect entangled states of two electron spins 97
4.3.3 Create and detect entangled states of three electron spins . . . 99
4.3.4 Measure magnetic fields with entangled states of electron spins 101
4.3.5 Perform repetitive quantum measurements of electron spins . 104
4.4 Conclusion and outlook 108

5 Conclusion and outlook **111**

List of Figures

1-1 Understand the conceptual framework underlying this thesis. 15

2-1 Understand the Walsh reconstruction protocol. 18
2-2 Understand the Walsh functions. 20
2-3 Simulate the reconstruction of bichromatic fields. 31
2-4 Quantify the accuracy of the Walsh reconstruction method. 32
2-5 Reconstruct sinusoidal fields with Walsh sequences. 35
2-6 Extract the Walsh coefficient from the fluorescence signal. 36
2-7 Reconstruct bichromatic fields with Walsh sequences. 37
2-8 Characterize the transmission properties of the coplanar waveguide. . 38
2-9 Simulate an action potential. 40
2-10 Reconstruct arbitrary time-varying fields with Walsh sequences. . . . 41

3-1 Represent two-dimensional Walsh filters (1). 51
3-2 Represent two-dimensional Walsh filters (2). 52
3-3 Represent the arithmetic and dyadic sampling domain. 54
3-4 Represent the autocorrelation function of a stationary process. 55
3-5 Represent the arithmetic and dyadic sampling domain. 56

4-1 Measure the resonance spectrum of two paramagnetic centers. 64
4-2 Observe from above the Terra-B diamond sample. 66
4-3 Estimate the strength and orientation of the static magnetic field. . . 69
4-4 Measure the cw-esr spectrum of an ensemble of NV centers. 70
4-5 Estimate the hyperfine components of two paramagnetic centers. . . . 70

4-6 Estimate the dipolar components of two paramagnetic centers. 72
4-7 Initialize quantum systems using coherent feedback control. 78
4-8 Initialize quantum systems using cross-polarization in the rotating frame. 84
4-9 Understand cross-polarization in the rotating frame. 85
4-10 Initialize an electron spin using Hartmann-Hahn cross-polarization. . 87
4-11 Initialize another electron spin using Hartmann-Hahn cross-polarization. 88
4-12 Create entangled states of two electron spins in diamond. 98
4-13 Detect entangled states of two electron spins in diamond. 100
4-14 Create entangled states of three electron spins in diamond. 101
4-15 Detect entangled states of three electron spins in diamond. 102
4-16 Measure magnetic fields with entangled states of two electron spins. . 103
4-17 Perform repetitive readout of a single electron spin. 105
4-18 Detect entangled states of two electron spins using repetitive readout. 107

Chapter 1

Introduction

Quantum systems composed of many interacting particles of light and matter exhibit complex dynamical properties that can be studied experimentally to better understand fundamental states of matter and design novel technologies. Coherent control techniques to prepare, manipulate, and read out the quantum state of single and multiple interacting quantum systems have been demonstrated in a vast array of physical systems, including superconducting qubits, trapped ions, quantum dots, ultracold atoms in optical lattices, electron donors in semiconductors, and spin defects in solid-state materials. Spin defects in solid-state materials are particularly promising for applications in quantum metrology and sensing; in particular, electron and nuclear spins associated with single and multiple nitrogen-vacancy (NV) centers in diamond have recently been used as quantum probes to measure the spatiotemporal profile of electric and magnetic fields associated with molecular and biological samples at the atomic scale under ambient conditions.

Quantum metrology explores quantum strategies such as the use of entanglement, discord, and squeezing to reduce the statistical error associated with the estimation of unknown physical parameters. Environment-assisted metrology exploits the environment of a quantum sensor to estimate unknown parameters with an improvement in precision beyond the limits allowed by classical strategies. Quantum strategies that outperform classical strategies have been explored in different physical implementations of a quantum probe to improve the performance of metrology tasks, including squeezed states, non-Gaussian spin states, and entangled states of many quantum particles. The creation of multipartite entangled states of electron spins in solid-state materials has been hindered, however, by the difficulty of initializing their quantum state in a state of low entropy and protecting their evolution against dephasing in the presence of environmental fluctuations.

This thesis makes significant contributions to quantum metrology in two important areas. First, we extend the framework of quantum parameter estimation to estimate deterministic and stochastic time-dependent parameters. Our approach takes advantage of the Walsh functions to generate a complete set of digital filters that efficiently sample and reconstruct time-varying fields. Second, we develop coherent control techniques to extract quantum resources from the environment of a quantum probe to create entangled states of many quantum particles and perform environment-assisted quantum metrology. These techniques are experimentally demonstrated with hybrid electron-nuclear spin systems associated with unknown paramagnetic centers located in the environment of a single nitrogen-vacancy center in diamond.

1.1 Conceptual framework

The conceptual framework underlying this thesis is the coherent control of open quantum systems for applications in quantum metrology and sensing (Fig. 1-1). Coherent control techniques are introduced to control and characterize the dynamics of open quantum systems, specifically composed of a single quantum probe interacting with an environment formed by a mesoscopic ensemble of interacting quantum particles, such as electron spins in diamond. The goal is not only to characterize the influence of the environment on the evolution of a quantum probe, but also to exploit the quantum properties of the environment in order to improve the performance of quantum metrology protocols. We introduce and experimentally demonstrate coherent control techniques to prepare, manipulate, and measure the quantum state of unknown paramagnetic centers located in the environment of a single NV center in diamond. We then convert these unknown paramagnetic centers into quantum resources useful

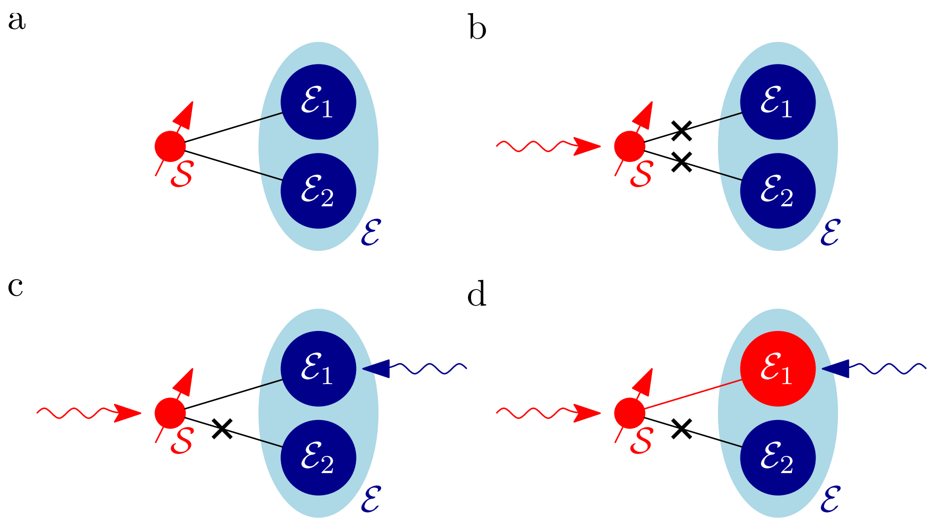

Figure 1-1: **Coherent control of open quantum systems for applications in quantum information science and quantum sensing. a,** A single quantum probe interacts with many fragments of its environment, causing the decay of coherent superposition of states and preventing interferometric measurements of time-varying fields over long periods of time. **b,** Coherent control sequences applied on the quantum probe decouple the quantum probe from its environment, increasing the lifetime of coherent superposition of states and enabling interferometric measurements of time-varying fields over long periods of time. **c,** Coherent control sequences simultaneously applied on both the quantum probe and a resonant fragment of its environment selectively recouple their mutual interaction, thus providing information about the structure and dynamics of the environment. **d,** A single quantum probe converts a fragment of its environment into quantum resources useful for creating entangled states of many particles and performing interferometric measurements of time-varying fields with improved sensitivity.

for creating entangled states of multiple electron spins and measuring time-varying fields with improved sensitivity. Performing repetitive quantum measurements of the quantum state of the electron spins provides a gain in information that balances the detrimental effects of control errors and dissipation during quantum operations and quantum evolution.

1.2 Outline of this thesis

This thesis addresses the problem of measuring deterministic and stochastic fields with single quantum probes in Chapter 2 and Chapter 3, before tackling the problem of converting unknown quantum systems into quantum resources useful for quantum sensing in Chapter 4.

Chapter 2 introduces the Walsh reconstruction method [15, 16, 17], which is a new approach to quantum parameter estimation based on Walsh sequences that simultaneously extract information about time-varying fields and suppress dephasing due to incoherent sources of noise. We experimentally demonstrate the Walsh reconstruction method by measuring the temporal profile of various time-varying magnetic fields, including the magnetic field created by an action potential traveling throught the physical model of a neuron.

Chapter 3 extends the Walsh reconstruction method to the problem of estimating the parameters of stochastic fields. The Walsh spectroscopy method samples the noise spectrum in the sequency domain and synthesizes the autocorrelation function in the time domain using a series of linear transformations without the need for solving a deconvolution problem.

Chapter 4 addresses the problem of converting unknown quantum systems in the environment of a quantum probe into quantum resources useful for quantum metrology and sensing. Magnetic double-resonance techniques are introduced and exploited to locate and identify unknown paramagnetic centers in the environment of a single NV center in diamond. These paramagnetic centers are hybrid electron-nuclear spin systems characterized by a single electron spin interacting with a single nuclear spin. The parameters of the magnetic dipolar interaction terms and hyperfine interaction terms are estimated by varying the strength and orientation of the static magnetic field. After initializing the quantum state of multiple electron spins using cross-polarization sequences and coherent feedback techniques, entangled states of two and three electron spins are created to perform a.c. magnetometry, i.e., estimate the amplitude of sinusoidal magnetic fields.

Chapter 5 summarizes the main scientific and technical contributions of this thesis and discusses approaches to develop new technologies in quantum metrology and sensing and solve fundamental problems in many-body quantum physics.

Chapter 2

Time-resolved magnetic sensing with electronic spins in diamond

Quantum probes measure time-varying fields with high sensitivity and spatial resolution, enabling the study of biological, material, and physical phenomena at the nanometer scale. In particular, NV centers in diamond have recently emerged as promising quantum probes for measuring magnetic [1, 2, 3] fields, electric [4] fields, and temperature [5, 6, 7]. These sensors are ideal for nanoscale imaging of living biological systems [8, 9, 10] due to their low cytotoxicity, surface functionalizations [11], optical trapping capability [12, 13] and long coherence time under ambient conditions [14].

Although coherent control techniques have measured the amplitude of constant or oscillating fields, these techniques are not suitable for measuring time-varying fields with unknown dynamics. In this chapter, we introduce a coherent acquisition method (Fig. 2-1) to accurately reconstruct the temporal profile of time-varying fields using Walsh sequences [15, 16, 17]. These decoupling sequences act as digital filters that efficiently extract spectral coefficients while suppressing decoherence, thus providing an improved sensitivity over existing strategies. We experimentally reconstruct the temporal profile of the time-varying magnetic field radiated by a physical model of a neuron using a single electron spin in diamond.

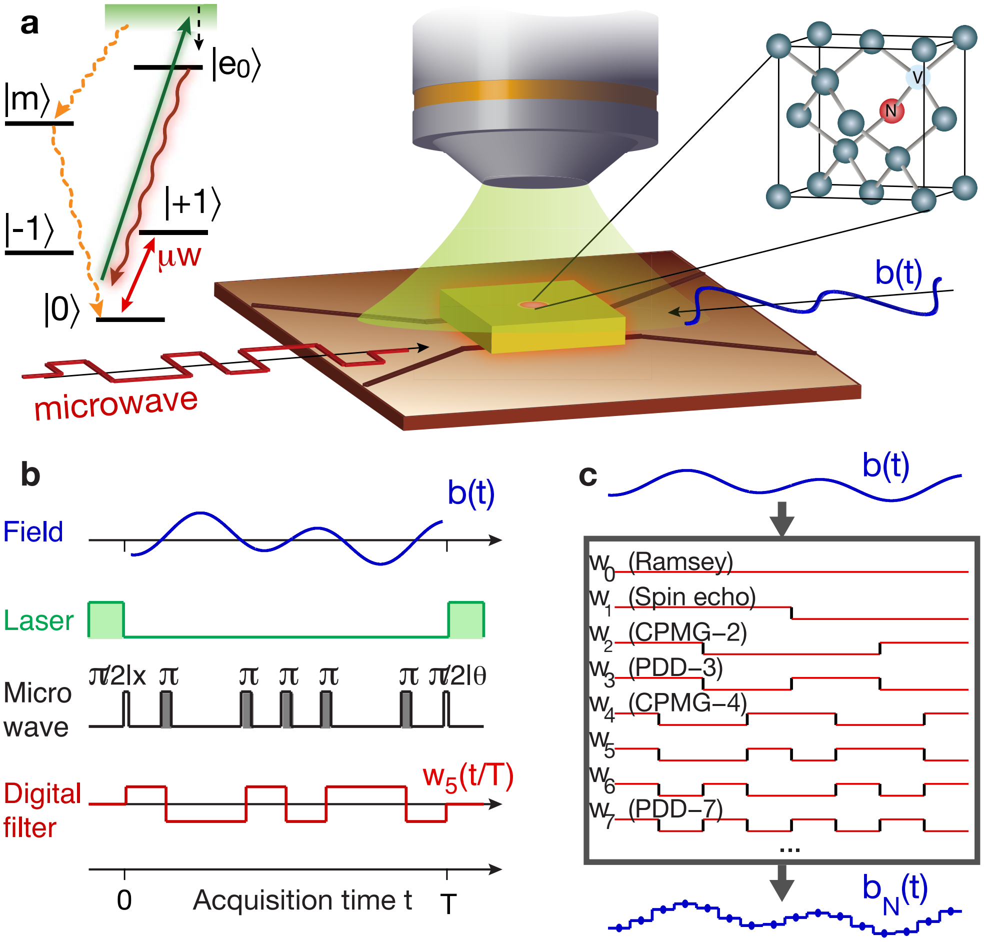

Figure 2-1: **Understand the Walsh reconstruction protocol.** **a,** A single nitrogen-vacancy (NV) center in diamond, optically initialized and read out by confocal microscopy, is manipulated with coherent control sequences to measure the arbitrary profile of time-varying magnetic fields radiated by a coplanar waveguide under ambient conditions. **b,** Coherent control sequences, acting as digital filters on the evolution of the qubit sensor, extract information about time-varying fields. **c,** An N-point functional approximation of the field is obtained by sampling the field with a set of N digital filters taken from the Walsh basis, which contain some known set of decoupling sequences such as the even-parity Carr-Purcell-Meiboom-Gill (CPMG) sequences [18] (w_{2^n}) and the odd-parity Periodic Dynamical Decoupling (PDD) sequences [19] (w_{2^n-1}).

2.1 Quantum parameter estimation with quantum probes

Measurements of weak electric and magnetic fields at the nanometer scale are indispensable in many areas, ranging from materials science to fundamental physics and biomedical science. In many applications, much of the information about the underlying phenomena is contained in the dynamics of time-varying fields. While novel quantum probes promise to achieve the required combination of high sensitivity and spatial resolution, their application to efficiently mapping the temporal profile of time-varying fields is still a challenge.

Quantum estimation techniques [20] measure time-varying fields by monitoring the shift in the resonance energy of a quantum probe, e.g., via Ramsey interferometry. The quantum probe, first prepared in an equal superposition of its eigenstates, accumulates a phase $\phi(T) = \gamma \int_0^T b(t)dt$, where γ is the strength of the interaction with the time-varying field $b(t)$ during the acquisition period T.

The dynamics of time-varying fields could be mapped by measuring the quantum phase over successive, increasing acquisition periods [14] or sequential small acquisition steps [21]; however, these protocols are inefficient at sampling and reconstructing time-varying fields, as the former involves a deconvolution problem, while both are limited by short coherence times (T_2^*) that bound the measurement sensitivity. Decoupling sequences [18, 22, 19] could be used to increase the coherence time [23, 24, 25], but their application would result in a non-trivial encoding of the dynamics of the field onto the phase of the qubit sensor [26, 27, 28, 29, 30].

Instead, here we propose to reconstruct the temporal profile of time-varying fields with a set of digital filters, implemented with coherent control sequences over the whole acquisition period T, that simultaneously extract information about the dynamics of time-varying fields and protect the evolution of the qubit sensor against dephasing noise. In particular, we use control sequences (Fig. 2-2) associated with the Walsh functions [31], which form a complete orthonormal basis of digital filters and are easily implementable experimentally.

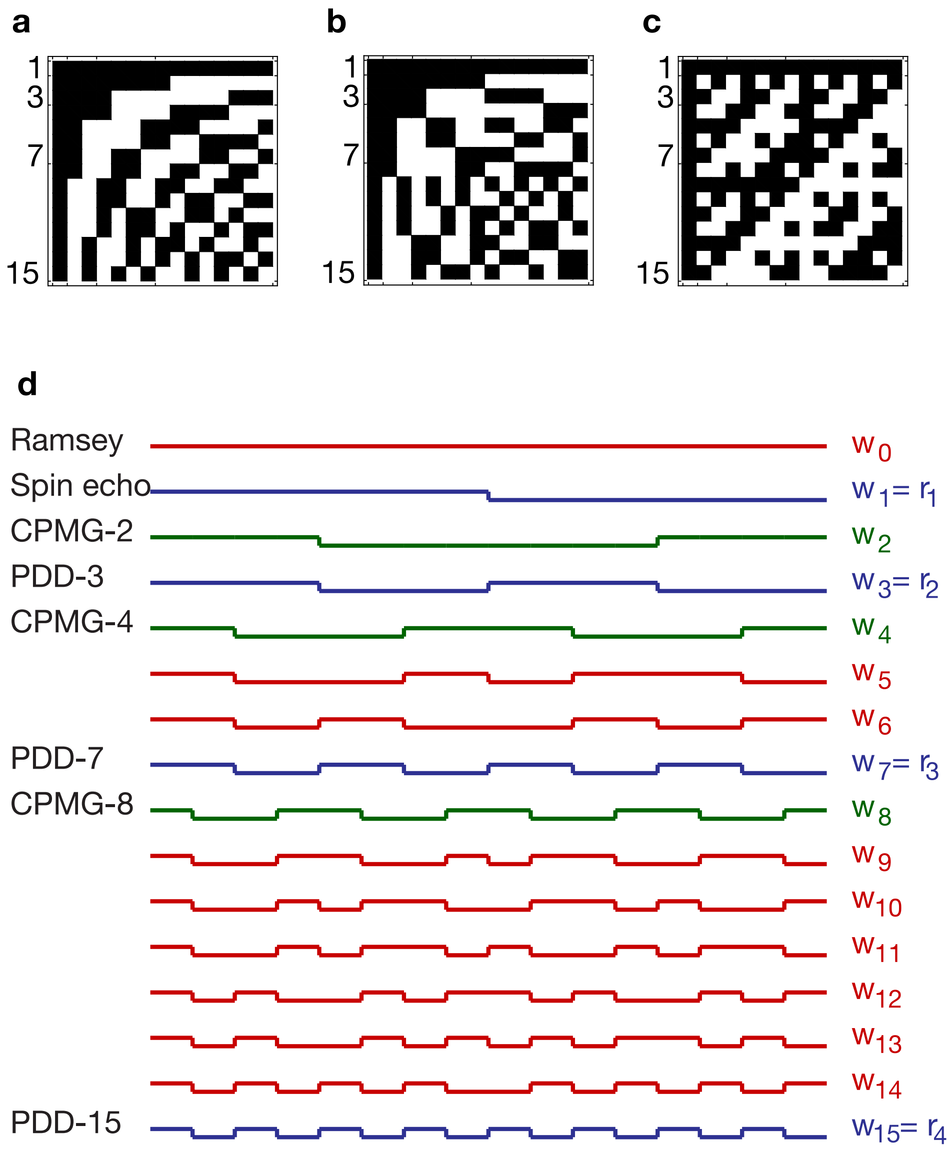

Figure 2-2: **Understand the Walsh functions.** Matrix representation of the Walsh functions up to fourth order ($N = 2^4$) in **a,** sequency ordering, **b,** Paley ordering, and **c,** Hadamard ordering. Each line corresponds to a Walsh sequence with the columns giving the value of the digital filter in the time domain. Black and white pixels represent the values ±1. Each ordering can be obtained from the others by linear transformations. **d** Walsh functions $\{w_m\}_{m=0}^{N-1}$ up to $N = 2^4$ in sequency ordering. The sequency m indicates the number of zero crossings of the m-th Walsh function. The Rademacher functions $r_k = w_{2^k-1}$ correspond to the Walsh functions plotted in blue. Some Walsh functions are associated with known decoupling sequences such as the even-parity CPMG sequences [18] (w_{2^k} green lines) and the odd-parity PDD sequences [19] (w_{2^k-1}, blue lines).

The Walsh reconstruction method uses a complete set of digital filters, implemented with coherent control sequences over the acquisition period T, to simultaneously extract information about the dynamics of time-varying fields and protect the evolution of the quantum probe against dephasing noise. The Walsh reconstruction method can be applied to estimate various time-varying parameters via coherent control of any quantum probe. In particular, we show that the phase acquired by a qubit sensor modulated with Walsh decoupling sequences is proportional to the Walsh transform of the field. This simplifies the problem of spectral sampling and reconstruction of time-varying fields by identifying the sequency domain as the natural description for dynamically modulated quantum systems.

At the same time, the Walsh reconstruction method provides a solution to the problem of monitoring time-dependent parameters with a quantum probe, which in general cannot be achieved via continuous tracking due to the destructive nature of quantum measurements. In addition, because the Walsh reconstruction method achieves dynamical decoupling of the quantum probe, it further yields a significant improvement in coherence time and sensitivity over sequential acquisition techniques. These characteristics and the fact that the Walsh reconstruction method can be combined with data compression [16] and compressive sensing [17, 32] provide clear advantages over prior reconstruction techniques [14, 21, 33, 34].

2.1.1 Understand the Walsh reconstruction method

The Walsh reconstruction method relies on the Walsh functions (Fig. 2-2), which are a family of piecewise-constant functions taking binary values, constructed from products of square waves, and forming a complete orthonormal basis of digital filters, analogous to the Fourier basis of sine and cosine functions. The Walsh functions are usually described in a variety of labeling conventions, including the sequency ordering that counts the number of sign inversions or "switchings" of each Walsh function. The Walsh sequences are easily implemented experimentally by applying π-pulses at the switching times of the Walsh functions; these sequences are therefore decoupling sequences [35, 36], which include the well-known Carr-Purcell-Meiboom-

Gill (CPMG) [18] and Periodic Dynamical Decoupling (PDD) sequences [19].

Walsh functions

The set of Walsh functions [31, 37, 38] $\{w_m(t)\}_{m=0}^{\infty}$ is a complete, bounded, and orthonormal basis of digital functions defined on the unit interval $t \in [0, 1[$. The Walsh basis can be thought of as the digital equivalent of the sine and cosine basis in Fourier analysis. There are different orderings of the Walsh functions in the basis that are interchangeably used depending on the various conventions adopted in different fields. The Walsh functions in the dyadic ordering or Paley ordering are defined as the product of Rademacher functions (r_k): $w_0 = 1$ and $w_m = \prod_{k=1}^{n} r_k^{m_k}$ for $1 \leq m \leq 2^n - 1$, where m_k is the k-th bit of m. The dyadic ordering is particularly useful in the context of data compression [16].The Rademacher functions are periodic square-wave functions that oscillate between ±1 and exhibit 2^k intervals and $2^k - 1$ jump discontinuities on the unit interval. Formally, the Rademacher function of order $k \geq 1$ is defined as $r_k(t) \equiv r(2^{k-1}t)$, with

$$r_k(t) = \begin{cases} 1 & : t \in [0, 1/2^k[\\ -1 & : t \in [1/2^k, 1/2^{k-1}[\end{cases}$$

extended periodically to the unit interval.

The Walsh functions in the *sequency ordering* are obtained from the gray code ordering of m. Sequency is a straightforward generalization of frequency which indicates the number of zero crossings of a given digital function during a fixed time interval. As such, the sequency m indicates the number of control π-pulses to be applied at the zero crossings of the m-th Walsh function. The sequency ordering is thus the most intuitive ordering in the context of digital filtering with control sequences.

The Walsh functions in the *Hadamard ordering* are represented by the Walsh-Hadamard square matrix of size $2^n \times 2^n$, whose elements are given by $H^{(n)}(i+1, j+1) = \prod_{l=0}^{2^n-1} (-1)^{i_l \cdot j_l}$. The Walsh-Hadamard matrix is used as a quantum gate in quantum information processing to prepare an equal superposition of 2^n orthogonal states from a set of n initialized qubits.

Walsh sequences

Because a microwave π-pulse effectively reverses the evolution of a quantum probe, control sequences formed by a series of π-pulses act as digital filters that sequentially switch the sign of the evolution between ± 1. If $w_m(t/T)$ is the digital filter created by applying m control π-pulses at the zero-crossings of the m-th Walsh function, the normalized phase acquired by the quantum probe prepared in a coherent superposition of states is

$$\frac{1}{\gamma T}\phi_m(T) = \frac{1}{T}\int_0^T b(t)w_m(t/T)dt \equiv \hat{b}(m). \tag{2.1}$$

Here $\hat{b}(m)$ is the m-th Walsh coefficient defined as the Walsh transform of $b(t)$ evaluated at the sequence number (sequency) m. This identifies the sequency domain as the natural description for digitally modulated quantum systems. Indeed, Eq. (2.1) implies a duality between the Walsh transform and the dynamical phase acquired by a quantum probe under digital modulation, which allows for efficient sampling of time-varying fields in the sequency domain and direct reconstruction in the time domain via linear inversion.

In particular, successive measurements with the first N Walsh sequences $\{w_m(t/T)\}_{m=0}^{N-1}$ give a set of N Walsh coefficients $\{\hat{b}(m)\}_{m=0}^{N-1}$ that can be used to reconstruct an N-point functional approximation to the field

$$b_N(t) = \sum_{m=0}^{N-1} \hat{b}(m)w_m(t/T). \tag{2.2}$$

Eq. (2.2) is the inverse Walsh transform of order N, which gives the best least-squares approximation to $b(t)$. With few assumptions or prior knowledge about the dynamics of the field, the reconstruction can be shown to be accurate with quantifiable truncation errors and convergence criteria [37, 38].

Although the signal is encoded on the phase of a quantum probe in a different way (via decoupling sequences), the Walsh reconstruction method shares similarities with classical Hadamard encoding techniques in data compression, digital signal processing, and nuclear magnetic resonance imaging [39, 40, 41]. All of these techniques could easily be combined to achieve both spatial and temporal imaging of magnetic fields at the nanometer scale, given the availability of gradient fields and frequency-selective pulses.

Walsh transform

The *Walsh-Fourier series* of an integrable function $b(t) \in L^1([0,T[)$ is given by

$$b(t) := \sum_{m=0}^{\infty} \hat{b}(m) w_m(t/T), \tag{2.3}$$

where the *Walsh-Fourier coefficients* are given by the Walsh transform of $b(t)$ evaluated at sequency m, i.e.,

$$\hat{b}(m) = \frac{1}{T} \int_0^T b(t) w_m(t/T) dt \in \mathbb{R}, \ \forall m \geq 0. \tag{2.4}$$

The truncation of the Walsh-Fourier series up to N coefficients gives the N-th partial sums of the Walsh-Fourier series,

$$b_N(t) := \sum_{m=0}^{N-1} \hat{b}(m) w_m(t/T), \tag{2.5}$$

which can be shown to satisfy $\lim_{N\to\infty} b_N(t) = b(t)$, almost everywhere for $b(t) \in L^1([0,T[)$ and uniformly for $b(t) \in C([0,T[)$ [38]. Equation (2.5) gives the N-point functional approximation to the field $b(t)$.

2.1.2 Quantify the performance of the Walsh reconstruction method

The performance of the Walsh reconstruction method is determined by the reconstruction error e_N and the measurement sensitivity η_N. The least-squares reconstruction error $e_N = \|b_N(t) - b(t)\|_2$ due to truncation of the Walsh spectrum up to $N = 2^n$ coefficients is bounded by $e_N \leq \max_{t\in[0,T]} |\partial_t b(t)|/2^{n+1}$ [38] and vanishes to zero as N tends to infinity (as needed for perfect reconstruction). This implies that although the resources grow exponentially with n, the error converges exponentially quickly to zero, and only a finite number of coefficients is needed to accurately reconstruct the field.

Sensitivity

The measurement sensitivity of the m-th Walsh sequence in M measurements,

$$\eta_m = \frac{v_m^{-1}}{\gamma_e C\sqrt{T}|\hat{f}(m)|} = \frac{\hat{\eta}_m}{|\hat{f}(m)|}, \tag{2.6}$$

gives the minimum field amplitude, $\delta b_m = \eta_m/\sqrt{MT} = \Delta S_m/(|\partial S_m/\partial b_m|\sqrt{M})$, that can be measured with fixed resources. Here $\gamma_e = 2\pi \cdot 28\ \mathrm{Hz}\cdot \mathrm{nT}^{-1}$ is the gyromagnetic ratio of the NV electronic spin and C accounts for inefficient photon collection and finite contrast due to spin-state mixing during optical measurements [1, 42].

The sensitivity is further degraded by the decay of the signal visibility, $v_m = (e^{-T/T_2(m)})^{p(m)} \leq 1$, where $T_2(m)$ and $p(m)$ characterize the decoherence of the qubit sensor during the m-th Walsh sequence in the presence of a specific noise environment. In general, $T_2(m) > T_2$, as the Walsh sequences suppress dephasing noise and extend coherence times by many orders of magnitude [35, 36]. The sensitivity η_m is thus the ratio between a field-independent factor $\hat{\eta}_m$ and the Walsh coefficient $|\hat{f}(m)|$ for the particular temporal profile of the measured field.

The Walsh reconstruction method provides a gain in sensitivity of $\sqrt{N}$ over sequential measurement techniques that perform N successive amplitude measurements over small time intervals of length $\tau = T/N \leq T_2^*$. Indeed, Walsh sequences exploit the long coherence time under dynamical decoupling to reduce the number of measurements, and thus the associated shot noise. This corresponds to a decrease by a factor of N of the total acquisition time needed to reach the same amplitude resolution or an improvement by a factor of $\sqrt{N}$ of the amplitude resolution at fixed total acquisition time. Thus, unless the signal can only be triggered once, in which case one should use an ensemble of quantum probes to perform measurements in small time steps, the Walsh reconstruction method outperforms sequential measurements, which is an important step toward quantum-optimized waveform reconstruction [43].

Measurements with an ensemble of N_{NV} NV centers improve the sensitivity by $1/\sqrt{N_{\mathrm{NV}}}$, such that the sensitivity per unit volume will scale as $1/\sqrt{n_{\mathrm{NV}}}$, where n_{NV} is the density of NV centers. Previous studies have demonstrated $\eta_1 \approx 4$ nT$\cdot$Hz$^{-1/2}$ for a single NV center in an isotopically engineered diamond [14] and $\eta_1 \approx 0.1$ nT $\cdot$ Hz$^{-1/2}$ for an ensemble of NV centers [44], with expected improvement down to $\eta_1 \approx 0.2$ nT $\cdot$ μm$^{3/2}$ $\cdot$ Hz$^{-1/2}$.

Sensitivity improvement over existing sensing techniques

We consider the problem of reconstructing an N-point approximation to the time-varying field $b(t)$ over the acquisition period of length T. Here we show that the Walsh reconstruction method offers an improvement in sensitivity scaling as $\sqrt{N}$ over existing sequential methods. This corresponds to a reduction by $\sqrt{N}$ of the minimum detectable field at fixed total acquisition time or a reduction by N of the total acquisition time at fixed minimum detection field. We compare the Walsh reconstruction method to piece-wise reconstruction of the field via successive acquisition (e.g. with a Ramsey [14, 21] or CW [33] method).

Consider first that we use sequential (e.g., Ramsey) measurements to estimate the amplitude of the field during each of the N sub-intervals of length $\tau = T/N$. The error on each point for shot-noise limited measurements scales as $\delta b_j \sim 1/\tau\sqrt{M_1}$, where M_1 is the number of measurements performed for signal averaging. The total acquisition time is $\mathcal{T}_1 = M_1 N\tau = M_1 T$ and the total reconstruction error on the N-point reconstructed field is

$$(\delta b_N)_1 = \sqrt{\sum_{j=0}^{N-1} \delta b_j^2} = \sqrt{N}\delta b_j \sim \sqrt{N}/\tau\sqrt{M_1}. \tag{2.7}$$

We compare this result to Walsh reconstruction performed via N Walsh measurements, each over the acquisition period T. The error on each Walsh coefficient for shot-noise limited measurements scales as $\delta\hat{b}_m \sim 1/T\sqrt{M_2}$, where M_2 is the number of measurements performed for signal averaging. The total acquisition time is

$\mathcal{T}_2 = M_2NT$ and the total reconstruction error on the N-point reconstructed field (the main text) is

$$(\delta b_N)_2 = \sqrt{\sum_{m=0}^{N-1} \delta\hat{b}_m^2} = \sqrt{N}\delta\hat{b}_m \sim \sqrt{N}/T\sqrt{M_2}. \tag{2.8}$$

For a fixed total acquisition time, $\mathcal{T}_1 = M_1T = M_2NT = \mathcal{T}_2$, we have $M_1 = NM_2$, which means that N times more Ramsey measurements can be performed than Walsh measurements. We however have $(\delta b_N)_1 = \sqrt{N}(\delta b_N)_2$, which means that the Walsh measurements is more sensitive by a factor of $\sqrt{N}$.

For a fixed minimum detectable field, $(\delta b_N)_1 \sim \sqrt{N}/\tau\sqrt{M_1} = \sqrt{N}/T\sqrt{M_2} \sim (\delta b_N)_2$, we have $M_1 = N^2M_2$, which means that N^2 times more Ramsey measurements are needed to measure the exact same minimum field provided by N Walsh measurements. We have then $\mathcal{T}_1 = N\mathcal{T}_2$, such that the total acquisition time for Ramsey measurements is N times longer than for Walsh measurements.

In summary, the Walsh reconstruction method offers a $\sqrt{N}$ improvement in sensitivity over Ramsey measurements, i.e. $(\eta_N)_2 = (\eta_N)_1/\sqrt{N}$. Further improvement in sensitivity can be achieved with data compression [16] and compressive sensing [17] techniques. Given $N_2 < N_1$ and $T = N_1\tau$, we find

$$\frac{(\eta_N)_1}{(\eta_N)_2} = \frac{N_1}{N_2}\sqrt{\frac{T}{\tau}} = \frac{N_1}{N_2}\sqrt{N_1} \tag{2.9}$$

For $N_2 = N_1 = N$, we retrieve $(\eta_N)_2 = (\eta_N)_1/\sqrt{N}$. Given a compression rate $\kappa < 1$, such that $N_2 = \kappa N_1$, we find $(\eta_N)_2 = \kappa(\eta_N)_1/\sqrt{N_1} < (\eta_N)_1/\sqrt{N_1}$. For compressive sensing with resources scaling as $N_2 \sim \log_2(N_1)$, we find

$$(\eta_N)_2 \sim \frac{\log_2(N_1)}{N_1}\frac{(\eta_N)_1}{\sqrt{N_1}} < \frac{(\eta_N)_1}{\sqrt{N_1}}. \tag{2.10}$$

In the discussion above, we did not consider other error sources besides shot noise. Indeed, while the sequential acquisition times are limited by the dephasing noise, the coherence time under the Walsh sequence is in general much longer (typically by 2-3 orders of magnitude for NV centers), thus additional decoherence losses are comparable in the two protocols. We note that even if the total acquisition time T over which one wants to acquire the signal were longer than the coherence time under Walsh decoupling, T_2, it would still be advantageous to use sequential Walsh reconstruction over smaller time intervals, $\sim T_2$. Other considerations, such as power broadening in CW experiments and dead-times associated with measurement and initialization of the quantum probe, make the Walsh reconstruction method even more advantageous.

Amplitude estimation

The sensitivity formula of Eq. (2.6) can be used to identify the Walsh sequences that extract the most information about the amplitude of time-varying fields in the presence of noise. In analogy to a.c. magnetometry [1], which measures the amplitude of sinusoidal fields, we refer to the problem of performing parameter estimation of the amplitude of an arbitrary waveform as *arbitrary waveform (a.w.) magnetometry*. Indeed, if the dynamics of the field is known, the Walsh spectrum can be precomputed to identify the Walsh sequence that offers the best sensitivity. Because different Walsh sequences have different noise suppression performances [35, 16], the choice of the most sensitive Walsh sequence involves a trade-off between large Walsh coefficients and long coherence times.

Given some time-varying fields with known dynamics, the Walsh reconstruction method provides a systematic way to choose for the Walsh sequence that gives the best estimate of the amplitude of the field with the optimal sensitivity. For example, the spin-echo sequence ($w_1(t/T)$) gives the best sensitivity for measuring the amplitude of a sinusoidal field $b(t) = b \sin(2\pi\nu t)$ with known frequency $\nu = 1/T$. If the dynamics of the field is only partially known, an estimate of the field amplitude can be obtained by distributing the resources over a fixed subset of Walsh sequences; for example, by choosing the spin-echo sequence ($w_1(t/T)$) and CPMG-2 sequence ($w_2(t/T)$) to measure the amplitude of an oscillating field $b(t) = b \sin(2\pi\nu t + \alpha)$ with known frequency $\nu = 1/T$ but unknown phase α.

Amplitude resolution

We can compute the minimum field amplitude that can be estimated from M measurements with the m-th Walsh sequence from the quantum Cramer-Rao bound:

$$\delta b_m = \frac{1}{\sqrt{M}} \frac{\Delta S_m}{|\partial S_m/\partial b|} = \frac{v_m^{-1}}{\gamma_e C \sqrt{M} T |\hat{f}(m)|},$$

where $\gamma_e = 2\pi \cdot 28\ \mathrm{Hz} \cdot \mathrm{nT}^{-1}$ is the gyromagnetic ratio of the NV electronic spin, C accounts for inefficient photon collection and finite contrast due to spin-state mixing during optical measurements [1, 42] and $v_m = (e^{-T/T_2(m)})^{p(m)} \leq 1$ is the visibility, which depends on the parameters $T_2(m)$ and $p(m)$, which characterize the decoherence of the qubit sensors during the m-th Walsh sequence.

The minimum field amplitude δb_m is related to the minimum resolvable Walsh coefficient $\delta\hat{b}_m = \Delta S_m/|\partial S_m/\partial \hat{b}_m|\sqrt{M} = \delta b_m |\hat{f}(m)|$. Given a total measurement time $T_{total} = MT$, the corresponding sensitivities are $\eta_m = \delta b_m \sqrt{\mathcal{T}}$ and $\hat{\eta}_m = \delta\hat{b}_m \sqrt{\mathcal{T}} = \eta_m |\hat{f}(m)|$ (cf. Eq. (3) of the main text). The statistical error on the field function $b_N(t)$ reconstructed from the measured set of N Walsh coefficients $\{\hat{b}(m)\}_{m=0}^{N-1}$ is obtained from the errors on each coefficient by $\delta b_N^2(t) = \sum_m \delta\hat{b}_m^2 |w_m(t)|^2 = \sum_m \delta\hat{b}_m^2 \mathbb{1}_{[0,T[}(t)$, which is constant on the time interval $t \in [0, T[$. This quantity gives the measurement sensitivity of the Walsh reconstruction method $\eta_N = \delta b_N \sqrt{N\mathcal{T}} = \sqrt{N \sum_m \hat{\eta}_m^2}$.

The amplitude resolution of the Walsh reconstruction method, $\delta b_N = \sqrt{\sum_m \delta\hat{b}_m^2}$, gives the smallest variation of the reconstructed field that can be measured from the Walsh spectrum of order N. If each Walsh coefficient is obtained from M measurements over the acquisition period T, the measurement sensitivity of the Walsh reconstruction method, $\eta_N \equiv \delta b_N \sqrt{MNT}$, is

$$\eta_N = \sqrt{N \sum_m \hat{\eta}_m^2} = \frac{\sqrt{N \sum_{m=0}^{N-1} v_m^{-2}}}{\gamma_e C \sqrt{T} \sqrt{n_{\mathrm{NV}}}}. \tag{2.11}$$

Reconstruction accuracy

The measurement sensitivity η_N combines with the reconstruction error e_N to determine the accuracy of the Walsh reconstruction method. If some small coefficients cannot be resolved due to low signal visibility, the increase in reconstruction error can be analytically quantified using data compression results [16]. In the same way, the acquisition time can be reduced by sampling only the most significant coefficients and discarding other negligible coefficients. Furthermore, if the field is sparse in some known basis, which is often the case, a logarithmic scaling in resources can be achieved by using compressed sensing methods based on convex optimization algorithms [17, 32], an advantage that is not shared by other sequential acquisition protocols [14, 21, 33].

The Walsh spectrum of order $N = 16$ for a bichromatic field is shown in Fig. 2-3a-b. The Walsh coefficients were first computed in term of their sequency m, which is related to the number of π pulses needed to implement the corresponding m-th Walsh sequence. The amount of information provided by each Walsh sequence is proportional to the magnitude of the Walsh coefficient; the Walsh spectrum can thus be reordered with the coefficients sorted in decreasing order of their magnitude (Fig. 2-3b). As each Walsh coefficient adds new information to the reconstructed field, the accuracy of the reconstruction improves while the reconstruction error decreases.

Figure 2-4a shows the reconstructed field with an increasing number of Walsh coefficients ($m \in [0, m_{max}]$) in sequency ordering. The reconstruction error decreases monotonically as the number of coefficients increases. If the dynamics of the field is known, the Walsh coefficients can be precomputed and sorted so to allocate the available resources to sample the largest coefficients, which provide the most information about the field. Figure 2-4b shows that not only the accuracy of the reconstruction improves monotonically, but also only the first few coefficients are needed to achieve an accurate estimate of the field.

The set of Walsh sequences contains some known set of digital decoupling sequences such as the Carr-Purcell-Meiboom-Gill (CPMG) sequences (w_{2^n}, $n \geq 1$) and

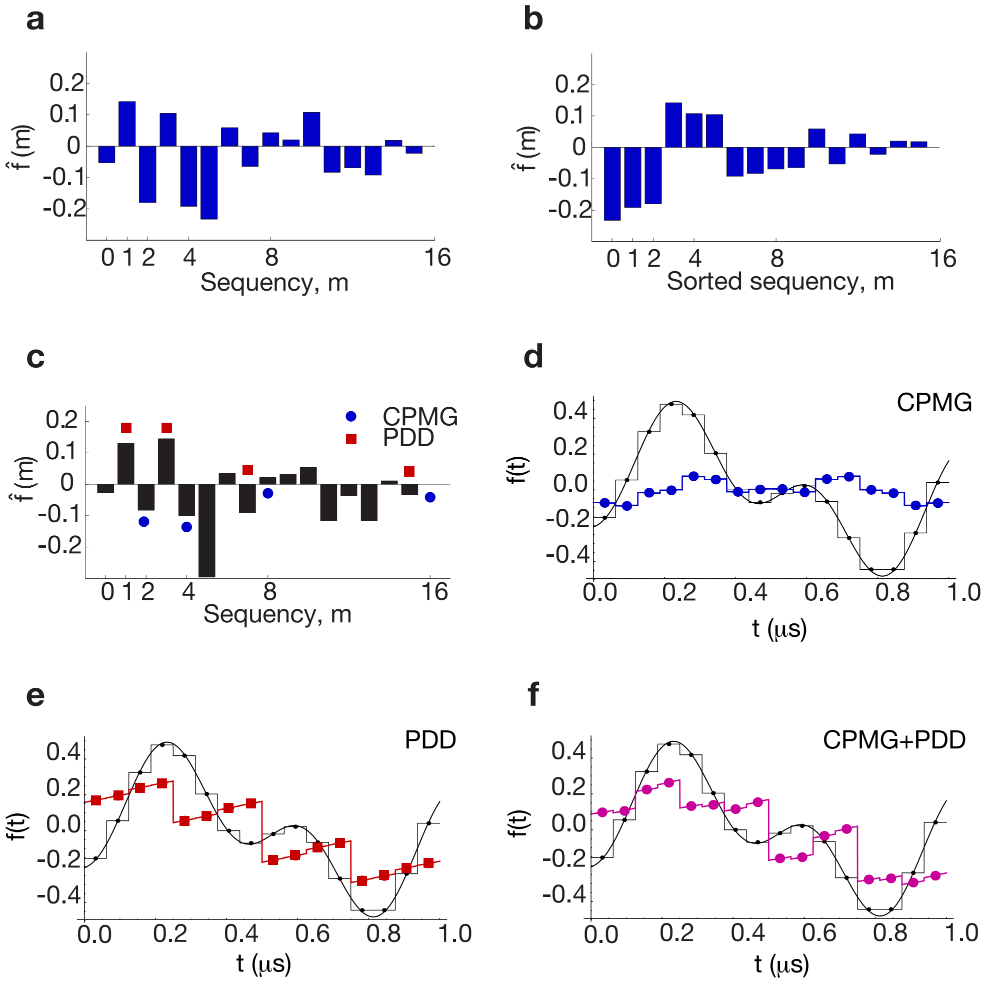

Figure 2-3: **Simulate the reconstruction of bichromatic fields with Walsh sequences.** Simulated Walsh spectrum for a bichromatic field. Walsh coefficients are presented in **a,** sequency ordering and **b,** sorted ordering with decreasing magnitude. If the temporal profile of the field is known, the resources can be allocated to extract the most significant information about the field by sampling the largest Walsh coefficients. **c,** Walsh spectrum up to fifth order ($N = 2^4 = 16$). The blue dots and red squares respectively indicate the subset of coefficients associated with the PDD sequences (w_{2^n-1}) and CPMG sequences (w_{2^n}). The field reconstructed with the first 16 CPMG coefficients (**d,**), 16 PDD coefficients (**e,**) and both PDD and CPMG coefficients (**f,**), remains inaccurate in comparison with the reconstructed field obtained with the first 16 Walsh coefficients (black solid line in **d-f**).

the periodic dynamical decoupling (PDD) sequences (w_{2^n-1}, $n \geq 1$), which have been studied in the context of dynamical error suppression and noise spectrum reconstruction. Although the CPMG and PDD sequences can be shown to contain some significant information about the field, they do not contain all the significant infor-

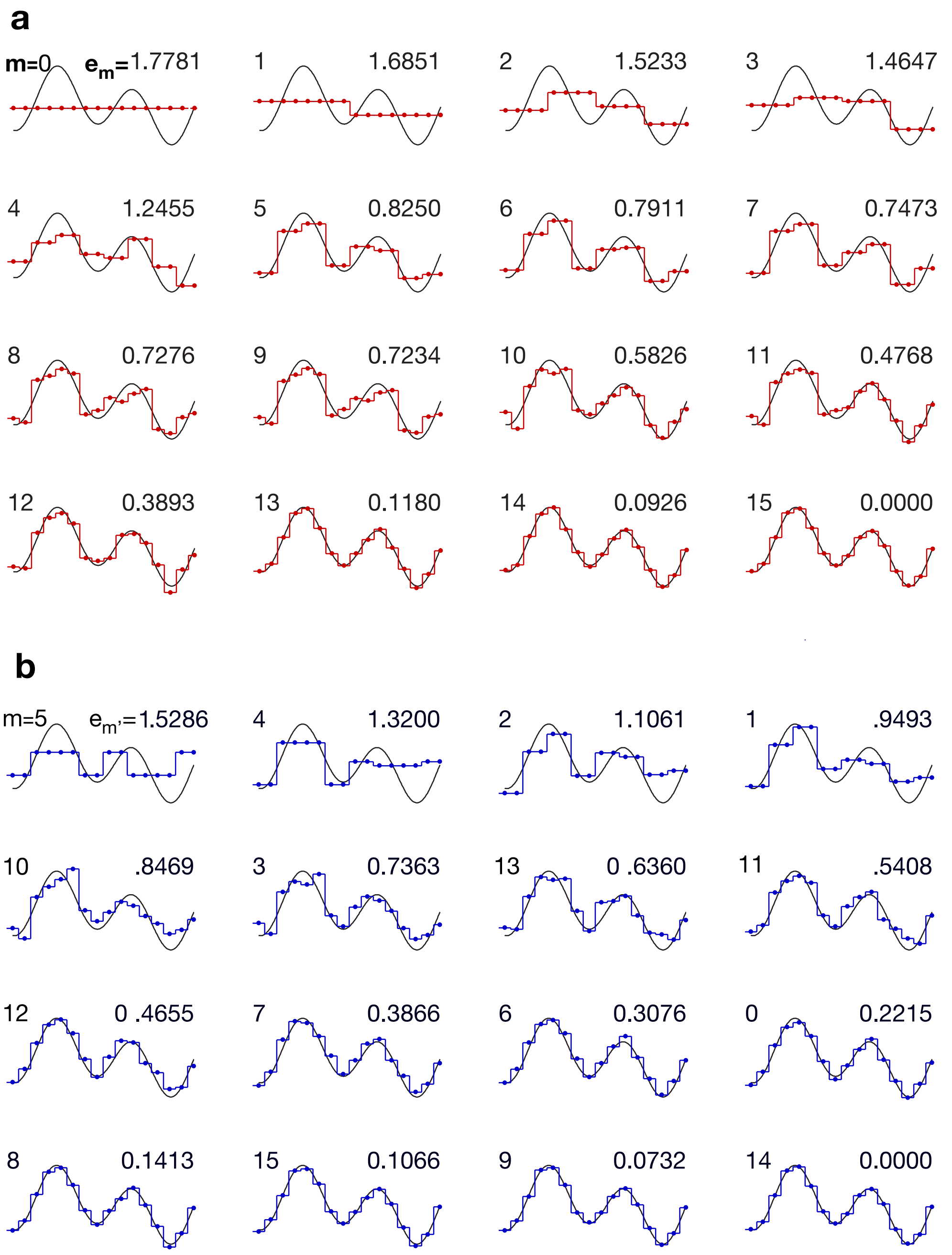

Figure 2-4: **Quantify the accuracy of the Walsh reconstruction method. a**. Reconstruction of a bichromatic field with an increasing number of Walsh coefficients $\{\hat{f}(m)\}_{m=0}^{m_{max}}$ in sequency ordering. **b**. Reconstruction of a bichromatic field with an increasing number of Walsh coefficients $\{\hat{f}(m)\}_{m=0}^{m'_{max}}$ sorted by the coefficient magnitude. A finite number of coefficients is needed to reconstruct an accurate estimate of the field. The upper left and upper right numbers respectively correspond to m (in the sequence order) and the l_2-reconstruction error up to the m' reconstruction, $e_{m'}$.

mation. The CPMG and PDD sequences are indeed symmetric and anti-symmetric functions about their midpoint; they only sample the even and odd symmetries of the field. Figure 2-3c-f shows that the Walsh reconstruction method outperforms the CPMG and PDD sequences, even if the same amount of resources is allocated to sample an equal number of coefficients; because the field does not have a definite parity, the CPMG and PDD sequences fail to accurately reconstruct the field. In addition, these sequences require an exponentially large number of control pulses, which may be detrimental in the presence of pulse errors. Therefore, sampling the field with only these sequences provides incomplete information about the Walsh spectrum and thus leads to inaccurate reconstruction in the time domain.

CPMG and PDD have been used as filters in the frequency domain to achieve frequency-selective detection and reconstruction of noise spectral density.Even for this task, Walsh reconstruction can provide an advantage. Indeed, in the frequency domain, digital filters are trigonometric functions that are not perfectly approximated by delta functions and exhibit spectral leakage, i.e., the non-zero side-lobes of the filter function capture non-negligible signal contributions about other frequencies than the main lobe. Although the CPMG and PDD sequences can be tuned to sample the field at a specific central frequency, they also capture signal at other frequencies, which prevents the accurate reconstruction of time-varying fields. The Walsh reconstruction method removes the need for functional approximations or deconvolution algorithms by choosing the representation that is natural for digital filters: the Walsh basis.

2.2 Demonstrate the Walsh reconstruction method experimentally with a single nitrogen-vacancy center in diamond

We experimentally demonstrate the Walsh reconstruction method by measuring increasingly complex time-varying magnetic fields with the electron spin associated with a single nitrogen-vacancy center in diamond in an isotopically purified diamond sample. A single NV center is optically initialized and read out by confocal microscopy under ambient conditions. A coplanar waveguide delivers both resonant microwave pulses and off-resonant time-varying magnetic fields produced by an arbitrary waveform generator.

2.2.1 Reconstruct the temporal profile of sinusoidal fields

We first reconstructed monochromatic sinusoidal fields, $b(t) = b \sin(2\pi\nu t + \alpha)$, by measuring the Walsh spectrum up to fourth order ($N = 2^4$). Figure 2-5b shows the measured non-zero Walsh coefficients of the Walsh spectrum. As shown in Fig. 2-5c, the 16-point reconstructed fields are in good agreement with the expected fields. We note that, contrary to other methods previously used for a.c. magnetometry, the Walsh reconstruction method is phase selective, as it discriminates between time-varying fields with the same frequency but different phase.

The m-th Walsh coefficient $\hat{f}(m)$ of the normalized field $f(t) = b(t)/b$ was obtained by sweeping the amplitude of the field and measuring the slope of the signal $S_m(b) = \sin(\gamma b \hat{f}(m) T)$ at the origin (Fig. 2-5a). The qubit sensor is first initialized to its ground state $|0\rangle$ and then brought into a superposition of its eigenstates $(|0\rangle + |1\rangle)/\sqrt{2}$ by applying a $\frac{\pi}{2}$-pulse along the σ_x rotation axis. During the free evolution time T, the qubit acquires a phase difference $\phi(T) = \gamma \int_0^T b(t)dt$, where γ is the strength of the interaction with the external time-varying field $b(t)$ directed along the quantization axis of the qubit sensor. Under a control sequence of m π-pulses applied at the zero-crossings of the m-th Walsh function $w_m(t/T)$, the phase difference acquired

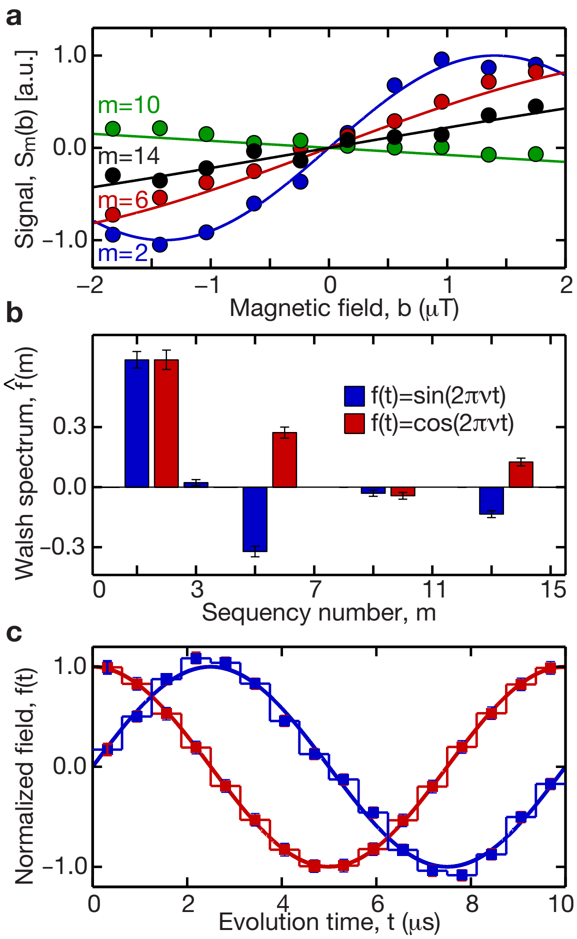

Figure 2-5: **Reconstruct sinusoidal fields with Walsh sequences. a,** Measured signal $S_m(b) = \sin(\gamma_e b \hat{f}(m) T)$ as a function of the amplitude of a cosine magnetic field for different Walsh sequences with m π-pulses. Here $\gamma_e = 2\pi \cdot 28$ Hz $\cdot$ nT^{-1} is the gyromagnetic ratio of the NV electronic spin. The m-th Walsh coefficient $\hat{f}(m)$ is proportional to the slope of $S_m(b)$ at the origin. **b,** Measured Walsh spectrum up to fourth order ($N = 2^4$) of sine and cosine magnetic fields $b(t) = b \sin(2\pi\nu t + \alpha)$ with frequency $\nu = 100$ kHz and phases $\alpha \in \{0, \pi/2\}$ over an acquisition period $T = 1/\nu = 10$ μs. Error bars correspond to 95 % confidence intervals on the Walsh coefficients associated with the fit of the measured signal. **c,** The reconstructed fields (filled squares) are 16-point piecewise-constant approximations to the expected fields (solid lines, not a fit). Error bars correspond to the amplitude uncertainty of the reconstructed field obtained by propagation of the errors on the estimates of the uncorrelated Walsh coefficients.

after an acquisition period T is $\phi_m(T) = \gamma \int_0^T b(t) w_m(t/T) dt = \gamma \hat{b}(m) T$, which is proportional to the m-th Walsh coefficient of $b(t)$. A final $\frac{\pi}{2}$-pulse applied along the $\sigma_\theta = \cos(\theta)\sigma_x + \sin(\theta)\sigma_y$ rotation axis converts the phase difference into a measurable fluorescence signal $S_{x\theta}$.

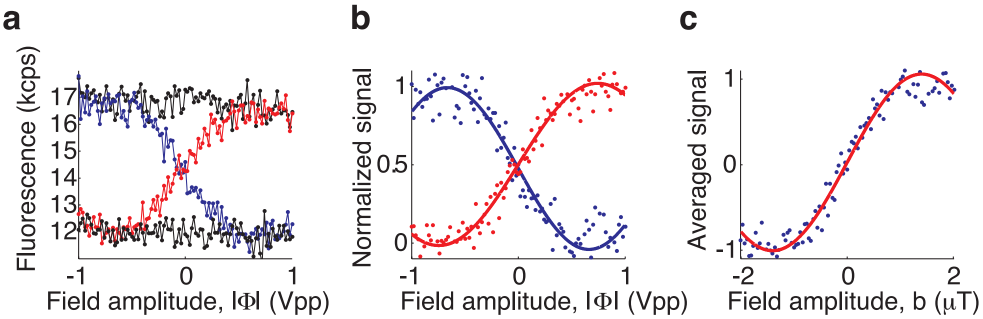

Figure 2-6: **Extract the Walsh coefficient from the fluorescence signal.** Example of experimental data for measuring the m-th Walsh coefficient. **a,** Measured fluorescence signals S_{xy} and $S_{x\bar{y}}$ for a sinusoidal field measured with the $m = 1$ Walsh sequence. **b,** The measured fluorescence signals are normalized with respect to the reference signals. **c,** Average normalized fluorescence signal $S_m(b)$ whose slope at the origin is proportional to the m-th Walsh coefficient $\hat{f}(m)$ of the normalized field $f(t)$.

Although performing a single measurement with $\theta = \pi/2$ is enough to extract the m-th Walsh coefficient, we sweep the field amplitude of $b(t) = b\, f(t)$ to better estimate it (Fig. 2-6). The m-th Walsh coefficient $\hat{f}(m)$ of the normalized field is obtained from the slope at the origin of the normalized fluorescence signal averaged over $M \sim 10^5$ measurements: $S_m(b) = \sin(\gamma_e b \hat{f}_m T) = \frac{S_{x\bar{y}} - S_{xy}}{S_{x\bar{y}} + S_{xy}} \cdot \frac{S_0 + S_1}{S_0 - S_1}$, where S_0 is the fluorescence count rate of the $m_s = 0$ state measured after optical polarization, and S_1 is the fluorescence count rate of the $m_s = 1$ state measured after adiabatic inversion of the qubit with a 600 ns frequency-modulated chirp pulse over a 250 MHz frequency range centered around the resonance frequency.

In practical applications for which the amplitude of the field cannot be swept, the m-th Walsh coefficient can be equivalently measured by sweeping the phase θ of the last read-out $\frac{\pi}{2}$-pulse and fitting the normalized signal to a cosine function: $1 - 2S_m(\theta) = \cos(\gamma_e \hat{b}_m T - \theta) = \frac{S_{x\theta} - S_0}{S_1 - S_0}$. This procedure gives an absolute estimate of $\hat{b}(m)$ rather than an estimate of the normalized coefficient $\hat{f}(m) = \hat{b}(m)/b$.

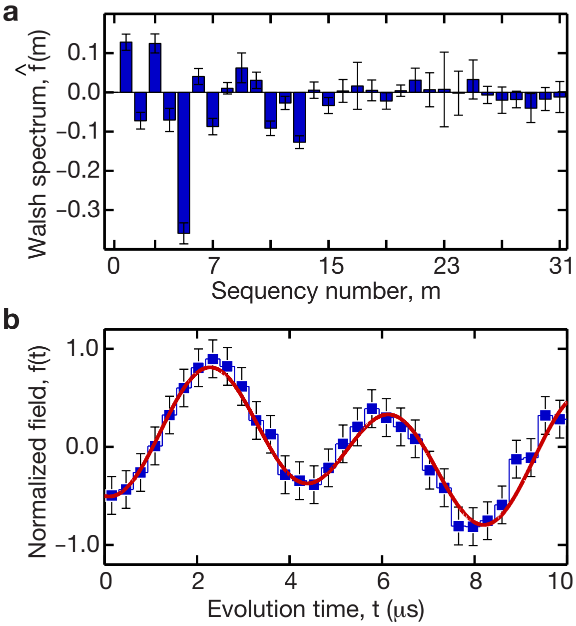

Figure 2-7: **Reconstruct bichromatic fields with Walsh sequences.** **a,** Measured Walsh spectrum up to fifth order ($N = 2^5$) of a bichromatic magnetic field $b(t) = b \cdot [a_1 \sin(2\pi\nu_1 t + \alpha_1) + a_2 \sin(2\pi\nu_2 t + \alpha_2)]$ with $a_1 = 3/10$, $a_2 = 1/5$, $\nu_1 = 100$ kHz, $\nu_2 = 250$ kHz, $\alpha_1 = -0.0741$, and $\alpha_2 = -1.9686$. The zero-th Walsh coefficient $\hat{f}(0)$ corresponds to a static field offset that was neglected. **b,** The reconstructed field (filled squares) is a 32-point approximation to the expected field (solid line, not a fit). Error bars correspond to the amplitude uncertainty of the reconstructed field obtained by propagation of the errors on the estimates of the uncorrelated Walsh coefficients.

2.2.2 Reconstruct the temporal profile of bichromatic fields

We further reconstructed a bichromatic field $b(t) = b\,[a_1 \sin(2\pi\nu_1 t + \alpha_1) + a_2 \sin(2\pi\nu_2 t + \alpha_2)]$. Figure 2-7a shows the measured Walsh spectrum up to fifth order ($N = 2^5$). As shown in Fig. 2-7b, the 32-point reconstructed field agrees with the expected field, which demonstrates the accuracy of the Walsh reconstruction method (Fig. 2-4). In contrast, sampling the field with an incomplete set of digital filters, such as the CPMG and PDD sequences, extracts only partial information about the dynamics of the field (Fig. 2-3). By linearity of the Walsh transform, the Walsh reconstruction method applies to any polychromatic field (and by extension to any time-varying field), whose frequency spectrum lies in the acquisition bandwidth $[1/T, 1/\tau]$ set by the coherence time $T \leq T_2$ and the maximum sampling time $\tau = T/N$, which is in turn limited by the finite duration of the control π-pulses.

2.2.3 Reconstruct the temporal profile of arbitrary time-varying fields

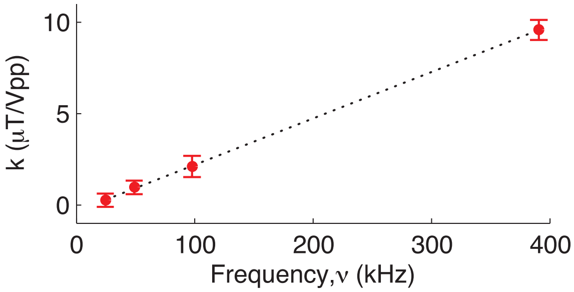

Figure 2-8: **Characterize the transmission properties of the coplanar waveguide.** The conversion factor converts the amplitude of the electric field $\Phi(t)$ into the amplitude of the magnetic field $b(t)$ measured by the NV center. The conversion factor depends linearly on the frequency. Error bars are standard deviation of measurements.

As a proof-of-principle implementation, we measured the magnetic field radiated by a physical model of a neuron undergoing an action potential $\Phi(t)$ approximated by a skew normal impulse [45, 46, 47]. Due to its linear response in the kHz regime (Fig. 2-8), our coplanar waveguide acts as the physical model of a neuron, with the radiated magnetic field given by the derivative of the electric field [48, 49]: $b(t) = d\Phi(t)/dt$ (Fig. 2-9).

Calibrate the transmission spectrum of the coplanar waveguide

Coplanar waveguides were fabricated by e-beam photolithography on microscope glass coverslips, soldered on a PCB board, and mounted to the confocal microscope. Electric waveforms $\Phi(t)$ (Vpp) were generated with an arbitrary waveform generator, amplified, and sent through the coplanar waveguide. The coplanar waveguide radiates a magnetic field $b(t)$ (nT) at the location of the NV center which can be derived from $\Phi(t)$ via a conversion factor $k(\nu)$ ($\mathrm{nT} \cdot \mathrm{Vpp}^{-1}$).

We calibrated the conversion factor by performing a.c. magnetometry experiments with sinusoidal oscillating fields ($\nu = 1/T$) sampled with the corresponding Walsh sequence $w_m(t/T)$. The amplitude of the field was swept and the normalized Walsh coefficient was extracted from the measured signal $S_m(b) = \sin(\gamma_e b \hat{f}(m) T)$. The slope at the origin $\mu_{Vpp} = \gamma_e \hat{f}(m) T$ was compared with the value computed analytically, e.g., by choosing $\hat{f}(1) = 2/\pi$ for the spin-echo sequence (m=1). The conversion factor $k = \mu_{nT}/\mu_{Vpp}$ (nT $\cdot$ Vpp^{-1}) was calculated from the ratio between μ_{nT} calculated analytically and μ_{Vpp} measured experimentally at different frequencies.

As shown in Fig. 2-8, the conversion factor $k(\nu)$ increases linearly in the frequency range of interest. Taking into account the intrinsic 90° phase shift between the electric and magnetic fields, we have $b(\nu) = -ic\nu\Phi(\nu)$ such that $b(t) = -c\frac{d\Phi(t)}{dt}$ with $c =$ 25.4 μT $\cdot$ (Vpp $\cdot$ kHz)$^{-1}$. Therefore, our coplanar waveguide behaves as the physical model of a neuron, with the magnetic field given by the first derivative of the electric field.

Simulate the magnetic field radiated by a single neuron

The creation and conduction of action potentials is the primary communication mean of the nervous system. The flow of ions across neuronal membranes produce an electric field that propagates through the axon of single neurons. The electric signals carried by the action potentials radiate a magnetic field given approximately by the first derivative of the action potential [48, 49]. As shown in Fig. 2-9, we approximated the action potential by a skew normal impulse and extracted the physical parameters by fitting the simulation data obtained for a rat hippocampal mossy fiber boutons [46]. The action potential was rescaled to perform proof-of-principle measurements.

Reconstruct the simulated magnetic field radiated by a single neuron

The Walsh coefficients were measured by fixing the amplitude of the field and sweeping the phase of the last read-out pulse to reconstruct the absolute field $b(t)$ rather than the normalized field $f(t)$. This protocol is in general applicable when the field amplitude is not under experimental control. Figure 2-10a shows the measured Walsh spectrum up to fifth order ($N = 2^5$). As shown in Fig. 2-10b, the 32-point recon-

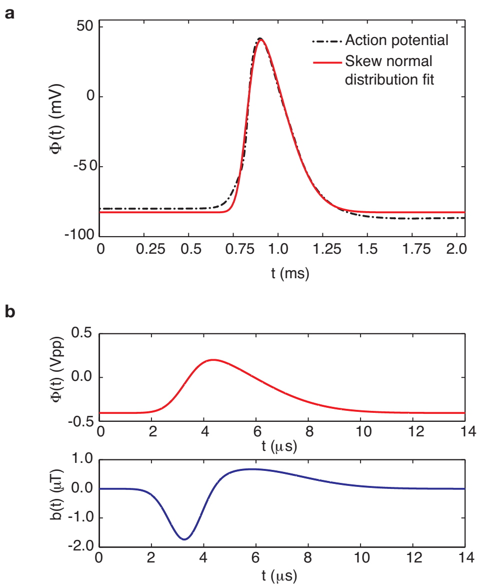

Figure 2-9: **Simulate an action potential. a** ,The simulated action potential of a rat hippocampal mossy fiber boutons [46] is approximated by a skew normal impulse. **b**, The action potential is rescaled to perform the Walsh reconstruction experiment, with the radiated magnetic field corresponding to the first derivative of the action potential.

structed field is in good agreement with the expected field. Although neuronal fields are typically much smaller than in our proof-of-principle experiment with a single NV center, they could be measured with shallow-implanted single NVs [50, 51, 52, 53] or small ensembles of NV centers [10, 44, 54].

The total measurement time for acquiring all the data of the $T = 14$ μs waveform presented in Fig. 2-10, excluding dead times associated with computer processing and interfacing, was less than 4 h. Each of the $N = 32$ Walsh coefficients were obtained from two $M' = 90$ measurements of the fluorescence signal as a function of the phase and conjugate phase of the last readout pulse to correct for common-mode noise (we note that in a well-calibrated, temperature stabilized and isolated setup this step is unnecessary). Each experimental point was averaged over $M = 10^5$ repetitive measurements due to low light-collection efficiency. The length of each sequence was about 42 μs, including the two waveform measurements (28 μs), optical polarization and readout periods (5 μs), adiabatic inversion (4 μs) used for calibration purposes but not necessary, and waiting time (5 μs).

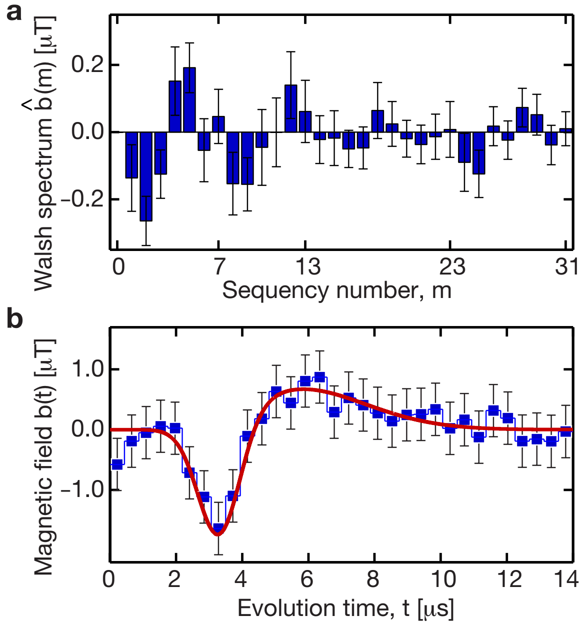

Figure 2-10: **Reconstruct arbitrary time-varying fields with Walsh sequences. a,** Measured Walsh spectrum up to fifth order ($N = 2^5$) of the magnetic field radiated by a skew normal impulse flowing through the physical model of a neuron. The Walsh coefficients were obtained by fixing the amplitude of the field and sweeping the phase of the last read-out $\pi/2$-pulse. The acquisition time for measuring all the Walsh coefficients was less than 4 hours. Error bars correspond to 95 % confidence intervals on the Walsh coefficients associated with the fit of the measured signal. **b,** The reconstructed field (filled squares) is a 32-point approximation to the expected field (solid line, not a fit). Error bars correspond to the amplitude uncertainty of the reconstructed field obtained by propagation of the errors on the estimates of the uncorrelated Walsh coefficients.

2.3 Conclusion and outlook

In conclusion, we used control sequences acting as digital filters on the evolution of a single NV electronic spin to efficiently sample and accurately reconstruct the arbitrary profile of time-varying fields with quantifiable errors and formal convergence criteria.

The Walsh reconstruction method is readily applicable to measure time-varying parameters in a variety of physical systems, including light shift spectroscopy with trapped ions [30]; magnetometry with single spins in semiconductors [2, 55, 56] or quantum dots [57]; and measurements of electric fields [4] or temperature [5, 6, 7] with NV centers in diamond. Other promising applications include magnetic resonance spectroscopy of spins extrinsic to the diamond lattice [52, 53], measurements of the dynamics of magnetic nanostructures [58], or magnetic vortices in nanodisk chains [59].

The Walsh reconstruction method can easily be used together with spatial encoding techniques to achieve both spatial and temporal imaging of magnetic fields. In addition, this method is compatible with data compression techniques [16] and compressed sensing algorithms [17, 32] to achieve a significant reduction in resources, acquisition time, and reconstruction errors. Extension of the Walsh reconstruction method to stochastic fields could simplify the problem of spectral density estimation by removing the need for functional approximations or deconvolution algorithms [60, 27, 29]. This would enable, e.g., in-vivo monitoring of cellular functions associated with cell membrane ion-channel processes [61, 62]. Finally, this work connects with other fields in which the Walsh functions have recently attracted attention, e.g., in quantum simulation to construct efficient circuits for diagonal unitaries [63], in quantum error suppression [35, 36], and in quantum control theory to improve the fidelity of two-qubit entangling gates on trapped atomic ions [64].

2.3.1 Comparison with existing techniques

The problem of measuring the time-varying magnetic fields with NV centers in diamond has also been discussed by Balasubramanian *et al.* [14] and Hall *et al.* [21].

They both considered Ramsey interferometry measurements to detect time-varying magnetic fields, either by sweeping the measurement time or translating the acquisition window.

The first protocol presents a deconvolution problem that requires numerical algorithms to be solved and makes it difficult to analytically quantify the reconstruction error. In addition, the field is not efficiently sampled due to spectral leakage, because the window function is a sinc function, rather than a delta function, in the frequency domain. The Walsh transform method simplifies the problem of spectral sampling and reconstruction by setting the sequency domain, rather than the frequency domain, as the natural description for digitally sampled fields.

The second protocol does not require solving the inversion problem, as it directly gives the average field value during each sampling interval. However, the time required to achieve the same sensitivity as the Walsh method for an N-point reconstruction is N times longer.

More importantly, these methods are not compatible with optimized protocols based on adaptive and compressive sampling. In particular, compressive sensing is fully compatible with the Walsh reconstruction method and for many sparse signals it would lead to a large saving in measurement time. Indeed, sequentially measuring the field over small time intervals δt requires performing $N = T/\delta t$ acquisitions to reconstruct the whole evolution, while one in general only needs $m \propto \log(N)$ measurements using compressive sensing techniques [17].

Hall *et al.* [21] also considered using an optically detected magnetic resonance protocol [33, 34] for measuring time-varying fields. This protocol is meant to perform real-time measurements of the resonance frequency of the NV centers via a lock-in detection system. Although this protocol is presented as continuously monitoring the field, a finite binning time is required ($\sim 24\ \mu$s in the case of Ref. [21]) since the measurement on the NV center is destructive. In addition, continuous driving protocols are inherently less sensitive than pulsed ones, as the continuous laser light and microwave field induce power broadenitng, in addition to heating, which can be detrimental to biological samples.

2.3.2 Applications to sensing neural activity

An active research direction for quantum sensors is measuring biological [61, 62, 10] and neuronal [54, 21] activity at the nanometer scale. Hall *et al.* [21] provided compelling evidence about the feasibility of measuring the magnetic fields radiated by action potentials flowing through single neurons. They calculated magnetic field strengths of the order of 10 nT at distance up to 100 nm from a morphologically reconstructed hippocampal CA1 pyramidal neuron. These fields are within experimental reach using small ensembles of shallow-implanted NV centers, e.g., located less than 10 nm below the diamond surface [50, 51], given improvements in collection efficiency [44, 65] and coherence times [66].

The Walsh reconstruction method may also prove useful in neuroscience, alongside existing electrical activity recording techniques and other emerging neuroimaging modalities, to monitor the weak magnetic activity of neuronal cells at subcellular spatial resolution, as needed to better understand neurophysiology and map neuronal circuits. To achieve a repeatable signal and reduce stochastic fluctuations during averaging, sequential trains of action potentials could be evoked with conventional electrophysiological techniques, photo-stimulation methods, or current injection through underlying nanowire electrode arrays [67]. Technical issues associated with maintaing the stability of the system over long time scale still remain to be solved.

An alternative to wide-field imaging would be to use functionalized nanodiamonds with coherence time approaching bulk diamonds as both fluorescent biomarkers and quantum probes to perform local measurements of magnetic fields and temperature. Advantages would include selective positioning, high sensitivity, and minimal invasiveness. Neuronal growth and mobility could also be studied by optically tracking the position of nanodiamonds over long time scale.

The spatial resolution will be limited by the diffraction limit in a confocal microscopy setting (unless sub-diffraction techniques are used) and the pixel size in a wide-field imaging setup. Because neurons are living cells that move, relative displacements of the quantum sensors with respect to the living neurons will induce fluctuations in the amplitude of the magnetic field at the position of each NV center. These fluctuations will be averaged over each pixel for measurements with ensembles of NV centers, given that the pixel size is greater than the displacement of the neuron during the acquisition period.

The Walsh reconstruction method depends on a repeatable signal assumed to be deterministic and triggered on-demand. Action potentials can be artificially created by external stimulation techniques that involve creating large potential differences across the membrane and injecting current into the system. An initial stimulus at one end of the axon creates a potential difference across the axonal membrane; when the difference is above some threshold value, the potential suddenly spikes upwards and returns to its resting value as equilibrium is restored in the system. This spike, called the action potential, propagates along the length of the axon to the other end, where it can stimulate other connecting nerve cells. The action potential can create magnetic fields at the nT scale [45] and each event lasts for a wide range of time scales from 1 μs to 10 ms.

While there is large variability in these techniques, their key point is that the timing of events can be controlled to a high degree. Trains of hundreds action potentials can be repeatedly evoked in neuronal cells via conventional electrophysiological techniques, photo-stimulation methods, or current injection through underlying nanowire electrode arrays. The stimulation rate needs to be below the frequency threshold to avoid propagation failure [47] due to geometrical constraints, depolarization of the membrane, or hyperpolarization of the axon. The stimulation frequency threshold depends on the type of neuronal cells and range from moderate ($10-50$ kHz) to high ($200-300$ Hz), sometimes even up to 1 kHz for axons in the auditory pathways [47]. Short trains of N action potentials are evoked at a stimulation rate of 100 kHz in M stimulation-recovery cycles of length 1 s, for a total acquisition time less than few hours, within the lifespan of neurons (several hours). Data compression methods [16] or compressed sensing techniques [17] can be used to significantly reduce the acquisition time.

Chapter 3

Spectral reconstruction of stochastic fields with Walsh sequences

This chapter extends the Walsh reconstruction method to characterize the spectral properties of stochastic fields with quantum probes [68, 69].

3.1 Noise spectroscopy with single quantum probes

We consider the evolution of a quantum probe formed by a single qubit interacting with an external time-varying magnetic field directed along its quantization axis, such that the resonance frequency $\omega(t)$ of the qubit is varying in time. We prepare the qubit in an equal superposition of its eigenstates and estimate the dynamic phase acquired after a sensing period of duration T,

$$\begin{aligned} \phi(T) &= \int_0^T \omega(t)dt && (3.1) \\ &= \omega_0(T) \cdot T, && (3.2) \end{aligned}$$

where the effective precession frequency $\omega_0(T) = \frac{1}{T}\int_0^T \omega(t)dt$ is equal to the time-averaged precession frequency of the qubit during the sensing period $[0, T[$. Gaining information about the temporal dynamics of the resonance frequency $\omega(t)$ by performing a series of projective measurements on the quantum probe after short evolution periods $T = T_2^*$ is inefficient, because of the probabilistic nature of quantum measurements that introduces projection noise in the measurement outcomes and destroy the quantum information encoded into the quantum state of the quantum probe.

We instead modulate the evolution of the quantum probe with a control sequence of m time-inverting π-pulses, specifically chosen among the set of Walsh sequences. The dynamic phase acquired by the qubit sensor modulated with the m-th Walsh sequence $w_m(t/T)$ after a sensing period of duration T is

$$\begin{aligned} \phi_m(T) &= \int_0^T \omega(t) w_m(t/T) dt && (3.3) \\ &= \hat{\omega}_m(T) \cdot T, && (3.4) \end{aligned}$$

where the effective precession frequency $\omega_m(T) = \hat{\omega}_m(T)$ is equal to the Walsh transform of the time-varying resonance frequency computed over the interval $[0, T[$,

$$\hat{\omega}_m(T) \equiv \frac{1}{T} \int_0^T \omega(t) w_m(t/T) dt. \tag{3.5}$$

The signal obtained after averaging the measurement results of a series of M sequential Ramsey interferometry experiments is given by

$$\begin{aligned} \mathcal{S}_m(T) &= \langle \exp\left(i \hat{\omega}_m(T) \cdot T\right) \rangle_M && (3.6) \\ &= \exp\left(\sum_{n=1}^{\infty} \frac{(-iT)^n}{n!} \langle \hat{\omega}_m^n(T) \rangle_c \right) && (3.7) \\ &\approx \exp\left(-i \langle \hat{\omega}_m(T) \rangle T\right) \; \exp\left(-\langle \hat{\omega}_m^2(T) \rangle_c T^2/2\right), && (3.8) \end{aligned}$$

where $\langle \cdot \rangle_M$ denotes the ensemble average over M sequential measurements and $\langle \cdot \rangle_c$ denotes the cumulants of the probability distribution associated with the stochastic variable $\hat{\omega}_m(T)$. The last approximation, which is valid under the assumption of Gaussian noise, shows that the signal $\mathcal{S} = \mathcal{M} \cdot \mathcal{N}$ is equal to the product of a coherent term $\mathcal{M} = \exp\left(-i \langle \omega_m(T) \rangle T\right)$ that causes the signal to oscillate coherently and an incoherent term $\mathcal{N} = \exp\left(-\langle \omega_m^2(T) \rangle_c T^2/2\right)$ that causes the signal to decay. The decay rate of the signal is given by the second cumulant of $\hat{\omega}_m(T)$, which as we will see, is proportional to the autocorrelation function $R(t_1, t_2)$ associated with the fluctuations in the precession frequency $\omega(t)$.

The problem of estimating deterministic parameters addressed in Chapter 2 consists in finding the modulation sequence $w_m(t)$ that maximizes the information extracted from the interferometric signal and thus involves a tradeoff between increasing the coherent term and decreasing the incoherent term, which causes a loss in signal visibility due to dissipative sources of noise. The problem of estimating stochastic parameters addressed in this chapter consists in gaining information about the probability distribution of $\omega(t)$ from a series of measurements of the decay rate of the signal $\Gamma_2^m(T) = \sqrt{\langle \hat{\omega}_m^2(T) \rangle}$ for different choices of the evolution time T and modulation sequences $\{w_m(t)\}$. This chapter focuses on the problem of estimating stochastic parameters, more precisely on the problem of estimating the spectral density of stochastic fields with quantum probes modulated with Walsh sequences.

We model the external time-varying field $b(t)$ by a stochastic process, such that the precession frequency of the qubit probe $\omega(t) = \gamma b(t)$ is a stochastic variable, where γ is the interaction strength between the qubit probe and the external time-varying field, e.g., $\gamma = \gamma_e = 2.8025$ MHz/G for electron spins interacting with magnetic fields. The precession frequency of the qubit can be written as $\omega(t) = \langle \omega(t) \rangle + \tilde{\omega}(t)$, where $\tilde{\omega}(t) = \omega(t) - \langle \omega(t) \rangle$ is assumed to be the realization of a zero-mean, real, wide-sense stationary stochastic process described by its *arithmetic* autocorrelation function $R(t_1, t_2) = R(t_1 - t_2) = E[\tilde{\omega}(t_1)\tilde{\omega}(t_2)]$, where $E[X]$ denotes the expectation of the random variable X.

The central limit theorem is invoked to equate the expectation of X to the ensemble average over M realizations of X in the limit of large M, i.e., we write $E[X] = \langle X \rangle = \frac{1}{M}\sum_{j=1}^{M} X_j$. We can prove that the ensemble average is a consistent estimator of the expectation with chi-squared distribution χ_M^2, i.e., it converges in distribution to the expectation of X:

$$\frac{1}{M}\sum_{j=1}^{M} X_j \xrightarrow{d} E[X] \cdot \chi_M^2 / M. \tag{3.9}$$

We assume the external time-varying field to be a zero-mean stationary Gaussian stochastic process, such that the stochastic variable $\tilde{\omega}(t) = \gamma b(t)$ is fully characterized by its second cumulant, $\langle \hat{\omega}_m^2(T) \rangle_c = \langle \hat{\omega}_m^2(T) \rangle$. The signal of Eq. (3.8) becomes

$$\mathcal{S}_m(T) \;=\; \exp\left(-\langle \hat{\omega}_m^2(T) \rangle T^2/2\right). \tag{3.10}$$

The effective decay rate of the signal $\Gamma_2^m(T) = \sqrt{\langle \hat{\omega}_m^2(T) \rangle}$ during the evolution period $[0, T[$ is given by the variance of the effective precession frequency,

$$\begin{aligned}
\langle \hat{\omega}_m^2(T) \rangle &= \frac{1}{T^2} \int_0^T \int_0^T \langle \tilde{\omega}(t_1) \tilde{\omega}(t_2) \rangle w_m(t_1/T) w_m(t_2/T) dt_1 dt_2 && (3.11) \\
&= \frac{1}{T^2} \int_0^T \int_0^T R(t_1 - t_2) w_m(t_1/T) w_m(t_2/T) dt_1 dt_2 && (3.12) \\
&= \frac{1}{T^2} \int_0^T \int_0^T R(t_1 - t_2) w_m((t_1/T) \oplus (t_2/T)) dt_1 dt_2, && (3.13)
\end{aligned}$$

The term $(t_1/T) \oplus (t_2/T)$ corresponds to the binary addition of $(t_1/T) \in [0, 1[$ and $(t_2/T) \in [0, 1[$, which results from the composition property of Walsh functions under multiplication. The binary addition is carried out by expressing t/T in its binary expansion form, $(t/T)_2 = (0.t_1 t_2 ... t_n)$, where the number of bits in the binary expansion, $n = \lceil \log_2(m) \rceil$, is equal to the smallest order at which the m-th Walsh sequence can be represented.

In its most general form, Equation (3.11) shows that the decay rate is proportional to the autocorrelation function of the time-varying field $R(t_1, t_2)$ sampled by the two-dimension filter $w_m(t_1, t_2) = w_m(t_1) w_m(t_2)$ generated by the Walsh modulation sequence. The symmetry properties of the Walsh functions make it possible to represent the two-dimensional Walsh filters illustrated in Fig. 3-1 as a one-dimensional Walsh filter $w_m(t_1, t_2) = w_m(t_1 \oplus t_2)$ (Fig. 3-2).

3.1.1 Discrete representation of the autocorrelation function

We simplify Eq. (3.12) by expressing the autocorrelation function in its discrete representation. Let $\mathbb{N}(n) = \{0, 1, \cdots, 2^n - 1\}$ be the set of the first $N = 2^n$ non-negative

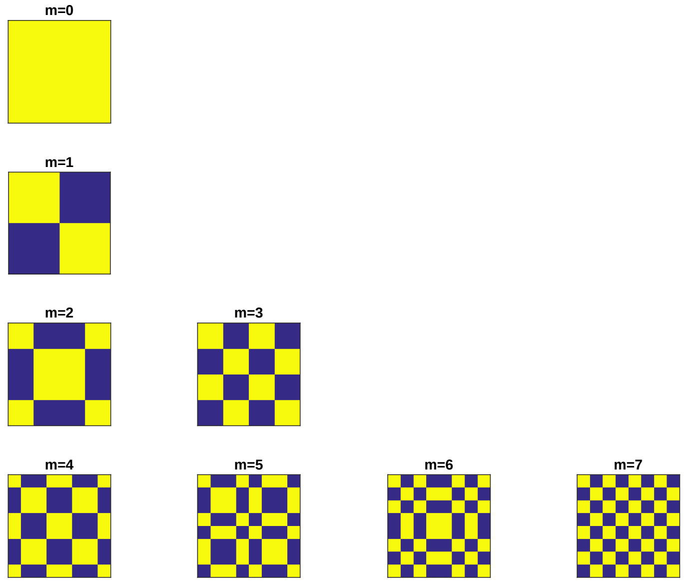

Figure 3-1: **Represent two-dimensional Walsh filters $w_m(t_1, t_2) = w_m(t_1)w_m(t_2)$ in $\mathbb{R}^2([0,1[)$ up to order $n = 3$ in sequency ordering.** The Walsh filters swiches between $w_m = 1$ (yellow) and $w_m = -1$ (blue).

integers. We subdivide the continuous interval $[0, T[$ into N sub-intervals of equal length $\tau = T/N$ with left indices $\tau_j = j \cdot \tau$, $\forall j \in \mathbb{N}(n)$. We define the discrete autocorrelation function, $R'(j) : \mathbb{N}(n) \to \mathbb{R}$, as the average value of the continuous autocorrelation function R on each sub-intervals $[\tau_j, \tau_{j+1}[$, i.e.,

$$R'(j) = \frac{1}{\Delta_j} \int_{\tau_j}^{\tau_{j+1}} R(t)dt, \ \forall \text{æ} \in \mathbb{N}(n), \tag{3.14}$$

where the length of each interval is $\Delta_j = \tau_{j+1} - \tau_j = \tau$.

Equation (3.12) can thus be written as

$$\begin{aligned} \langle \hat{\omega}_m^2(T) \rangle &= \frac{1}{T^2} \int_0^T \int_0^T R(t_1 - t_2) w_m(t_1/T) w_m(t_2/T) dt_1 dt_2 && (3.15) \\ &\approx \frac{1}{N^2} \sum_{j,k=0}^{N-1} R'(j-k) w_m(j/N) w_m(k/N) && (3.16) \\ &= \frac{1}{N^2} \sum_{j,k=0}^{N-1} R'(j-k) w_m((j \oplus k)/N), && (3.17) \end{aligned}$$

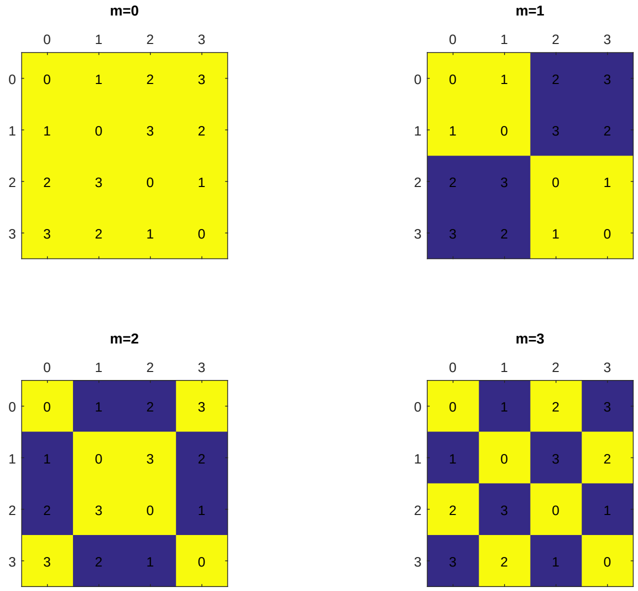

Figure 3-2: **Represent two-dimensional Walsh filters** $w_m(t_1, t_2) = w_m(t_1)w_m(t_2)$ **in** $\mathbb{R}^2([0,1[)$ **up to order** $n = 2$ **in sequency ordering.** The Walsh filters swtiches between $w_m = 1$ (yellow) and $w_m = -1$ (blue). The labels indicate the result of the binary addition $t_1 \oplus t_2$ to illustrate that $w_m(t_1, t_2) = w_m(t_1)w_m(t_2) = w_m(t_1 \oplus t_2)$, i.e., two-dimensional Walsh filters are defined by a single parameter $v = t_1 \oplus t_2$.

where we have used the composition property of Walsh functions under multiplication, $w_m(j)w_m(k) = w_m(j \oplus k)\ \forall j,k \in \mathbb{N}(n)$. After the change of variable $j \to j \oplus k$, we obtain

$$\begin{aligned} \langle \hat{\omega}_m^2(T) \rangle &= \frac{1}{N^2} \sum_{j,k=0}^{N-1} R'(j \oplus k - k) w_m(j/N) && (3.18) \\ &= \frac{1}{N} \sum_{j=0}^{N-1} L_N(j) w_m(j/N) && (3.19) \\ &= P_N(m), && (3.20) \end{aligned}$$

where we have defined the *local logical autocorrelation function* [70, 71] as

$$L_N(j) = \frac{1}{N} \sum_{k=0}^{N-1} R'(j \oplus k - k), \tag{3.21}$$

and the *local Walsh spectral density* as

$$P_N(m) = \frac{1}{N} \sum_{j=0}^{N-1} L_N(j) w_m(j/N). \tag{3.22}$$

The *local Walsh spectral density* corresponds to the Walsh transform of the *local logical autocorrelation function* on the finite time interval $[0, T[$. The *local Walsh spectral density* converges to the *Walsh spectral density* in the limit of large N, i.e.,

$$P(m) = \lim_{N \to \infty} P_N(m). \tag{3.23}$$

Equation (3.20) shows that the variance of the precession frequency is equal to the local Walsh spectral density of $\tilde{\omega}(t)$ evaluated at sequency m. Measuring the decay rate of the signal $\Gamma_2^m(T) = \sqrt{\langle \hat{\omega}_m^2(T) \rangle}$ after an evolution time T for different Walsh sequences $\{w_m(t/T)\}$ is equivalent to sampling the local Walsh spectrum $P_N(m)$, from which the local logical autocorrelation function $L_N(j)$ can be estimated by applying the inverse Walsh transform. The problem of recovering the autocorrelation function $R'(j)$ from the logical autocorrelation function $L_N(j)$ is addressed in the following

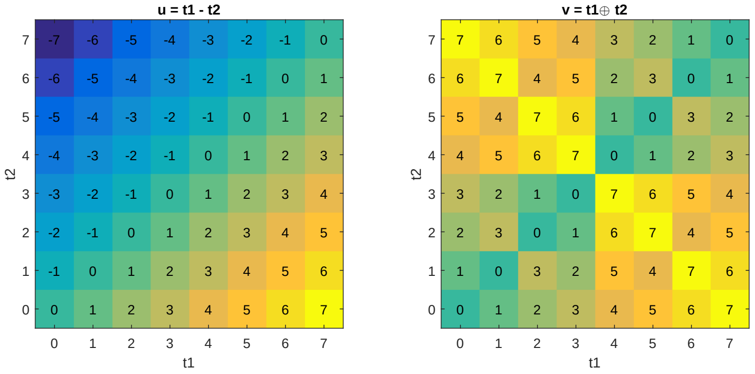

	0	1	2	3	4	5	6	7
7	-7	-6	-5	-4	-3	-2	-1	0
6	-6	-5	-4	-3	-2	-1	0	1
5	-5	-4	-3	-2	-1	0	1	2
4	-4	-3	-2	-1	0	1	2	3
3	-3	-2	-1	0	1	2	3	4
2	-2	-1	0	1	2	3	4	5
1	-1	0	1	2	3	4	5	6
0	0	1	2	3	4	5	6	7

	0	1	2	3	4	5	6	7
7	7	6	5	4	3	2	1	0
6	6	7	4	5	2	3	0	1
5	5	4	7	6	1	0	3	2
4	4	5	6	7	0	1	2	3
3	3	2	1	0	7	6	5	4
2	2	3	0	1	6	7	4	5
1	1	0	3	2	5	4	7	6
0	0	1	2	3	4	5	6	7

Figure 3-3: **Represent the arithmetic $u = (t_1 - t_2)$ and dyadic $v = (t_1 \oplus t_2)$ sampling domain.** The dyadic sampling domain is computed from the bitwise XOR operation of t_1 and t_2, which is equivalent to the nimber addition or Caley table of $\mathbb{Z}_2^4$.

sections.

3.1.2 Continuous representation of the autocorrelation function

An equivalent derivation of the expressions for the decay rate is introduced using a continuous representation of the autocorrelation function. We first define $d\mu(t_1, t_2) = dt_1 dt_2/T^2$ for $(t_1, t_2) \in \mathbb{R}^2([0, T[)$ as the integration measure on $\mathbb{R}^2([0, 1[)$, such that the second cumulant in Eq. (3.12) can be written as

$$\langle \hat{\omega}_m(T)^2 \rangle \;=\; \int\!\!\int d\mu(t_1, t_2) R(t_1 - t_2) w_m((t_1/T) \oplus (t_2/T)). \tag{3.24}$$

We then perform the change of variables $u = (t_1 - t_2) \in \mathbb{R}([-T, T[)$ and $v = ((t_1/T) \oplus (t_2/T)) \in \mathbb{R}([0, 1[)$, where the dyadic addition is carried out by continuously

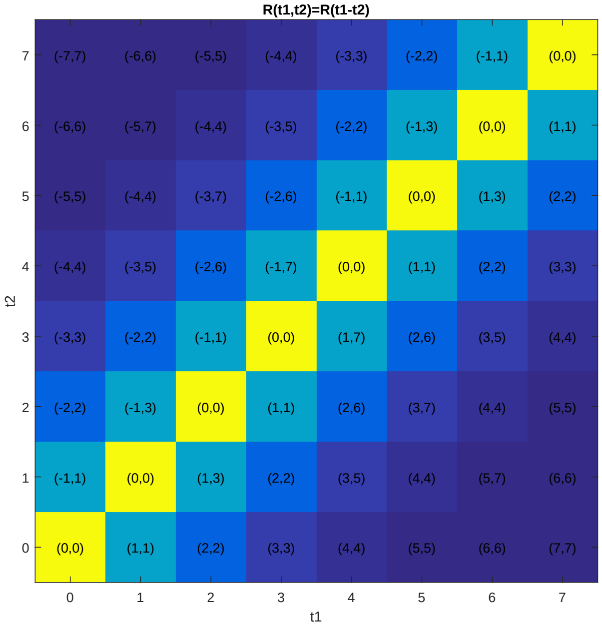

	0	1	2	3	4	5	6	7
7	(-7,7)	(-6,6)	(-5,5)	(-4,4)	(-3,3)	(-2,2)	(-1,1)	(0,0)
6	(-6,6)	(-5,7)	(-4,4)	(-3,5)	(-2,2)	(-1,3)	(0,0)	(1,1)
5	(-5,5)	(-4,4)	(-3,7)	(-2,6)	(-1,1)	(0,0)	(1,3)	(2,2)
4	(-4,4)	(-3,5)	(-2,6)	(-1,7)	(0,0)	(1,1)	(2,2)	(3,3)
3	(-3,3)	(-2,2)	(-1,1)	(0,0)	(1,7)	(2,6)	(3,5)	(4,4)
2	(-2,2)	(-1,3)	(0,0)	(1,1)	(2,6)	(3,7)	(4,4)	(5,5)
1	(-1,1)	(0,0)	(1,3)	(2,2)	(3,5)	(4,4)	(5,7)	(6,6)
0	(0,0)	(1,1)	(2,2)	(3,3)	(4,4)	(5,5)	(6,6)	(7,7)

Figure 3-4: **Represent the autocorrelation function $R(t_1, t_2) = R(t_1 - t_2) = \exp(-|t_1 - t_2|)$ of a stationary process on the dyadic grid up to order $n = 3$.** The labels indicate the coordinates $(u = t_1 - t_2, v = t_1 \oplus t_2)$. The diagonal elements correspond to regions where $u = t_1 - t_2$ is a constant.

extending the set of dyadic rational numbers of order n, $\mathbb{Q}_2(n) = \{z/2^n \mid z \in \mathbb{N}(n)\}$, to the set of real numbers on the unit interval, $\mathbb{R}([0, 1[)$. The sampling domain on the discrete grid set by the Walsh filters of order $n = 3$ is represented in Fig. 3-3.

We finally choose $d\nu(u, v)$ as the integration measure on $\mathbb{R}([-T, T[) \times \mathbb{R}([0, 1[)$, such that Eq. (3.24) can be written as

$$\langle \hat{\omega}_m(T)^2 \rangle \;=\; \int\!\!\int d\nu(u, v) R(u) w_m(v). \tag{3.25}$$

An an example, Figure 3-4 illustrates the autocorrelation function $R(t_1, t_2) = R(t_1 - t_2) = \exp(-|t_1 - t_2|)$ over the discrete sampling domain set by the Walsh filter $w_m(v)$. The integrals in Eq. (3.25) are solved by computing the overlap between the autocorrelation function $R(u)$ and the Walsh filter $w_m(v)$, which effectively correspond to adding and substracting the discrete elements of the autoccorelation function according to the sign of the Walsh filter. The labels indicate the (u, v) coordinates in

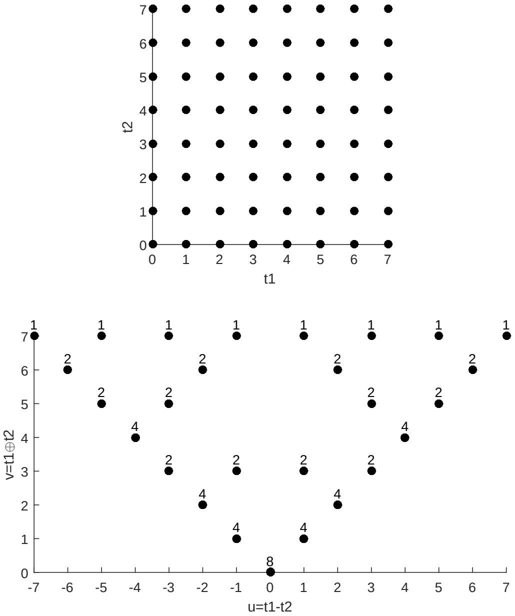

Figure 3-5: **Represent the arithmetic $u = (t_1 - t_2)$ and dyadic $v = (t_1 \oplus t_2)$ sampling domain.** Each sampling point of the arithmetic space is mapped to a sampling point in the dyadic space. The transformation from the arithmetic domain to the dyadic domain is however not injective; there exist distinct elements of the arithmetic domain that are mapped to the same elements in the dyadic domain. The number of elements (t_1, t_2) in the arithmetic domain that are mapped to the same element (u, v) in the dyadic domain is given by the transfer function $T(u, v)$. For example, the Walsh functions sample the zero time-lag elements of $c(t_1 - t_2)$ at $v = t_1 - t_2 = 0$ whenever $u = 0$ with $T(0, 0) = N$ degenerate elements. The long-time correlation elements $c(N - 1)$ are sampled only once at $u = N - 1$.

the discrete sampling domain, which show that the element $(0, 0)$ is sampled $N = 2^n$ times, the elements $(1, 1)$ and $(-1, 1)$ are sampled $N/2 = 2^{(n-1)}$ times, etc.

The degeneracy number of each element of the sampling domain is captured by the transfer function, $T(u, v)$, which is defined such that $d\nu(u, v) = dudvT^{-1}(v, u)$ and

$$\int T^{-1}(v,u)T(u,v')du = \delta(v - v') \tag{3.26}$$

$$\int T(u,v)T^{-1}(v,u')dv = \delta(u - u') \tag{3.27}$$

$$\int d\nu(u,v)T(u,v) = \int\int dudvT^{-1}(v,u)T(u,v) = 1. \tag{3.28}$$

The change in integration space associated with the change of variable from (t_1, t_2) to (u, v) is illustrated in Fig. 3-5.

Using the expression for the transfer function, Equation (3.25) becomes

$$\begin{aligned}
\langle \hat{\omega}_m(T)^2 \rangle &= \int\int dudv\ w_m(v)\ T^{-1}(v,u)\ R(u) && (3.29)\\
&= \int du\ R(u) \int dv\ w_m(v)\ T^{-1}(v,u) && (3.30)\\
&= \int dv\ w_m(v) \int du\ T^{-1}(v,u)\ R(u), && (3.31)
\end{aligned}$$

where the decay rate has two equivalent representations depending on the order in which the integration is carried out. The variance can thus be expressed in two equivalent ways.

First, we can write the variance in the *arithmetic* representation as

$$\langle \hat{\omega}_m(T)^2 \rangle = \int du\ R(u) F_m(u), \tag{3.32}$$

where $F_m(u) = \int dv\ w_m(v)\ T^{-1}(v,u)$ is the *autocorrelation filter* [72]. The decay rate is given by the overlap between the autocorrelation function and the autocorrelation filter generated by the modulation sequence.

Second, we can write the variance in the *dyadic* representation as

$$\begin{aligned}
\langle \hat{\omega}_m(T)^2 \rangle &= \int dv\ w_m(v)\ L(v) && (3.33)\\
&= P_m(T), && (3.34)
\end{aligned}$$

where $P_m(T)$ is the *local Walsh spectral density* or *local Walsh energy spectrum* defined as the Walsh transform of the *logical autocorrelation function*, $L(v)$, which is obtained from the *arithmetic autocorrelation function*, $R(u)$, through the application of the transfer function $T(u,v)$:

$$L(v) = \int duT^{-1}(v,u)R(u) \tag{3.35}$$

$$R(u) = \int dvT(u,v)L(v)dv. \tag{3.36}$$

The transfer function $T(u,v)$ converts the arithmetic autocorrelation function expressed in the arithmetic domain $(t_1 - t_2)$ to the logical autocorrelation function expressed in the dyadic domain $((t_1/T) \oplus (t_2/T))$. Because the autocorrelation function is even-symmetric about the origin, $R(t) = R(-t)$, the domain can be restricted to $u = (t_1 - t_2) \in \mathbb{R}([0,T[)$ by the change of variable $T'(u,v) = T(u,v)$ for $u = 0$ and $T'(u,v) = 2 \cdot T(u,v)$ elsewhere. The size of the transfer matrix then changes from $(2N - 1 \times N)$ to $(N \times N)$. In practice, the transfer function $T(u,v)$ performs a shuffling of the coefficients of $R(u)$, defined in the arithmetic domain to generate $L(v)$, defined in the dyadic domain [73].

Given a knowledge of the spectral density in the sequency domain, we can estimate the spectral density in the frequency domain by a applying series of linear transformations

$$P_W \xrightarrow{WT^{-1}} L_W \xrightarrow{T_{WF}} R_F \xrightarrow{FT} S_F, \tag{3.37}$$

where WT stands for Walsh Transform, FT stands for Fourier Transform, and T_{WF} stands for the transfer function, which converts from the dyadic time domain to the arithmetic time domain.

The Walsh sequences generate a complete set of digital filters that can be used to directly sample the coefficients of the spectral density in the sequency domain. An estimate of the autocorrelation function is obtained through a series of linear transformations without the need for undue approximations on the simplified representation of the filter in the frequency domain. The reconstruction protocol does not rely on any prior information about the field other than the assumptions of Gaussianity and stationarity, although additional assumptions about the characteristics of the stochastic process can be used to design more efficient sampling strategies. Future work will focus on comparing the performance of the proposed method with existing sampling protocols and exploring applications of the Walsh spectroscopy method to characterize the dynamics of ensembles of interacting spins and estimate the parameters of deterministic fields using asynchronous measurements, i.e., measurements performed without the ability to synchronize the sampling sequence with the sampled field.

Chapter 4

Environment-assisted quantum metrology with entangled states of electron spins in diamond

Quantum metrology explores quantum strategies such as the use of entanglement, discord, and squeezing to reduce the statistical error associated with the estimation of unknown physical parameters and ultimately attain the fundamental bounds set by the Heisenberg uncertainty relations. Quantum strategies have been explored in different physical implementations of a quantum probe to improve the performance of metrology tasks, including squeezed states, non-Gaussian spin states, and entangled states of many particles. Entangled states of electron spins have been proposed to enhance the performance of quantum sensors [74, 75], but their implementation in solid-state materials has been hindered by the difficulty of accessing ensembles of electron spins that can be prepared, manipulated, and measured with high fidelity. In this chapter, we introduce coherent control techniques to convert unknown quantum systems located in the environment of a quantum probe into quantum resources available for sensing time-varying fields with improved performance.

We experimentally demonstrate these techniques with a composite quantum system formed by the electron spins associated with optically-bright nitrogen-vacancy centers (NV) and other optically-dark paramagnetic centers (X) in an engineered diamond sample. We first identify the hyperfine components of the spin Hamiltonian of two hybrid electron-nuclear spin systems associated with two unknown paramagnetic centers (X_1, X_2) located in the environment of a single NV center in diamond. We then initialize and measure the quantum state of two X electron spins using cross-polarization techniques, coherent feedback, and repetitive quantum measurements. We finally create and exploit entangled states of two and three electron spins to estimate the amplitude of time-varying magnetic fields. Our results demonstrate an approach to environment-assisted quantum sensing and quantum-enhanced metrology with electron spins in diamond.

4.1 Quantum system identification

An essential requirement for achieving environment-assisted quantum metrology is the ability to identify unknown quantum systems located in the environment of a quantum probe. In this section, we introduce spectroscopic techniques to estimate the components of the internal Hamiltonian of some unknown quantum systems located in the environment of a single quantum probe. We then experimentally demonstrate these techniques to measure the spin Hamiltonian of two hybrid electron-nuclear spins systems, including the principal values and orientation of the hyperfine tensor $\underline{\underline{A}}$. These two unknown paramagnetic centers are possibly nitrogen-related defects, dangling bonds, or other impurities located inside the diamond or near its surface.

4.1.1 Identify two unknown paramagnetic centers in the environment of a single nitrogen-vacancy center in diamond

Magnetic double-resonance control sequences extract spectral information about electron spins in the environment of a single NV center. The spin-echo sequence (SE) is the simplest instance of a pulse decoupling sequence with a single decoupling pulse applied midway the evolution period. SE suppresses the contribution from the secular dipolar interaction terms from all subsets of the environment. The recoupled spin-echo sequence (SEDOR), similar to the spin-echo double-resonance sequence, decouples the quantum probe from its environment, but selectively recouples the dipolar interaction with a resonant subset of the environment by simultaneously applying decoupling and recoupling pulses on both the quantum probe and the environment [76]. The recoupled spin-echo sequence is one instance of magnetic double resonance sequences, also called double electron-electron resonance (DEER) or pulse electron double resonance (PELDOR).

We measure the electron spin resonance spectrum of the electron spin environment of a single NV center by varying the frequency of the recoupling pulse in the SEDOR sequence (Fig. 4-1). In our experiment, the NV electron spin is prepared in a coherent superposition of states with a $\pi/2$ pulse and decoupled from its environment with a series of resonant microwave π pulses. The magnetic dipolar interaction with nearby electron spins is selectively recoupled by applying a series of recoupling π pulses on the electron spins. The series of decoupling and recoupling pulses effectively decouple the NV electron spin from dephasing noise, while selectively recoupling the dipolar interaction terms to nearby electron spins whose resonance frequency is included in the spectral bandwidth of the excitation pulses. The measured fluorescence signal decreases whenever electron spins are resonantly excited by the microwave excitation pulses; varying the frequency of the microwave excitation pulses produces an electron resonance spectrum from which the resonance frequencies of two hybrid electron-nuclear spin systems are determined.

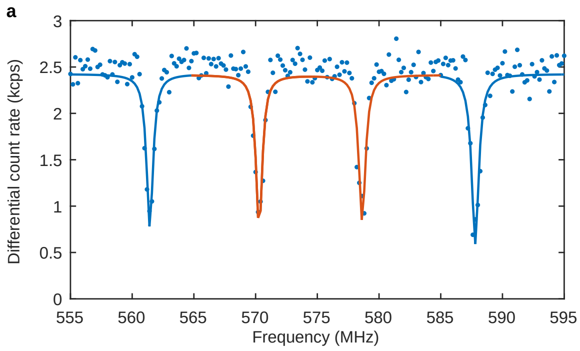

Figure 4-1: **Measure the electron spin resonance spectrum of two hybrid electron-nuclear spin systems in the environment of a single NV center using a recoupled spin-echo sequence.** The static magnetic field is aligned along the molecular axis of the NV center. The esr spectrum of the environment shows four spectral peaks centered around the resonance frequency expected for free electrons. The two pairs of inner and outer spectral lines correpond to two paramagnetic centers formed by an electron spin interacting with a nearby nuclear spin via hyperfine interaction. The hyperfine splitting for the two X electron spins is 26.4 MHz and 8.3 MHz respectively.

The electron spin resonance spectrum measured with the static magnetic field oriented along the molecular axis of the NV center shows four resonant transitions centered at the single resonance transition expected for free electrons at $\omega_S = \gamma_e B_0$. We associate these four resonant transitions with the existence of two hybrid electron-nuclear spin systems associated with two nearby paramagnetic centers.

The two unknown paramagnetic centers are modeled by two hybrid electron-nuclear spin systems formed by a single electron spin ($S = 1/2$) interacting via hyperfine interaction with a single nuclear spin ($J = 1/2$). The Hamiltonian of a single hybrid electron-nuclear spin system is

$$\mathcal{H} = \beta_e/\hbar\, \underline{B}_0 \cdot \underline{\underline{g}} \cdot \underline{S} + \underline{S} \cdot \underline{\underline{A}} \cdot \underline{J} - g_n \beta_n/\hbar\, \underline{B}_0 \cdot \underline{J}, \tag{4.1}$$

where $\beta_e/\hbar = 2\pi{\cdot}13.996$ GHz T^{-1} is the Bohr magneton, $\beta_n/\hbar = 2\pi{\cdot}7.623$ MHz T^{-1} is the nuclear magneton, g_n is the g-factor of the unknown nuclear spin, $\underline{\underline{g}}$ is the g tensor of the electron spin, $\underline{\underline{A}}$ is the hyperfine tensor describing the hyperfine interaction between the electron and nuclear spins, $\underline{B}_0$ is the static magnetic field, and $\underline{S}$ and $\underline{J}$ are the vector operators for the electron and nuclear spins. We assume the hyperfine tensor to be an axially symmetric tensor with $A_x = A_y = A_\perp$ and $A_z = A_\parallel$, and the g tensor to be an isotropic tensor, $g = g_x = g_y = g_z$, such that the spin Hamiltonian is fully determined by six unknown components, ($A_\perp$, A_y, α, β, g, g_n), where α and β are the Euler angles defining the orientation of the molecular axis of the X centers with respect to the molecular axis of the NV center. These assumptions make the problem of identifying the unknown components of the spin Hamiltonian tractable experimentally.

4.1.2 Estimate the parameters of the internal spin Hamiltonian of two unknown paramagnetic centers in diamond

The resonance frequencies of the electron spin double-resonance spectrum depend on the strength of the hyperfine interaction between the electron spin and its nearby nuclear spin, which itself depends on the strength and orientation of the static magnetic field with respect to the orientation of the principal axes of the hyperfine tensor (molecular frame). We estimate the parameters of the spin Hamiltonian of two unknown paramagnetic centers in the environment of a single NV center by monitoring the resonance frequencies of the SEDOR spectrum as a function of the strength and orientation of the static magnetic field, which is varied by translating and rotating a permanent magnet with respect to the diamond sample. The spatial components of the static magnetic field in the crystallographic frame of the diamond sample are estimated with the NV center acting as a vectorial magnetometer.

Vary the strength and orientation of the static magnetic field

The strength and orientation of the static magnetic field is varied by translating and rotating a permanent magnet with respect to the diamond sample (Fig. 4-2). The diamond sample is cut with its edge directed along the 110 crystallographic axis, such that the 111 molecular axis of the NV center lies in the 110 × 001 crystallographic plane with its transverse projection oriented towards the 110 edge of the diamond sample rather than towards its corner, as it would have been the case for a diamond sample with its edge oriented along the 100 crystallographic axis.

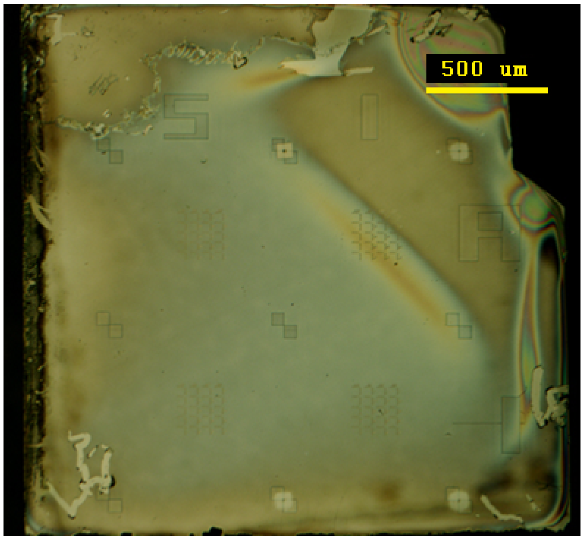

Figure 4-2: **Observe from above the Terra-B diamond sample when it is mounted in the confocal microscope on top of the coplanar waveguide.** The implantation pattern is facing down towards the coplanar waveguide and the microscope objective. The bottom edge of the sample is oriented along the 110 direction, the up edge of the sample is oriented along $1\bar{1}0$, and the top face of the sample facing the viewer when looking down at the sample is oriented along the 001 direction. The permanent magnet is oriented and translated along the 110 direction so as to vary the polar angle θ of the static magnetic field in the azimuthal plane $\phi = 0$.

A 1 $''$ cubic magnet is mounted with its magnetization axis oriented along the edge of the diamond sample. The orientation of the magnet is defined in spherical coordinates with respect to the molecular axis of the NV center. When the magnet is placed exactly on top of the NV center, the static magnetic field at the position of the NV center is oriented along the 110 direction. Translating the magnet along its magnetization axis rotates the magnetic field in the 110×001 crystallographic plane, and thus corresponds to a rotation of the polar angle θ in the molecular frame of the NV center. Rotating the magnet with respect to the diamond edge corresponds to a rotation of the azimuthal angle ϕ in the molecular frame of the NV center.

Estimate the strength and orientation of the static magnetic field

The spatial components of the static magnetic field in the molecular frame of the NV center are estimated by using the NV center as a vectorial magnetometer. The hyperfine interaction between the NV electron spin and the host N-15 nuclear spin modulates the spin-echo signal at the nuclear frequencies, from which the transverse components of the static magnetic field in the NV molecular frame is inferred. Measuring the electron spin resonance spectrum of an ensemble of NV centers provides additional information about the strength and orientation of the static magnetic field.

The magnet is translated along the 110 direction over a displacement range of 50 mm with a linear actuator. Translating the magnet induces a rotation of the polar angle θ of the static magnetic field in the azimuthal plane $\phi = 0$. The resonance frequency of the NV electron spin in the $ms \in \{0, -1\}$ manifold is measured at each position of the magnet with a cw-ESR sequence (continuous driving of the NV electron spin under optical illumination with a carrier microwave signal of varying frequency). The measured values of the resonance frequency at each position of the magnet, $\{\nu(x)\}$, do not uniquely determine the strength and orientation of the magnetic field; they rather generate a surface of possible values for the strength and polar orientation of the magnetic field, $\mathcal{S} = \{(B_0, \theta) \mid \nu(B_0, \theta) = \nu(\vec{x})\}$, i.e., there are multiple choices of the strength and orientation of the magnetic field that give rise to the same resonance frequency.

The strength and orientation of the magnetic field at each position of the magnet is uniquely determined by measuring both the resonance frequency of the NV electron spin with a cw-esr sequence and the hyperfine-modulated signal of the NV-N electron-nuclear spin system with a spin-echo sequence. In the presence of a static magnetic field oriented along a different direction than the molecular axis of the NV center, the energy levels of the NV electron spin are mixed with the energy levels of the N nuclear spin and the spin-echo signal is modulated at the nuclear frequencies and their combinations, $\{\omega_1, \omega_0, \omega_1 \pm \omega_0\}$. This modulation of the spin-echo signal is the so-called electron spin-echo envelope modulation (ESEEM). The nuclear frequencies, which can be computed numerically by diagonalizing the spin Hamiltonian of the electron-nuclear spin system with $S = 1$ and $I = 1/2$ for an intrinsic N-15 nuclear spin, correspond to the quantization energies of the nuclear spin conditional on the NV electron spin being in the state $ms = 0$ or $ms = 1$.

We numerically compute the resonance frequencies of the NV center for different values of the strength and orientation of the static magnetic field. For each position of the magnet, we use the set of numerically computed values, $\{\nu(B_0, \theta)\}$, to determine the one-dimensional curve of field parameters (B_0, θ) that provides a resonance frequency equal to the measured resonance frequency $\nu(x)$. This one-dimensional curve corresponds to the interesection between the surface of all resonance frequencies ($\{\nu(B_0, \theta)\}$) and the plane of constant height set by the measured frequency ($\nu(x)$) at a specific position of the magnet (x). We then numerically simulate the modulated spin-echo spectrum for all field parameters on the one-dimensional curve. We finally perform a table search to identify the parameters of the static field (B_0, θ) that minimize the distance between the measured ESEEM spectrum and the simulated ESEEM spectra (Fig. 4-3).

The set of cw-esr spectra measured for an ensemble of NV centers match the cw-esr spectra simulated using the parameters of the static magnetic field estimated from cw-esr and ESEEM measurements on a single NV center (Fig 4-4), validating the assumption that the magnet is translated in the azimuthal plane $\phi = 0$. These results show that overlapping the spectral doublets of two spectral classes provides a convenient method to orient the magnetization axis of the magnet in the azimuthal plane $\phi = 0$.

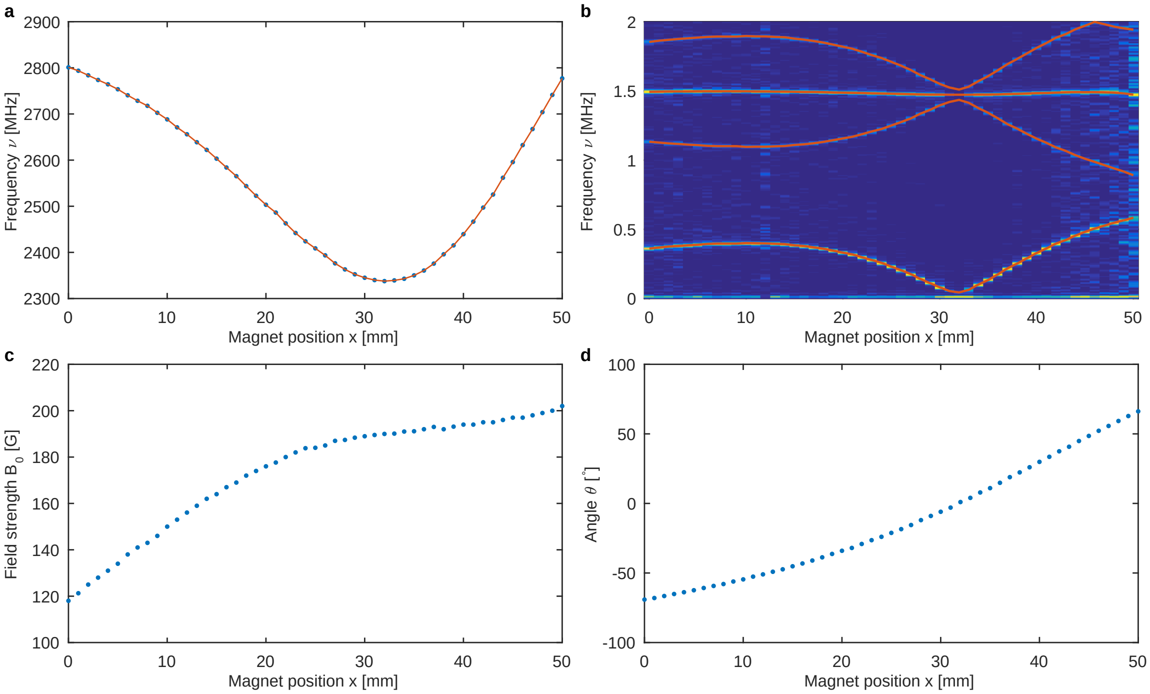

Figure 4-3: **Estimate the strength and orientation of the static magnetic field as a function of the longitudinal position of the permanent magnet from electron spin resonance measurements on the NV center. a**, Resonance frequency of the NV electron spin measured from cw-esr measurements on the NV center. The solid line is a numerical calculation of the resonance frequency calculated by diagonalizing the spin Hamiltonian of the NV center using the estimated field parameters. **b**, Spectrum of the modulated spin-echo signal obtained from spin-echo measurements on the NV center. The solid line is a numerical calculation of the nuclear frequencies calculated by diagonalizing the spin Hamiltonian of the NV center using the estimated field parameters. **c-d,** Strength and orientation of the static magnetic field estimated from cw-esr and ESEEM measurements on the NV center.

The electron spin resonance spectrum for an ensemble of NV centers gives four pairs of spectral doublets associated with all of the four possible molecular orientations of the NV center in the diamond crystal. When the static magnetic field is oriented along the 111 direction, the resonance frequencies of three out of four NV families are overlapping. When the static magnetic is oriented along the 001 direction, the resonance frequencies of all of the four NV classes are degenerate. When the rotation of the magnetic field is restricted to the 110×001 plane the resonance frequencies of at least two out of four classes are overlapping. This provides a convenient approach to align the static magnetic field along a specific crystallographic direction.

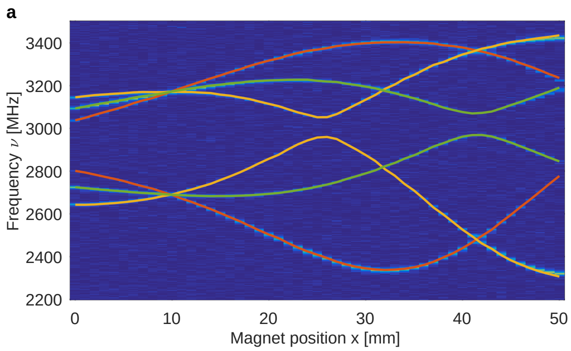

Figure 4-4: **Measure the cw-esr spectrum of an ensemble of NV centers oriented along all of the four possible crystallographic orientations in the diamond lattice.** The solid lines are the resonance frequencies calculated numerically by diagonalizing the spin Hamiltonian of an ensemble of NV centers with the estimated values of the field parameters. Because the magnet is translated in the azimuthal plane $\phi = 0$, the spectral lines of two out of four NV families are degenerate, such that only three out of four spectral doublets are visible in the measured spectrum.

Estimate the components of the hyperfine tensor

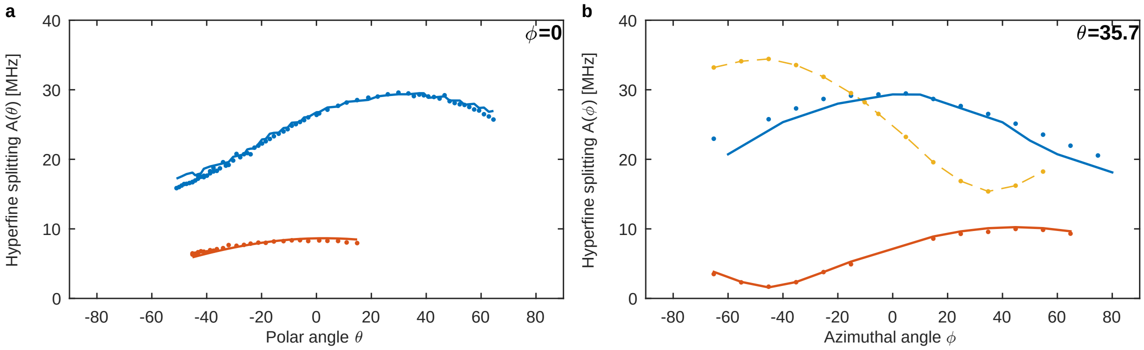

Figure 4-5: **Estimate the components of the hyperfine tensor of two hybrid electron-nuclear spin systems associated with two paramagnetic centers in diamond. a**, Hyperfine splitting of the spectral doublets of two X electron spins as a function of the polar angle of the static magnetic field with respect to the molecular axis of the NV center in the azimuthal plane $\phi = 0$. The solid line is a numerical fit to the eigenvalues of an axially-symmetric hyperfine tensor with four free parameters. **b**, Hyperfine splitting of the spectral doublets of two X electron spins as a function of the azimuthal angle of the static magnetic field measured at the polar angle $\theta = 35.7°$. A third spectral doublet is identified, possibly indicating the presence of a third unknown paramagnetic center in the environment of the single NV center.

We estimate the components of the hyperfine tensor describing the interaction between the electron spin and the nuclear spin of the two unknown paramagnetic centers by monitoring the change in the hyperfine splitting of the spectral doublets as a function of the orientation of the static magnetic field defined with respect to the molecular axis of the NV center. The experimental data reported in Fig. 4-5 are fitted to the values computed numerically by diagonalizing the Hamiltonian expressed in Eq. (4.1). Assuming $g = 2.002$, a numerical fit to the experimental data gives X_1=($A_\perp = 17.16$, $A_z = 29.45$, $\alpha = 87.07$, $\beta = 0.30$) for the first paramagnetic center and X_2=($A_\perp = 1.58$, $A_z = 11.22$, $\alpha = 65.72$, $\beta = 44.88$) for the second paramagnetic center (X_2). These parameters do not match the hyperfine values of known defects reported in the scientific literature, possibly indicating that we are dealing with yet unstudied paramagnetic centers in diamond.

Estimate the components of the dipolar tensor

We located two unknown paramagnetic centers in the environment of a single NV center by measuring the angular dependence of the dipolar interaction strength on the static magnetic field. The secular dipolar Hamiltonian for heteronuclear spins *quantized along the static magnetic field*, which describes the magnetic dipolar interaction between spins having different Zeeman energies, is usually given by

$$\mathcal{H}_{\mathrm{SI}} \quad = \quad d(\alpha) \cdot 2S_z I_z, \tag{4.2}$$

where $d(\alpha) = -(\mu_0/4\pi)\hbar^2\gamma_S\gamma_I r^{-3} P_2(\cos\alpha)$ is the dipolar interaction strength and $P_2(\cos(\alpha)) = (3\cos(\alpha)^2 - 1)/2$ is the geometric scaling factor, which depends on the angle α between the interspin vector $\underline{r}$ and the static magnetic field $\underline{B}_0$. Because the NV electron spin is effectively quantized along its zero-field splitting oriented along the 111 crystallographic direction for small values of the static magnetic field, the geometric scaling factor for the NV–X electron spin system is

$$P_2(\alpha, \theta) = [\cos(\theta) - 3\cos(\alpha) \cdot \cos(\alpha - \theta)]/3, \tag{4.3}$$

where α is the angle between the interspin vector $\underline{r}$ and the static magnetic field $\underline{B}_0$ and θ is the angle between the molecular axis of the NV center and the static magnetic field. Equation (4.3) is valid under the stringent assumption that the two electron spins lie in the same azimuthal plane $\phi = 0$. This assumption can be lifted by measuring the dipolar interaction strength between the two electron spins in more than one azimuthal plane.

We measure the components of the dipolar tensor between a single NV electron spin and two X electron spins by monitoring the change in the dipolar interaction strength as a function of the polar angle θ of the static magnetic field with respect to the molecular axis of the NV center in the azimuthal plane set by $\phi = 0$. The dipolar interaction strength is estimated from the coherent modulation of the recoupled spin-echo experiments (SEDOR) measured up to 72 μs.

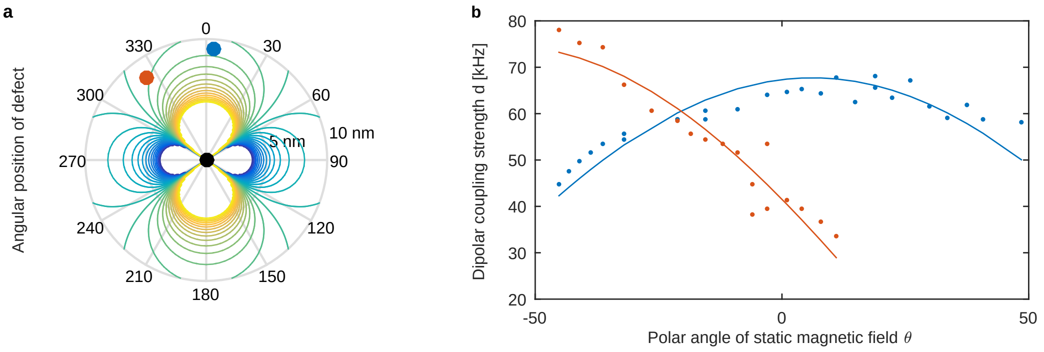

Figure 4-6: **Estimate the dipolar components of hybrid electron-nuclear spin systems associated with unknown paramagnetic centers in diamond.** The solid line is a numerical fit to the eigenvalues of an axially-symmetric hyperfine tensor with four free parameters. **a,** Polar plot indicating the location of two unknown paramagnetic centers in the environment of a single nitrogen-vacancy center in diamond assuming they are located in the same azimuthal plane $\phi = 0$. **b,** Measured dipolar coupling constants for two electron spins as a function of the polar angle of the static magnetic field with respect to the molecular axis of the NV center in the azimuthal plane $\phi = 0$. The solid line is a fit to the geometrically-scaled dipolar coupling constant.

We fit the experimental data reported in Fig. 4-6 to the dipolar coupling constant expressed in Eq. (4.3) to obtain ($\alpha = 4.1°$, $d = 67.9$ kHz) for the first X electron spin and ($\alpha = -36.1°$, $d = 86.8$ kHz) for the second X electron spin (modulo an indistinguishable π factor in the estimation of the angle α). These values correspond to an interspin distance between the X paramagnetic centers and NV center of $r_1 = 9.2$ nm and $r_2 = 8.4$ nm. Assuming the two electron spins to lie in the same azimuthal plane $\phi = 0$, the internuclear distance between the two electron spins computed by solving $r_{12}^2 = r_1^2 + r_2^2 - 2r_1r_2\cos(\alpha_1 - \alpha_2)$ is $r_{12} = 6.1$ nm. This distance corresponds to a dipolar coupling constant of $d_{12} = 65.2$ kHz when the magnetic field is aligned along the molecular axis of the NV center. We could not detect the coupling between the two X electron spins, possibly indicating that the two paramagnetic centers are located further apart in different azimuthal planes.

4.2 Quantum system integration

Quantum system integration aims at combining quantum resources extracted from the environment of a quantum probe into a large-scale quantum system that can efficiently process quantum information. Integrating additional quantum resources into an existing quantum system requires the ability to prepare and maintain the quantum system in a state of low entropy, create quantum correlations between spatially-remote quantum subsystems, and perform measurements on these quantum subsystems without disturbing the rest of the system.

Preparing unknown quantum systems in a state of low entropy can be achieved by using passive or active cooling approaches. Passive cooling approaches increase the intrinsic polarization bias of the quantum system by increasing the occupation probability of the lowest energy state, e.g., by applying a strong external magnetic field or decreasing the temperature of the physical system. Active cooling approaches rely on the existence and accessibility of a physical mechanism to extract entropy out of a quantum system and transfer that entropy into an external heat bath, e.g., via optical pumping. Quantum measurements combined with coherent feedback control techniques and cross-polarization techniques enable reducing the entropy of a quantum system that lacks an accessible physical mechanism for entropy extraction.

4.2.1 Initialize quantum systems using coherent feedback control

Quantum measurements use quantum probes to extract information about quantum systems that cannot be directly measured using projective measurements. Quantum measurements are performed in two steps: (1) correlate the state of the quantum probe with the state of the quantum system via direct or mediated interaction and (2) perform a (strong) projective measurement on the quantum probe to infer the state of the quantum system from the measurement outcomes. Quantum measurements enable identifying unknown quantum systems by gaining information about their physical properties, such as their structure, dynamics, dimensionality, and topology.

Quantum measurements can also be used to reduce the entropy of unknown quantum systems.

Mathematically, quantum measurements are described by a set of operators $\{A_n\}$ that satisfy $\sum_n A_n^\dagger A_n = \mathbb{1}$, where $\mathbb{1}$ is the identity operator [77]. The polar decomposition theorem states that any operator A_n can be written as $A_n = U_n \Pi_n$, where U_n is a unitary operator and Π_n is a positive operator. Projective measurements are described by a set of projection operators $\{\Pi_n\}$ with $\Pi_n^2 = \Pi_n$ (idempotent) and $\sum \Pi_n^\dagger \Pi_n = \sum \Pi_n = I$, where $\Pi_n = \Pi_n^\dagger$ is a positive Hermitian operator with a complete set of real eigenvalues greater or equal than zero, which thus represents a physical observable associated with a measurable quantity. According to the measurement postulate, projective measurements project the state of a quantum system onto the subpace associated with the n-th measurement outcome, Π_n, such that the density operator collapses to $\tilde{\rho}_n = \frac{\Pi_n \rho \Pi_n}{\mathrm{Tr}\{\Pi_n \rho \Pi_n\}} = \Pi_n$ with probability $p_n = \mathrm{Tr}\{\Pi_n \rho \Pi_n\} = \mathrm{Tr}\{\Pi_n \rho\}$. Projective measurements are specific instances of quantum measurements with $U_n = I$.

Measuring the quantum system in the $\sigma_{\vec{n}}$ basis requires choosing an interaction operator that rotates the state of the quantum probe by an amount proportional to the population of the quantum system in the eigenbasis of $\sigma_{\vec{n}}$, e.g., choosing $\sigma_2 \otimes \sigma_{\vec{n}}$ to generate the joint unitary operator $U_{\vec{n}} = e^{-i\theta\sigma_1 \otimes \sigma_{\vec{n}}/2}$ for a quantum probe initialized in a polarized state $\rho_\alpha = (\sigma_0 + \alpha\sigma_3)/2$.

Classical measurements with correlating gates

If the state of the quantum system commutes with the measurement operator U_n, the quantum system is not perturbed during the joint unitary evolution with the quantum probe, even though it becomes correlated with the quantum probe, as quantified by the increase in mutual information. Although the projective measurement on the quantum probe does not disturb the state of the quantum system, the state of knowledge of the observer described by the density operator must still be updated based on the information extracted. The quantum measurement thus acts as a classical measurement, in the sense that the change in the density operator is fully described by classical probability theory, e.g., using the Bayesian formalism.

Correlating gates that act on state operators that are diagonal in the measurement basis $\sigma_{\vec{n}}$ implement classical measurements that increase the state of knowledge of the observer about the state of the system. To understand that fact, let's consider the state of an initially uncorrelated bipartite quantum system $\rho_{\alpha\beta} = \rho_\alpha \otimes \rho_\beta$, where the marginal states $\rho_\alpha = \sum_n \lambda_n^\alpha \pi_n^\alpha$ and $\rho_\beta = \sum_n \lambda_n^\beta \pi_n^\beta$ are diagonal in the eigenbasis of $\sigma_{\vec{n}}$. The joint state

$$\begin{aligned} \rho_{\alpha\beta} &= \sum_{n_1,n_2} \lambda_{n_1}^\alpha \lambda_{n_2}^\beta \pi_{n_1}^\alpha \otimes \pi_{n_2}^\beta && (4.4) \\ &= \sum_n \lambda_n^{\alpha\beta} \pi_n^{\alpha\beta} && (4.5) \end{aligned}$$

is diagonal in the joint basis defined by the projection operators $\pi_n^{\alpha\beta} = \pi_{n_1}^\alpha \otimes \pi_{n_2}^\beta$.

In general, $\rho = \sum_n \lambda_n \pi_n$, where $\lambda_n = \prod_{j=1}^N \lambda_{n_j}$ is the occupation probability of the n-th energy level and $\pi_n = \bigotimes_{j=1}^N \pi_{n_j} = |n\rangle\langle n|$ is the projection operator on the n-th energy eigenstate $|n\rangle = |n_1 \cdots n_N\rangle$, with $n = (n_1 n_2 ... n_N)_2$ denoted as a N-bit binary string, where N is the number of qubits in the multipartite quantum system. For a bipartite quantum system with $N_{AB} = N_A + N_B$, the dimension of the joint Hilbert space is $d_{AB} = d_A \cdot d_B = 2^{N_A} 2^{N_B} = 2^{N_{AB}}$.

If the outcome of the projective measurement on the quantum probe is discarded, the resulting effect on the state of the quantum system is dephasing. The state of the quantum system after such *unconditional measurements* is described by a statistical mixture over all possible measurement outcomes, $\rho^\beta = \sum_n p_n \rho_n^\beta$. If the state of the quantum system is updated based on the outcome of the projective measurement on the quantum probe, the purity of the quantum system is increased. Implementing such *conditional measurements* rely on the ability to perform single-shot measurements of the state of the probe, i.e., to estimate the measurement outcome after a single trial rather than after averaging over many repetitions of the measurement.

Quantum measurements with entangling gates

If the state of the quantum system does not commute with the measurement operator U_n, i.e., the density matrix is not diagonal in the measurement basis, the quantum system becomes entangled with the quantum probe during the joint evolution period and the projective measurement on the quantum probe disturbs the state of the quantum system, an effect that is referred to as the measurement backaction. The strength of the backaction depends on the strength of the quantum measurement or the amount of quantum correlations created between the quantum system and the quantum probe, which depends on the coupling rate between the quantum system and the quantum probe and the duration of the interaction period.

Because the backaction induced on quantum systems by quantum measurements is equivalent to the action of a unitary operation on the state of quantum systems, measurement backaction can be used to manipulate the state of quantum systems. The state of the system is steered towards a specific target state by repeating the quantum measurement with the measurement strength updated adaptively. This requires the ability to update in real-time the strength of the measurement conditional on the measurement outcome.

Quantum measurements using classical and coherent feedback control

Classical feedback control can be used to initialize the state of a quantum system into an arbitrary pure state by applying a unitary transformation on the quantum system conditional on the outcome of the projective measurement on the probe. Coherent feedback control replaces classical feedback operations with coherent feedback operations that are described by a joint unitary operator acting on the joint system.

Extract entropy using coherent feedback control

The requirement for preparing a quantum system in a state of low entropy is the existence of a physical mechanism for extracting entropy out of the quantum system. We consider the experimental situation where the quantum system lacks a direct physical mechanism to reduce its entropy, but the quantum probe possesses a physical mechanism to reduce its entropy on a timescale faster than the relaxation time of the quantum system. Extracting entropy out of the quantum system can be achieved by implementing an amplitude damping channel using a coherent feedback protocol. The quantum circuit that implements coherent feedback to reduce the entropy of a bipartite quantum system of two qubits is shown in Fig. 4-7.

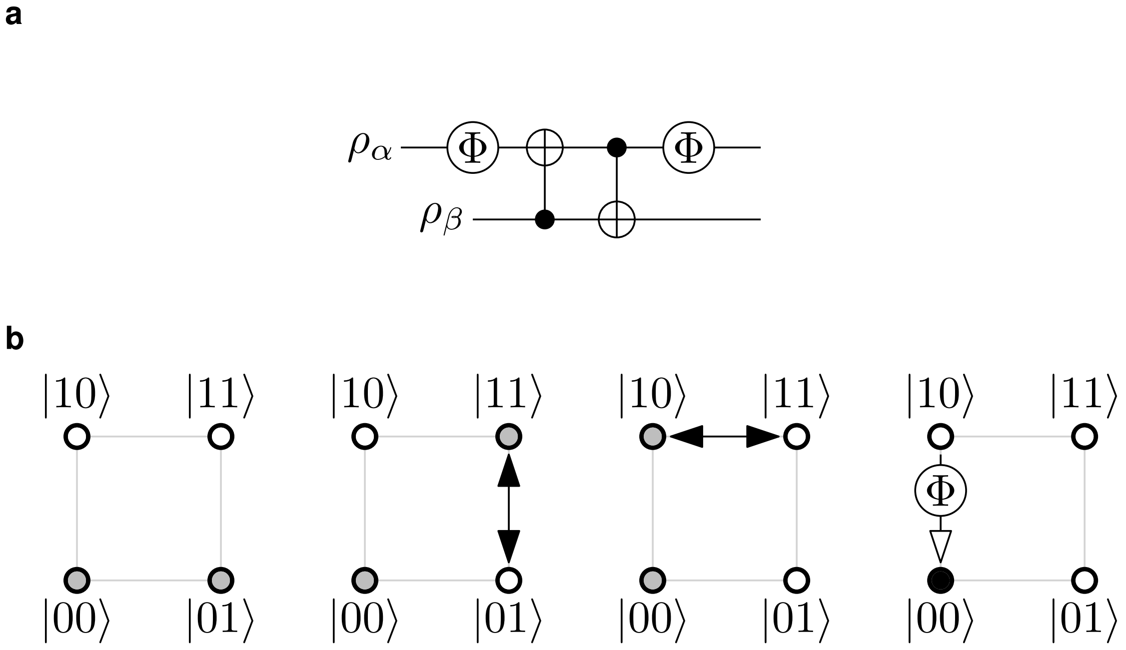

Figure 4-7: **Initialize quantum systems using coherent feedback control.** **a**, Quantum circuit to initialize a two-qubit system in a pure state using coherent feedback control when the first qubit possesses an accessible physical mechanism to reduce its entropy, e.g., via optical pumping. The dissipative channel Φ initializes the first qubit in a pure state and the two $\mathrm{C}_\alpha\mathrm{NOT}_\beta$ and $\mathrm{C}_\beta\mathrm{NOT}_\alpha$ gates exchanges the state of the first qubit with the state of the second qubit. **b**, The initial state of the two-qubit system is a maximally mixed state with equal occupation probability of all four basis states. Applying a dissipative gate on the first qubit initializes the state of the first qubit, while leaving the state of the second qubit in a maximally mixed state. The two controlled-NOT gates exchange the state of the first qubit with the state of the second qubit, leaving the first qubit in a maximally mixed state and the second qubit in a polarized pure state. The last dissipative gate initializes the state of the first qubit, such that the two-qubit system is prepared into a polarized pure state.

Assuming perfect unitary operations, the quantum circuit shown in Fig. 4-7 simulates the action of an amplitude damping channel acting on the quantum system with a combination of two controlled-NOT operations and one projective measurement. The first controlled-NOT operation correlates the state of the quantum system with the state of the quantum probe. The second controlled-NOT operation performs a coherent feedback operation that flips the state of the quantum system conditional on the state of the quantum probe having been flipped by the first controlled-NOT operation. The projective measurement resets the state of the quantum probe so that it can be reused in a cycling process.

In general, coherent feedback control techniques reduce the entropy of a quantum system by performing a quantum measurement on the quantum system with the aid of a quantum probe and coherently updating the state of the quantum system towards a desired target state, e.g., its ground state. To better understand the principle of entropy extraction using coherent feedback control, let's consider a bipartite quantum system formed by a single quantum probe and some unknown quantum system with vanishing initial correlations, such that the joint state is given by a separable product state $\rho_{\alpha\beta} = \rho_\alpha \otimes \rho_\beta$. The state space of the joint system is the Hilbert space $\mathcal{H}_{\alpha\beta} = \mathcal{H}_\alpha \times \mathcal{H}_\beta$ with dimension $d_{\alpha\beta} = d_\alpha \cdot d_\beta$. The quantum probe is initialized in a pure state $\rho_\alpha = \pi_0$ such that $S(\rho_\alpha) = 0$, whereas the quantum system is initialized in a maximally mixed state with $S(\rho_\beta) = \log d_\beta$, where d_β is the dimension of the Hilbert space of the quantum system. The quantum mutual information $I(\rho_{\alpha\beta}) = S(\rho_{\alpha\beta}||\rho_\alpha \otimes \rho_\beta) = S(\rho_\alpha) + S(\rho_\beta) - S(\rho_{\alpha\beta}) = 0$ is zero, as expected in the absence of correlations between the quantum system and the quantum probe.

Reducing the entropy of a quantum system by applying a unitary operation on the joint system requires finding and applying the joint unitary operation $U = \text{argmin}\{S(\rho_\beta) \mid \rho_\beta = \text{Tr}_\alpha\{U\rho_{\alpha\beta}U^\dagger\}\}$ that minimizes the entropy of the marginal state ρ_β on the unitary orbit $\mathcal{O}_\rho = \{\rho'_{\alpha\beta} = U\rho_{\alpha\beta}U^\dagger\}$. The unitary orbit $\mathcal{O}_\rho$ defines an isentropic manifold $S(\rho_{\alpha\beta}) = \text{cst.}$ for the joint state. For a separable state, $\rho_{\alpha\beta} = \rho_\alpha \otimes \rho_\beta$, this unitary operation corresponds to a permutation of the eigenvalues of the joint state [78]. The permutation operation is implemented with two successive controlled-NOT operations, $\text{C}_\beta\text{NOT}_\alpha$ followed by $\text{C}_\alpha\text{NOT}_\beta$. The $\text{C}_\beta\text{NOT}_\alpha$ operation inverts the state of the quantum probe conditional on the state of the quantum system. For a system of two spins with resolved couplings, the controlled-NOT operations can be implemented with selective π pulses. For a system of two spins with unresolved couplings, the controlled-NOT operations can be implemented using a combination of non-selective pulses and joint evolution periods under the interaction Hamiltonian.

Reducing the entropy of a quantum system by applying a non-unitary dissipative gate such as an amplitude damping channel requires constructing $\Phi(\rho_S) = \rho'_S$ such that $S(\rho_S) \geq S(\rho'_S) \geq 0$, with the right equality in the case of a perfect channel, which maps any mixed quantum state to a pure state, e.g., $\Phi : \rho \mapsto \Pi_0 \ \forall \rho$, where Π_0 is the projector associated with the ground state manifold. In general, the action of an amplitude damping channel on an arbitrary quantum state can be written as

$$\Phi : \rho \mapsto \rho' = \sum_{k=1}^{r} A_k \rho A_k^{\dagger}, \tag{4.6}$$

where $A_1 = \begin{bmatrix} 1 & 0 \\ 0 & \sqrt{1-p} \end{bmatrix}$ and $A_2 = \begin{bmatrix} 0 & \sqrt{p} \\ 0 & 0 \end{bmatrix}$ for $r = 2$. The set of discrete operators $\{A_k\}$ are the Kraus operators for the amplitude damping channel, which satisfy the completeness relation $\sum_{k=1}^{r} A_k^{\dagger} A_k = \mathbb{1}$. We can verify that $\Phi : \rho = \mathrm{diag}(\lambda_1, \lambda_2) \mapsto \mathrm{diag}(\lambda_1 + p\lambda_2, (1-p)\lambda_2)$, which is a maximally polarized pure state in the limit $p \to \{0, 1\}$.

For the sake of completeness, remember that the state of a single qubit can be decomposed on the single-spin operator basis, such that $\rho = \mathbb{1}/2 + \vec{\tau} \cdot \vec{\sigma}$, where $\vec{\sigma} = (\sigma_x, \sigma_y, \sigma_z)$ are the Pauli matrices. The quantum channel $\Phi : \rho \mapsto \rho'$ transforms ρ to $\rho' = \mathbb{1}/2 + \vec{\tau}' \cdot \vec{\sigma}$, where $\vec{\tau}' = t\vec{\tau} + \vec{\kappa}$, $t = O_1 \vec{\eta} O_2$ is a real matrix of size 3 and O_1, O_2 are rotation matrices that specify the orientation of the ellipsoid representing the quantum state. The distortion vector $\vec{\eta}$ converts the Bloch ball to an ellipsoid

$$1/4 = \tau_x^2 + \tau_y^2 + \tau_z^2 = (\tau'_x/\eta_x)^2 + (\tau'_y/\eta_y)^2 + (\tau'_z/\eta_z)^2,$$

while the translation vector $\vec{\kappa}$ moves the centre of mass of the Bloch ball. For the amplitude damping channel, $\vec{\eta} = (\sqrt{1-p}, \sqrt{1-p}, 1-p)$ and $\vec{\kappa} = (0, 0, p)$. Because

$\vec{\kappa} \neq 0$, the amplitude damping channel is not a unital map; a unital map is defined such that the centre of the Bloch ball is a fixed point of the map, i.e., the map transforms the identity state to itself.

Thermodynamics of coherent feedback control

The coherent feedback protocol to extract entropy out of a quantum system with a quantum probe can be understood as a physical implementation of the Maxwell's demon gedanken experiment. The quantum probe plays the role of the demon, which measures the microscopic state of the quantum system and use that information to update the state of the system so as to reduce its entropy. The first controlled-NOT is equivalent to the demon performing a coherent measurement on the quantum system, which correlates the state of the demon with the state of the quantum system (through the creation of two-spin order $2S_zI_z$). The gain in information about the system is quantified by the increase in quantum mutual information. The second controlled-NOT is equivalent to the demon using his knowledge about the state of the quantum system as a resource to perform work on the quantum system and thus reduce its entropy. The projective measurement on the quantum probe dissipates entropy to the environment, is equivalent to erasing the memory of the demon, which contains information about the initial state of the system.

Quantify the amount of entropy extracted

The decrease in entropy of the quantum system after applying the amplitude damping channel is captured by the relative entropy, $S(\rho_B||\rho'_B)$, which quantifies the change in entropy between the initial and final state of the quantum system. For a closed system at quasi-equilibrium, i.e., at equilibrium with respect to its internal Hamiltonian, but not with the larger environment, estimating the decrease in entropy is equivalent to estimating the change in effective temperature of the equilibrium state.

Quantifying the amount of entropy extracted is thus equivalent to the problem of estimating the change in the state parameters of the quantum system. Assuming the quantum system to be a closed system at quasi-equilibrium described by a thermal state $\tau_\beta \propto e^{-\beta\mathcal{H}}$ at a well-defined temperature $T = (\beta k_B)^{-1}$ (k_B is the Boltzmann constant), e.g., the temperature of the lattice, the problem is to estimate the change in inverse temperature $\delta\beta = \beta - \beta'$. The smallest change in effective temperature that can be measured is proportional to the relative entropy $S(\tau_\beta||\tau'_\beta)$ of τ_β with respect to τ'_β, which is a measure of distinguishability between τ_β and τ'_β.

Let's consider a quantum system composed of a spin ensemble initialized in a state of thermal equilibrium with the crystal lattice with inverse spin temperature β_L. The crystal lattice plays the role of a reservoir with infinite heat capacity. In the high temperature limit, the thermal equilibrium state is a weakly ordered state that only slightly differs from the state of complete disorder (mixed state) by $S(\tau_\beta||\mathbb{1}_N) \approx \beta^2\|\mathcal{H}\|^2/N$, with $\|\mathcal{H}\|^2 = \text{Tr}\{\mathcal{H}^2\}$.

By definition, the thermal state maximizes the entropy under the constraint of constant energy, $\text{Tr}\{\tau_\beta\mathcal{H}\} = \langle\mathcal{H}\rangle = \text{cste}$ with $\text{Tr}\{\tau\} = 1$. The equilibrium state for the canonical ensemble is $\tau = e^{-\beta\mathcal{H}} \cdot \mathcal{Z}^{-1}$ with $\mathcal{Z} = \text{Tr}\{e^{-\beta\mathcal{H}}\}$. In the limit of high temperature, $\rho = e^{-\beta\mathcal{H}} \cdot \mathcal{Z}^{-1} \approx (\mathbb{1} - \beta\mathcal{H})/\text{Tr}\{\mathbb{1}\}$, with $\mathcal{Z} = \text{Tr}\{e^{-\beta\mathcal{H}}\} \approx \text{Tr}\{\mathbb{1}\}$. The dimension of the Hilbert space for an ensemble of n spins is given by $N = \text{Tr}\{\mathbb{1}\} = (2I+1)^n$, which is equal to $N = 2^n$ for an ensemble of n spins $I = 1/2$. The mean energy is $\langle\mathcal{H}\rangle = \text{Tr}\{\mathcal{H}\rho\} \approx -\beta\|\mathcal{H}\|^2/N$, where $\|\mathcal{H}\|^2 = \text{Tr}\{\mathcal{H}^2\}$. The heat capacity, defined with respect to a change in inverse temperature β, is $-\partial\langle\mathcal{H}\rangle/\partial\beta = \|\mathcal{H}\|^2/\text{Tr}\{\mathbb{1}\}$.

The von Neumann entropy of τ_β is $S(\tau_\beta)/k_\text{B} = -\text{Tr}\{\tau \log(\tau)\} = \log(\mathcal{Z}) + \beta\langle\mathcal{H}\rangle$, which is equal to $S(\tau_\beta) \approx \log(N) + \beta^2\|\mathcal{H}\|^2/N$ for an ensemble of n non-interacting spins $I = 1/2$. The relative entropy of the thermal equilibrium state τ_β with respect to the maximally mixed state $\mathbb{1}_N$ is thus

$$\begin{aligned} S(\tau_\beta||\mathbb{1}_N) &= \text{Tr}\{\tau_\beta \log\tau\} - \text{Tr}\{\tau_\beta \log \mathbb{1}_N\} && (4.7) \\ &= \log(N) - S(\tau) && (4.8) \\ &\approx \beta^2\|\mathcal{H}\|^2/N, && (4.9) \end{aligned}$$

which approches zero in the limit of infinite temperature, i.e., $S(\tau_\beta||\mathbb{1}_N) \to 0$ for $\beta \to$

0. We have made use of the fact that $S(\tau_\beta) = \log(\mathcal{Z}) + \beta\langle H\rangle \approx \log(N) - \beta^2\|\mathcal{H}\|^2/N$ for $\langle\mathcal{H}\rangle = \mathrm{Tr}\{\tau_\beta\mathcal{H}\} \approx \mathrm{Tr}\{\mathcal{H}\}/N - \beta\mathrm{Tr}\{\mathcal{H}^2\}/N$, where $\mathrm{Tr}\{H\} = 0$ is chosen according to an arbitrary definition of the energy scale. Note that the condition $S(\tau_\beta||\mathbb{1}_N) \ll 1$ guarantees the validity of the the spin temperature assumption, i.e., the density matrix can be approximated by its first order expansion in β. For a two-level system with Zeeman Hamiltonian equal to $\mathcal{H}_S = \hbar\omega_0 \cdot \sigma_z/2$, we have $S(\tau_\beta||\mathbb{1}_N) \approx (\beta\hbar\omega/2)^2$.

4.2.2 Initialize quantum systems using cross-polarization

Electron spins associated with paramagnetic centers in diamond are prepared in a state of low entropy by exchanging energy with the NV electron spin, which is prepared in a pure state using optical pumping (Fig. 4-8). Cross-polarization techniques enable exchanging spin excitations between two spin systems. Cross-polarization in the laboratory frame is achieved by matching the quantization energy of the two spin systems in the laboratory frame by varying the strength and orientation of the static magnetic field. Cross-polarization in the rotating frame is achieved by modulating the energy levels of the two spin systems with continuous driving fields so as to enable the coherent exchange of energy at a level anti-crossing in the tilted doubly-rotating frame. The rate of polarization exchange is maximized at the Hartmann-Hahn matching condition when the amplitude of the continuous driving fields is the same for both spin systems.

Understand cross-polarization in the rotating frame

Cross-polarization in the rotating frame is best understood by considering the Hamiltonian of a quantum system of two spins of different spin species under continuous irradiation with resonant driving fields,

$$\begin{aligned} \mathcal{H} &= \omega_S S_z + \omega_I I_z + d \cdot 2S_z I_z \\ &\quad + 2\Omega_S \cos(\omega_S t) S_x + 2\Omega_I \cos(\omega_I t) I_x, \end{aligned} \tag{4.10}$$

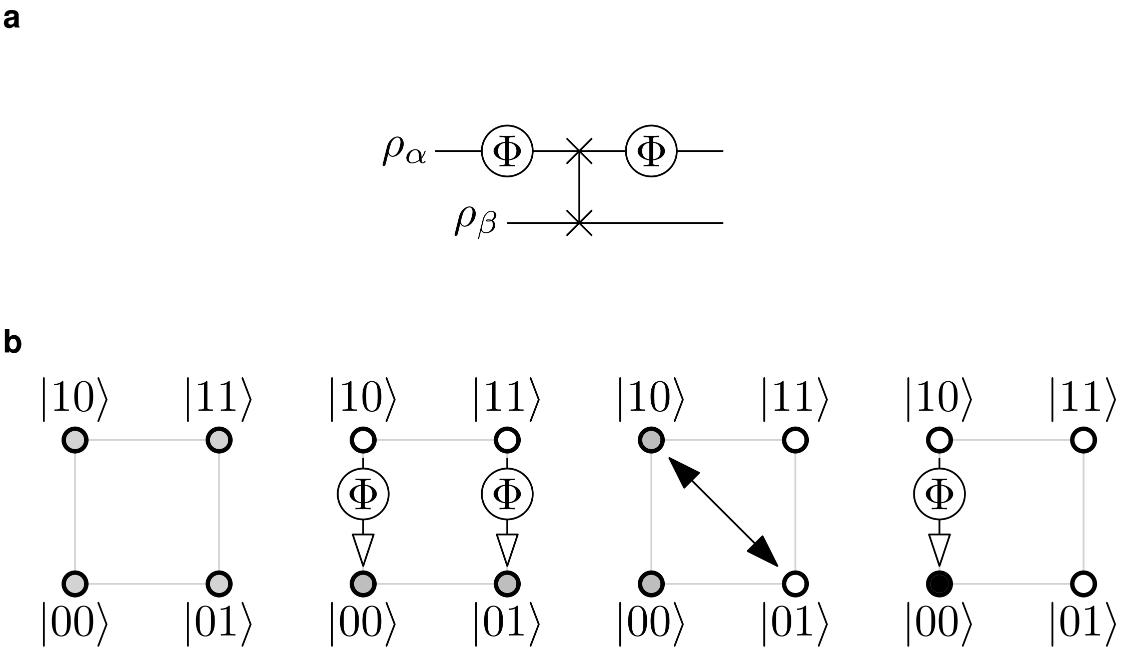

Figure 4-8: **Initialize quantum systems using cross-polarization in the rotating frame. a**, Quantum circuit to initialize a two-qubit system in a pure state when the first qubit possesses an accessible physical mechanism to reduce its entropy, e.g., via optical pumping. The dissipative channel Φ initializes the first qubit in a pure state and the *SWAP* gate, which is represented in the quantum circuit by two multiplication symbols linked by a straingth line, exchanges the state of the first qubit with the state of the second qubit. **b**, The initial state of the two-qubit system is a maximally mixed state with equal occupation probability of all four basis states. A first dissipative channel initializes the state of the first qubit without affecting the state of the second qubit. A *SWAP* gate then exchanges the state of the first qubit with the state of the second qubit, leaving the first qubit in a maximally mixed state and the second qubit in a polarized pure state. A second dissipative channel finally initializes the state of the first qubit and thus prepares the joint state of the two-qubit system into a polarized pure state.

such that the time-independent Hamiltonian in the doubly-rotating frame, $\mathcal{H}_{DR} = U^\dagger \mathcal{H} U - i\partial_t U U^\dagger$ with $U(t) = exp(-i(\omega_S S_z + \omega_I I_z)t)$, after the rotating wave approximation is

$$\mathcal{H}_{DR} = \Omega_S S_x + \Omega_I I_x + d \cdot 2 S_z I_z, \tag{4.11}$$

where the S and I spins are effectively quantized along S_x and I_x with a quantization energy of Ω_S and Ω_I. The dipolar interaction Hamiltonian has been approximated to its secular terms for heteronuclear spins.

To have the S and I spins quantized along S_Z and I_Z in a newly defined tilted frame, we apply the frame transformations $U(\theta_S) = e^{-i\theta_S S_y}$ and $U(\theta_I) = e^{-i\theta_I I_y}$ with $\theta_S = \pi/2$ and $\theta_I = \pi/2$, which transform the spin operators $\{S_z, S_x\}$ to $\{S_Z = S_x, S_X = -S_z\}$ and $\{I_z, I_x\}$ to $\{I_Z = I_x, I_X = -I_z\}$. The Hamiltonian in the tilted doubly-rotating frame $\mathcal{H}_{TDR} = U^\dagger \mathcal{H}_{DR} U$ after the frame transformation $U = U(\theta_S)U(\theta_I)$ is

$$
\begin{aligned}
\mathcal{H}_{TDR} &= \Omega_S S_Z + \Omega_I I_Z + d \cdot 2S_X I_X && (4.12)\\
&= (\Omega_\Sigma S_Z^\Sigma + dS_X^\Sigma) + (\Omega_\Delta S_Z^\Delta + dS_X^\Delta) && (4.13)\\
&= \mathcal{H}_\Sigma + \mathcal{H}_\Delta, && (4.14)
\end{aligned}
$$

where we have expressed the spin operators in the $\{\Sigma, \Delta\}$ basis with $\Omega_\Sigma = (\Omega_S + \Omega_I)$, $\Omega_\Delta = (\Omega_S - \Omega_I)$, $S_Z^\Sigma = (S_Z + I_Z)/2$, $S_Z^\Delta = (S_Z - I_Z)/2$, $S_X^\Delta = (S_X I_X + S_Y I_Y) = (S_+ I_- + S_- I_+)/2$, and $S_X^\Sigma = (S_X I_X - S_Y I_Y) = (S_+ I_+ + S_- I_-)/2$.

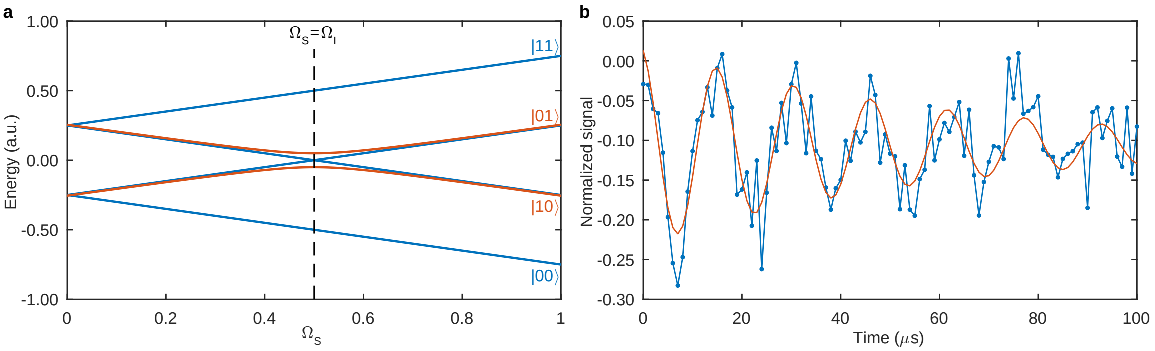

Figure 4-9: **Exchange spin excitations between two quantum systems using cross-polarization in the rotating frame at the Hartmann-Hahn matching condition. a**, Energy levels of a two-spin system under continuous irradiation with resonant driving fields in the tilted doubly-rotating frame. We observe a level anti-crossing in the limit of $\Omega_\Delta \to 0$. **b**, Coherent exchange of spin order between the NV electron spin and the first X electron spin. The solid line is a fit to a sinusoidal function decaying exponentially with a decay of 60.3 μs.

The Hamiltonian for the system of two spins in the titled doubly-rotating frame is decomposed into a sum of two commuting Hamiltonians that reside in the $\{\Sigma, \Delta\}$ subspaces respectively. Each Hamiltonian can be associated with an effective spin-

1/2 with quantization energy Ω_Σ and Ω_Δ coherently driven at a rate specified by the dipolar coupling constant d. For strong driving fields $\Omega_\Sigma \gg d$ in the limit of nearly exact amplitude matching $\Omega_\Delta \lesssim d$, the Hamiltonian in the tilted rotating frame is approximately given by

$$\mathcal{H}_{TDR} \approx (\Omega_\Sigma S_Z^\Sigma) + (\Omega_\Delta S_Z^\Delta + d S_X^\Delta). \tag{4.15}$$

The secular dipolar interaction term is driving coherent Rabi nutations in the Δ subspace spanned by the eigenstates of S_Z^Δ, $\{|10\rangle, |01\rangle\}$, at the rate given by $\tilde{\Omega} = \sqrt{\Omega_\Delta^2 + d^2}$. Figure (4-9) shows the energy levels of Hamiltonian (4.15) and the level anticrossing in the limit of $\Omega_\Delta \to 0$. The fidelity of the spin exchange operation is maximized in the limit of perfect matching from the level anti-crossing, i.e., $\Omega_\Delta = \Omega_S - \Omega_I \to 0$.

In our experiment, we implement the Hartmann-Hahn cross-polarization sequence between the NV electron spin and X electron spin in three steps. First, we prepare the NV electron spin in a coherent superposition of states with a $\pi/2$ pulse along σ_2. Second, we continuously drive on resonance the NV electron spin with a continuous microwave pulse of constant amplitude along σ_1. This step is equivalent to spin locking the NV electron spin along the σ_1 direction. Third, we continuously drive on resonance the X electron spin with a continuous driving field of constant amplitude. The Hartmann-Hahn matching condition is found by sweeping the amplitude of the continuous driving field on the X electron spin and identifying the amplitude at which the relaxation of the NV center is maximal. The driving fields are applied on resonance with the electron spin transitions to avoid measuring a resonance doublet associated with the matching conditions $\Omega_I = \pm\sqrt{\Omega_S^2 + \delta\omega_S^2}$. In our experiment, we drive only one of the two hyperfine transitions of the NV electron spin associated with the N-15 nuclear spin polarized with $p \geq 85\%$ to guarantee perfect matching with the Hartmann-Hahn condition. Driving only one hyperfine transition reduces the visibility of the signal, but does not affect the interpretation of the experimental data.

Initialize electron spins using cross-polarization

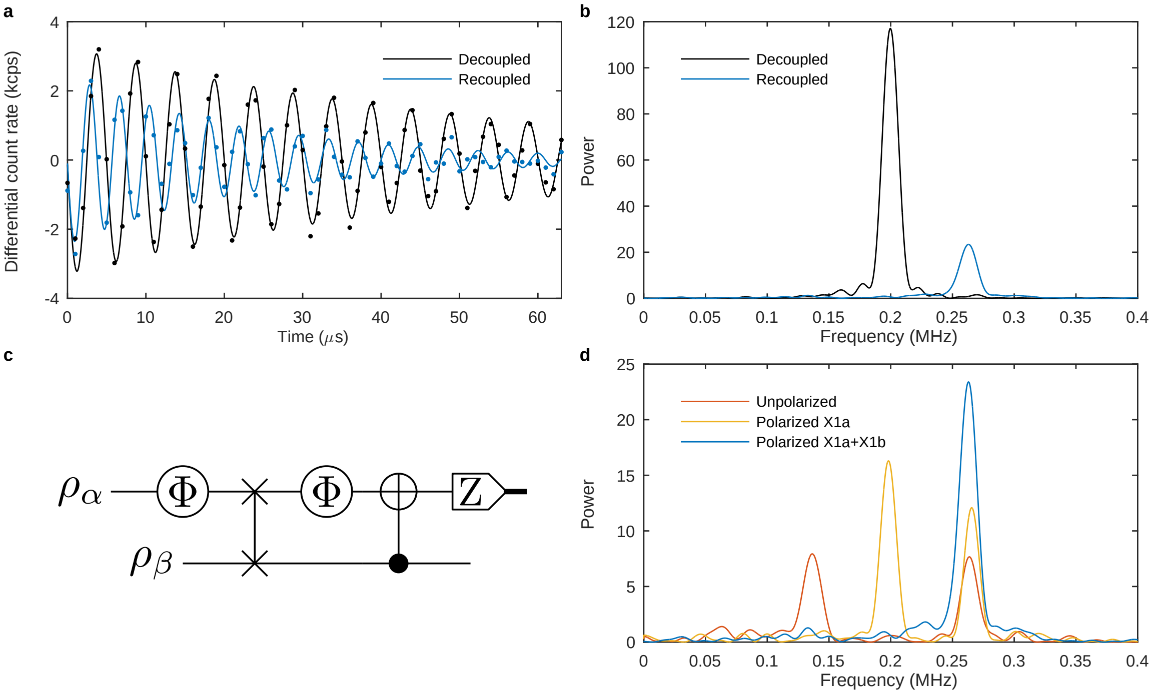

Figure 4-10: **Initialize the first X electron spin in a pure state using cross-polarization in the rotating frame at the Hartmann-Hahn matching condition. a-b,** The spin-echo signal is modulated at 200 kHz. Recoupling the NV electron spin with the first X electron spin polarized up (blue) shifts the spectral line by the dipolar interaction strength $d_1 = 64$ kHz. The decay time decreases from 54.4 μs to 23.9 μs after recoupling to the second polarized X electron spin, indicating a source of unwanted dissipation that should be suppressed **c**, Quantum circuit to initialize and detect the quantum state of a single electron spin. **d**, Spectrum of the recoupled spin-echo signal for the NV electron spin interacting with an unpolarized (red), partially polarized (yellow), or fully polarized (blue) X electron spin (X_1). The partially polarized signal is obtained by tuning the cross-polarization sequence in resonance with only one hyperfine transition of the first X electron spin. The spectral line at 200 kHz corresponds to the leaking coherence terms from the NV electron spin that are created in the absence of recoupling with the X electron spin, e.g., when the X electron spin occupies a hyperfine state that is not resonant with the control pulses. The fully polarized signal is obtained by injecting polarization to the two hyperfine transitions X_{1a} and X_{1b} of the X electron spin.

We implement cross-polarization techniques in the rotating frame to polarize electron spins associated with unknown paramagnetic centers in diamond. The increase in polarization is estimated using quantum parity measurements performed with the SEDOR sequence. The parity observable $\mathcal{O} = S_z \otimes I_z$ measures the imbalance between the population in the Σ and Δ subpsaces spanned by the quantum states $\{|00\rangle, |11\rangle\}$ and $\{|01\rangle, |10\rangle\}$ respectively. We can show that for electron spins with initial polarization $p_\alpha = \alpha$ and $p_\beta = \beta$, the quantum measurement extracts $\langle\mathcal{O}\rangle = p_\alpha p_\beta = \alpha\beta$. Figure 4-10 and Figure 4-11 show that we can efficiently initialize the two X electron spins from maximally mixed thermal states to polarized states using Hartmann-Hahn cross-polarization sequences, as needed to create entangled states of multiple electron spins.

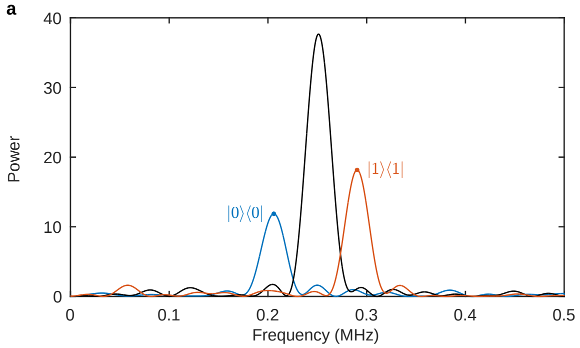

Figure 4-11: **Initialize the second X electron spin in a pure state using cross-polarization in the rotating frame at the Hartmann-Hahn matching condition.** The spin-echo signal is modulated at 200 kHz. Recoupling the NV electron spin with the second X electron spin polarized up (red) or down (blue) shifts the spectral line by the dipolar interaction strength $d_2 = 42$ kHz. The decay time decreases from 52.4 μs to 39.6 μs after recoupling to the second polarized X electron spin.

4.3 Quantum system exploitation

Entanglement is the authentic form of quantum correlations that provide an operational advantage in measuring time-varying fields using quantum probes [20]. Entangled states of light and matter in increasingly large many-body quantum systems have been created for precision measurements of frequency shifts and magnetic resonance imaging. Recent experiments with trapped ions [79] have used entangled states of electron spins to measure the magnetic interaction strength between two electron spins in the presence of magnetic noise with an improvement in sensitivity [80].

This thesis addresses the problem of estimating the amplitude of time-varying magnetic fields with entangled states of electron spins associated with two unknown paramagnetic centers (X_1, X_2) located in the environment of a single nitrogen-vacancy center (NV) in diamond. Each paramagnetic center has an electron spin that is strongly coupled to a nearby nuclear spin ($J = 1/2$). The resonance spectrum of each electron spin exhibits two resolved hyperfine transitions associated with the two possible states of the strongly-coupled nuclear spin. The nuclear spin thus labels the electron spins by shifting their resonance frequencies in such a way that each electron spin can be individually addressed with negligible crosstalk. The magnetic dipolar interaction between the labeled electron spins and other bare electron spins is also suppressed. This section describes our efforts to create entangled states of electron spins between the NV electron spins and the X electron spins to estimate the amplitude of time-varying magnetic fields with improved sensitivity.

4.3.1 Understand entangled states of electron spins

The maximally entangled states for two qubits are the Bell states (modulo an arbitrary phase factor) given by

$$|\Phi_{\pm}\rangle = (|00\rangle \pm |11\rangle)/\sqrt{2} \tag{4.16}$$

$$|\Psi_{\pm}\rangle = (|01\rangle \pm |10\rangle)/\sqrt{2}. \tag{4.17}$$

The projection operators associated with the maximally entangled states, $\pi_\pm^\Phi = |\Phi_\pm\rangle\langle\Phi_\pm|$ and $\pi_\pm^\Psi = |\Psi_\pm\rangle\langle\Psi_\pm|$, are represented in the computational basis as

$$\pi_\pm^\Phi = \frac{1}{2}\cdot\begin{pmatrix} 1 & 0 & 0 & \pm 1 \\ 0 & 0 & 0 & 0 \\ 0 & 0 & 0 & 0 \\ \pm 1 & 0 & 0 & 1 \end{pmatrix}, \; \pi_\pm^\Delta = \frac{1}{2}\cdot\begin{pmatrix} 0 & 0 & 0 & 0 \\ 0 & 1 & \pm 1 & 0 \\ 0 & \pm 1 & 1 & 0 \\ 0 & 0 & 0 & 0 \end{pmatrix} \tag{4.18}$$

The maximally entangled states $|\Phi_\pm\rangle$ and $|\Psi_\pm\rangle$ can be understood as coherent superposition of states in the $\{\Sigma, \Delta\}$ subspaces, which are spanned by the set of energy levels $\{|00\rangle, |11\rangle\}$ and $\{|01\rangle, |10\rangle\}$ and are generated by the Pauli matrices

$$\sigma_0^\Sigma = (\sigma_0 \otimes \sigma_0 + \sigma_3 \otimes \sigma_3)/2 \tag{4.19}$$

$$\sigma_1^\Sigma = (\sigma_1 \otimes \sigma_1 - \sigma_2 \otimes \sigma_2)/2 \tag{4.20}$$

$$\sigma_2^\Sigma = (\sigma_2 \otimes \sigma_1 + \sigma_1 \otimes \sigma_2)/2 \tag{4.21}$$

$$\sigma_3^\Sigma = (\sigma_3 \otimes \sigma_0 + \sigma_0 \otimes \sigma_3)/2, \tag{4.22}$$

and

$$\sigma_0^\Delta = (\sigma_0 \otimes \sigma_0 - \sigma_3 \otimes \sigma_3)/2 \tag{4.23}$$

$$\sigma_1^\Delta = (\sigma_1 \otimes \sigma_1 + \sigma_2 \otimes \sigma_2)/2 \tag{4.24}$$

$$\sigma_2^\Delta = (\sigma_2 \otimes \sigma_1 - \sigma_1 \otimes \sigma_2)/2 \tag{4.25}$$

$$\sigma_3^\Delta = (\sigma_3 \otimes \sigma_0 - \sigma_0 \otimes \sigma_3)/2, \tag{4.26}$$

where the Pauli matrices are given by

$$\sigma_0 = \begin{pmatrix} 1 & 0 \\ 0 & 1 \end{pmatrix}, \; \sigma_1 = \begin{pmatrix} 0 & 1 \\ 1 & 0 \end{pmatrix}, \; \sigma_2 = \begin{pmatrix} 0 & -i \\ i & 0 \end{pmatrix}, \; \sigma_3 = \begin{pmatrix} 1 & 0 \\ 0 & -1 \end{pmatrix}. \tag{4.27}$$

These Pauli matrices satisfy the usual commutation relationships, e.g., $\sigma_3^\Sigma =$

$-i[\sigma_1^\Sigma, \sigma_2^\Sigma]/2$, and are explicitely written as

$$\sigma_0^\Sigma = \begin{pmatrix} 1 & 0 & 0 & 0 \\ 0 & 0 & 0 & 0 \\ 0 & 0 & 0 & 0 \\ 0 & 0 & 0 & 1 \end{pmatrix}, \ \sigma_1^\Sigma = \begin{pmatrix} 0 & 0 & 0 & 1 \\ 0 & 0 & 0 & 0 \\ 0 & 0 & 0 & 0 \\ 1 & 0 & 0 & 0 \end{pmatrix}, \ \sigma_2^\Sigma = \begin{pmatrix} 0 & 0 & 0 & -i \\ 0 & 0 & 0 & 0 \\ 0 & 0 & 0 & 0 \\ i & 0 & 0 & 0 \end{pmatrix}, \ \sigma_3^\Sigma = \begin{pmatrix} 1 & 0 & 0 & 0 \\ 0 & 0 & 0 & 0 \\ 0 & 0 & 0 & 0 \\ 0 & 0 & 0 & -1 \end{pmatrix}$$

and

$$\sigma_0^\Delta = \begin{pmatrix} 0 & 0 & 0 & 0 \\ 0 & 1 & 0 & 0 \\ 0 & 0 & 1 & 0 \\ 0 & 0 & 0 & 0 \end{pmatrix}, \ \sigma_1^\Delta = \begin{pmatrix} 0 & 0 & 0 & 0 \\ 0 & 0 & 1 & 0 \\ 0 & 1 & 0 & 0 \\ 0 & 0 & 0 & 0 \end{pmatrix}, \ \sigma_2^\Delta = \begin{pmatrix} 0 & 0 & 0 & 0 \\ 0 & 0 & -i & 0 \\ 0 & i & 0 & 0 \\ 0 & 0 & 0 & 0 \end{pmatrix}, \ \sigma_3^\Delta = \begin{pmatrix} 0 & 0 & 0 & 0 \\ 0 & 1 & 0 & 0 \\ 0 & 0 & -1 & 0 \\ 0 & 0 & 0 & 0 \end{pmatrix}.$$

The joint state of two partially polarized qubits can be expressed as a statistical mixture of partially polarized qubits in the $\{\Sigma, \Delta\}$ subspaces,

$$\begin{aligned}
\rho_{\alpha\beta} &= \rho_\alpha \otimes \rho_\beta && (4.28)\\
&= \frac{(\sigma_0 + \alpha \cdot \sigma_3)}{2} \otimes \frac{(\sigma_0 + \beta \cdot \sigma_3)}{2} && (4.29)\\
&= (\frac{(\sigma_0\sigma_0 + \alpha\beta \cdot \sigma_3\sigma_3)}{2} + \frac{(\alpha \cdot \sigma_3\sigma_0 + \beta \cdot \sigma_0\sigma_3)}{2})/2 && (4.30)\\
&= \frac{(1+\alpha\beta)}{2} \cdot \frac{\sigma_0^\Sigma}{2} + \frac{(1-\alpha\beta)}{2} \cdot \frac{\sigma_0^\Delta}{2} + \frac{(\alpha+\beta)}{2} \cdot \frac{\sigma_3^\Sigma}{2} + \frac{(\alpha-\beta)}{2} \cdot \frac{\sigma_3^\Delta}{2} && (4.31)\\
&= p_\Sigma \cdot (\sigma_0^\Sigma + \alpha_\Sigma \cdot \sigma_3^\Sigma)/2 + p_\Delta \cdot (\sigma_0^\Delta + \alpha_\Delta \cdot \sigma_3^\Delta)/2 && (4.32)\\
&= p_\Sigma \cdot \rho_{\alpha\beta}^\Sigma + p_\Delta \cdot \rho_{\alpha\beta}^\Delta, && (4.33)
\end{aligned}$$

where the population and the polarization of the joint state in the $\{\Sigma, \Delta\}$ subspaces is

$$\begin{aligned}
p_\Sigma &= (1+\alpha\beta)/2 && (4.34)\\
p_\Delta &= (1-\alpha\beta)/2 && (4.35)
\end{aligned}$$

and

$$\alpha_\Sigma = \frac{(\alpha+\beta)}{(1+\alpha\beta)} \tag{4.36}$$

$$\alpha_\Delta = \frac{(\alpha-\beta)}{(1-\alpha\beta)}. \tag{4.37}$$

The occupation probability (population) in the $\{\Sigma, \Delta\}$ subpaces is determined by the even/odd parity ($\alpha\beta$) of the initial state of the two qubits, whereas the polarization in the $\{\Sigma, \Delta\}$ subpaces is determined by the occupation probability of the ground and excited states, $|00\rangle$ vs. $|11\rangle$ for the Σ subspace, and $|01\rangle$ vs. $|10\rangle$ for the Δ subspace.

In theory, an entangled state of two qubits can be created by applying one of many possible entangling gates, e.g., by applying an entangling gate that implements the equivalent of a $\pi/2$ pulse along $\sigma_2^\Sigma + \sigma_2^\Delta$, such that

$$\rho'_{\alpha\beta} = p_\Sigma \cdot (\sigma_0^\Sigma + \alpha_\Sigma \cdot \sigma_1^\Sigma)/2 + p_\Delta \cdot (\sigma_0^\Delta + \alpha_\Delta \cdot \sigma_1^\Delta)/2. \tag{4.38}$$

In the limit of maximally polarized qubits with $|\alpha| \to 1$ and $|\beta| \to 1$, the entangling gate creates a maximally entangled states

$$\rho'_{\alpha\beta} \in \{\pi_\pm^\Phi = (\sigma_0^\Sigma \pm \sigma_1^\Sigma)/2, \pi_\pm^\Psi = (\sigma_0^\Delta \pm \sigma_1^\Delta)/2\}. \tag{4.39}$$

Understand the formalism of spin operators

The formalism of spin operators facilitates understanding the experimental implementation of entangling gates. The state of a quantum system is described by the density operator $\hat{\rho}$, which can be expressed as a density matrix

$$\rho = \sum_{kl} \lambda_{kl} |k\rangle\langle l|, \tag{4.40}$$

where λ_{kl} are the matrix elements of the density matrix expressed in the basis generated by the set of quantum states $\{|k\rangle\}$. The diagonal elements λ_{kk} quantify the population in the state $|k\rangle$, whereas the non-diagonal elements λ_{kl} quantify the coherence between the states $|k\rangle$ and $|l\rangle$.

The density operator can be written as a linear combination of spin operators,

$$\hat{\rho} = \sum_k \lambda_k S_k, \tag{4.41}$$

which generate a complete set of orthogonal basis operators $\{S_k\}$ in the Liouville space. The spin operators satisfy the commutation relations $[S_k, S_l] = i\epsilon_{klm}S_m$, where ϵ_{klm} is the Levi-Civita symbol with $\epsilon_{xyz} = 1$ for the three Cartesian dimensions $\{x, y, z\}$. The spin operators for a spin-1/2 can be expressed in terms of the Pauli matrices, $\{\mathbb{1}, S_x, S_y, S_z\} = \{\sigma_0, \sigma_1/2, \sigma_2/2, \sigma_3/2\}$.

The spin operators provide a simple way to calculate the unitary evolution of a quantum system,

$$U\rho U^\dagger = \sum_k \lambda_k U S_k U^\dagger, \tag{4.42}$$

by calculating the evolution of each spin operator S_k. Given the unitary operator $U(\theta, S_l) = e^{-i\theta S_l}$, the Baker-Hausdorff formula applied to spin operators gives

$$U(\theta, S_l) : S_k \mapsto S_k \cos\theta - i[S_l, S_k]\sin\theta \tag{4.43}$$

for S_l different than S_k. For example, the unitary operation $U(\pi/2, S_y)$ is transformed to the spin operator S_z to $S_x = -i[S_z, S_y]$, such that the polarized state $\rho = \mathbb{1}/2 + S_z = |0\rangle\langle 0|$ transforms to the coherent state $\rho' = \mathbb{1}/2 + S_x = |+\rangle\langle +|$, as expected for a spin-1/2 rotated by $\pi/2|_y$ microwave pulse.

The set of basis operators for a quantum system composed of multiple subsystems is generated by taking the direct product between the spin operators for each subsystem. The set of spin operators for a system of two qubits $S = 1/2$ and $I = 1/2$ are

$$\begin{aligned}
&\{\mathbb{1}, S_x, S_y, S_z\} \otimes \{\mathbb{1}, I_x, I_y, I_z\} \\
&\{\mathbb{1}, S_x, S_y, S_z, I_x, I_y, I_z, \\
&\;2S_xI_x, 2S_xI_y, 2S_xI_z, 2S_yI_x, 2S_yI_y, 2S_yI_z, 2S_zI_x, 2S_zI_y, 2S_zI_z\},
\end{aligned} \tag{4.44}$$

where the prefactor 2 is added to the two-spin operators to satisfy the commutation relations.

Create entangled states of electron spins

A bipartite entangled state of two electron spin qubits initialized in a polarized state $\rho_{\alpha\beta} = \rho_\alpha \otimes \rho_\beta$ is created by preparing the first qubit in a superposition of states with a Hadamard gate and correlating the state of the first and second qubits with a $\mathrm{C}_\alpha\mathrm{NOT}_\beta$ gate. We experimentally implement this entangling gate with spin qubits associated with electron spins by preparing the first qubit in a superposition of state with a $\pi/2$ along σ_y ($U(\pi/2, S_y)$), and correlating the two spins with an INEPT sequence, which consist in preparing the second qubit in a superposition of states with a $\pi/2$ pulse along σ_y ($U(\pi/2, I_y)$), evolving the joint state under the secular dipolar interaction $\mathcal{H} = d \cdot 2S_zI_z$ for a duration $t = \pi/(2d)$, such that $\theta = d \cdot t = \pi/2$ ($U(\pi/2, 2S_zI_z)$), and combining the coherence terms with a final $\pi/2$ pulse along σ_x on the second qubit ($U(\pi/2, I_x)$).

Given the initial state of the quantum system of two qubits,

$$\begin{aligned} \rho_{\alpha\beta} &= \rho_\alpha \otimes \rho_\beta & (4.45) \\ &= (\mathbb{1}/2 + \alpha S_z) \otimes (\mathbb{1}/2 + \beta I_z), & (4.46) \end{aligned}$$

where $p_\alpha = \langle S_z \rangle = \mathrm{Tr}\{\rho_\alpha S_z\}/\mathrm{Tr}\{S_zS_z\} = \alpha$ and $p_\beta = \beta$ are the initial polarizations of the first and second qubits, the series of $\pi/2|_y$ pulses acting on both qubits ($U(\pi/2, S_y + I_y)$) creates a coherent superposition of states on each qubits,

$$\begin{aligned} \rho_{\alpha\beta} &= (\mathbb{1}/2 + \alpha S_z) \otimes (\mathbb{1}/2 + \beta I_z) & (4.47) \\ &\mapsto (\mathbb{1}/2 + \alpha S_x) \otimes (\mathbb{1}/2 + \beta I_x) & (4.48) \\ \rho'_{\alpha\beta} &= (\mathbb{1}/4 + \alpha/2 \cdot S_x + \beta/2 \cdot I_x + \alpha\beta/2 \cdot 2S_xI_x). & (4.49) \end{aligned}$$

The evolution under the secular dipolar interaction term, $\mathcal{H} = d \cdot 2S_zI_z$ transforms the spin operators to

$$
\begin{aligned}
S_x &\mapsto S_x \cos\theta + 2S_yI_z \sin\theta && (4.50)\\
I_x &\mapsto S_x \cos\theta + 2S_zI_y \sin\theta && (4.51)\\
2S_xI_x &\mapsto 2S_xI_x, && (4.52)
\end{aligned}
$$

where $\theta = d \cdot t$. We have used the Baker-Hausdorff formula for spin operators (Eq. (4.43)) with $[2S_zI_z, S_x] = i2S_yI_z$ and $[2S_zI_z, 2S_xI_x] = 0$. Choosing the evolution time $t = \pi/(2d)$ such that $\theta = \pi/2$, the state of the joint system obtained after the evolution period under the dipolar interaction term and the $\pi/2|_x$ pulse on the second qubit $(U(\pi/2, I_x))$ is

$$
\begin{aligned}
\rho'_{\alpha\beta} &= (\mathbb{1}/4 + \alpha/2 \cdot S_x + \beta/2 \cdot I_x + \alpha\beta/2 \cdot 2S_xI_x) && (4.53)\\
&\mapsto (\mathbb{1}/4 + \alpha/2 \cdot 2S_yI_z + \beta/2 \cdot 2S_zI_y + \alpha\beta/2 \cdot 2S_xI_x) && (4.54)\\
&\mapsto (\mathbb{1}/4 - \alpha/2 \cdot 2S_yI_y + \beta/2 \cdot 2S_zI_z + \alpha\beta/2 \cdot 2S_xI_x). && (4.55)
\end{aligned}
$$

The entangled nature of this state is better seen by transforming the spin operators to the $\{\Sigma, \Delta\}$ subspaces spanned by the maximally entangled states. The spin operators are grouped, such that

$$
\begin{aligned}
\rho''_{\alpha\beta} &= \mathbb{1}/4 - \alpha/2 \cdot 2S_yI_y + \beta/2 \cdot 2S_zI_z + \alpha\beta/2 \cdot 2S_xI_x && (4.56)\\
&= (\mathbb{1}/2 + \beta \cdot 2S_zI_z)/2 - \alpha \cdot (2S_yI_y - \beta \cdot 2S_xI_x)/2 && (4.57)\\
&= (1+\beta)/2 \cdot (\mathbb{1}^\Sigma/2 + \alpha S_x^\Sigma) + (1-\beta)/2 \cdot (\mathbb{1}^\Delta/2 - \alpha S_x^\Delta) && (4.58)\\
&= p_\Sigma \cdot \rho_\Phi + p_\Delta \cdot \rho_\Psi, && (4.59)
\end{aligned}
$$

where the identity operators are defined as

$$
\begin{aligned}
\mathbb{1} &= \mathbb{1}^\Sigma + \mathbb{1}^\Delta && (4.60)\\
\mathbb{1}^\Sigma/2 &= (\mathbb{1}/2 + 2S_zI_z)/2 && (4.61)\\
\mathbb{1}^\Delta/2 &= (\mathbb{1}/2 - 2S_zI_z)/2, && (4.62)
\end{aligned}
$$

and the spin operators in the $\{\Sigma, \Delta\}$ subspaces are defined as

$$\begin{aligned} S_x^{\Sigma} &= (2S_xI_x - 2S_yI_y)/2 = \sigma_1^{\Sigma}/2 && (4.63) \\ S_x^{\Delta} &= (2S_xI_x + 2S_yI_y)/2 = \sigma_1^{\Delta}/2. && (4.64) \end{aligned}$$

The initial polarization of the second qubit determines the occupation probability in each subspace

$$\begin{aligned} p_{\Sigma} &= (1+\beta)/2 && (4.65) \\ p_{\Delta} &= (1-\beta)/2, && (4.66) \end{aligned}$$

whereas the initial polarization of the first qubit $p_\alpha = \alpha$ determines the polarization of the entangled state in each subpsace. This experimental implementation of the entangling differs from what had been derived in Eq. (4.38) by applying a $\pi/2$ pulse along $\sigma_2^{\Sigma} + \sigma_2^{\Delta}$.

Understand entangling gates

Let's consider the joint state of a quantum system of two qubits prepared in partially polarized states, $\rho_{\alpha\beta} = \rho_\alpha \otimes \rho_\beta$, with $\rho_\alpha = (\sigma_0 + \alpha\sigma_3)/2$ and $\rho_\alpha = (\sigma_0 + \beta\sigma_3)/2$. The joint state is diagonal in the computational basis spanned by the basis states $\{|m\rangle\} = \{|00\rangle, |01\rangle, |10\rangle, |11\rangle\}$, where $m = (m_1m_2)_2$ is the binary number indexing the states of the quantum system. The entangling gate maps the joint state $\rho = \sum_m p_m \pi_m$ to $\rho' = \sum_m p_m \pi'_m$, where ρ' is expressed as a linear combination of the projection operators on the Bell states

$$\begin{aligned} \pi_{\Psi}^{\pm} &= |\Psi_{\pm}\rangle\langle\Psi_{\pm}| && (4.67) \\ \pi_{\Phi}^{\pm} &= |\Phi_{\pm}\rangle\langle\Phi_{\pm}|, && (4.68) \end{aligned}$$

with occupation probabilities given by $\{p_m\} = \{p_\alpha^0 p_\beta^0, p_\alpha^0 p_\beta^1, p_\alpha^1 p_\beta^0, p_\alpha^1 p_\beta^1\}$ with $\{p_\alpha^0, p_\alpha^1\} = \{(1+\alpha)/2, (1-\alpha)/2\}$ and $\{p_\beta^0, p_\beta^1\} = \{(1+\beta)/2, (1-\beta)/2\}$. The entangling gate transforms the projection operators on the computational basis states $\{\pi_m\} = \{\pi_{00}, \pi_{01}, \pi_{10}, \pi_{11}\}$ into the projection operators on the Bell states $\{\pi'_m\} = \{\pi_\Phi^+, \pi_\Psi^+, \pi_\Phi^-, \pi_\Psi^-\}$, as shown in the transformation table

		ρ_β	
		π_0	π_1
ρ_α	π_0	π_Φ^+	π_Ψ^+
	π_1	π_Φ^-	π_Ψ^-

Maximally entangled states are obtained for pure initial states with $|\alpha| = 1$ and $|\beta| = 1$. In such a case, the initial state of the control qubit (ρ_α) determines the parity of the entangled state ($\{+, -\}$), whereas the initial state of the target qubit (ρ_β) determines the phase of the entangled state ($\{\Phi, \Psi\}$).

The projection operators $\{\pi_\Phi^+, \pi_\Phi^-, \pi_\Psi^+, \pi_\Psi^-\}$ can be transformed to the Pauli matrices in the $\{\Sigma, \Delta\}$ subspaces $\{\sigma_0^\Sigma, \sigma_1^\Sigma, \sigma_0^\Delta, \sigma_1^\Delta\}$ with $\{\pi_+^\Sigma, \pi_-^\Sigma\} = \{(\sigma_0^\Sigma + \sigma_1^\Sigma)/2, (\sigma_0^\Sigma - \sigma_1^\Sigma)/2)\}$ and $\{\pi_+^\Delta, \pi_-^\Delta\} = \{(\sigma_0^\Delta + \sigma_1^\Delta)/2, (\sigma_0^\Delta - \sigma_1^\Delta)/2\}$, such that the entangled state

$$\begin{aligned} \rho &= (p_+^\Sigma \pi_+^\Sigma + p_-^\Sigma \pi_-^\Sigma) + (p_+^\Delta \pi_+^\Delta + p_-^\Delta \pi_-^\Delta) && (4.69) \\ &= p_\Sigma(\sigma_0^\Sigma + \alpha_\Sigma \sigma_1^\Sigma) + p_\Delta(\sigma_0^\Delta + \alpha_\Delta \sigma_x^\Delta) && (4.70) \end{aligned}$$

can be understood as a coherent superposition of states in the $\{\Sigma, \Delta\}$ manifolds with $p_\Sigma = p_+^\Sigma + p_-^\Sigma$, $p_\Delta = p_+^\Delta + p_-^\Delta$, $\alpha_\Sigma = (p_+^\Sigma - p_-^\Sigma)/(p_+^\Sigma + p_-^\Sigma)$, and $\alpha_\Delta = (p_+^\Delta - p_-^\Delta)/(p_+^\Delta + p_-^\Delta)$.

4.3.2 Create and detect entangled states of two electron spins

We create bipartite entangled states of two electron spins between the NV electron spin and the first X electron spin (Fig. 4-12). After initializing the state of the NV electron spin by optical pumping, the two hyperfine transitions of the X electron spins are polarized with a series of two Hartmann-Hahn cross-polarization sequences. After initializing the two electron spins, bipartite entangled states are created by applying an entangling gate, which consists in a Hadamard gate on the first qubit to create a coherent superposition of states on the NV electron spin and a $\mathrm{C}_\alpha\mathrm{NOT}_\beta$ to transfer the single-spin coherence into two-spin coherence. These gates are implemented using a series of control pulses and periods of evolution under the dipolar interaction, vid., INEPT sequence.

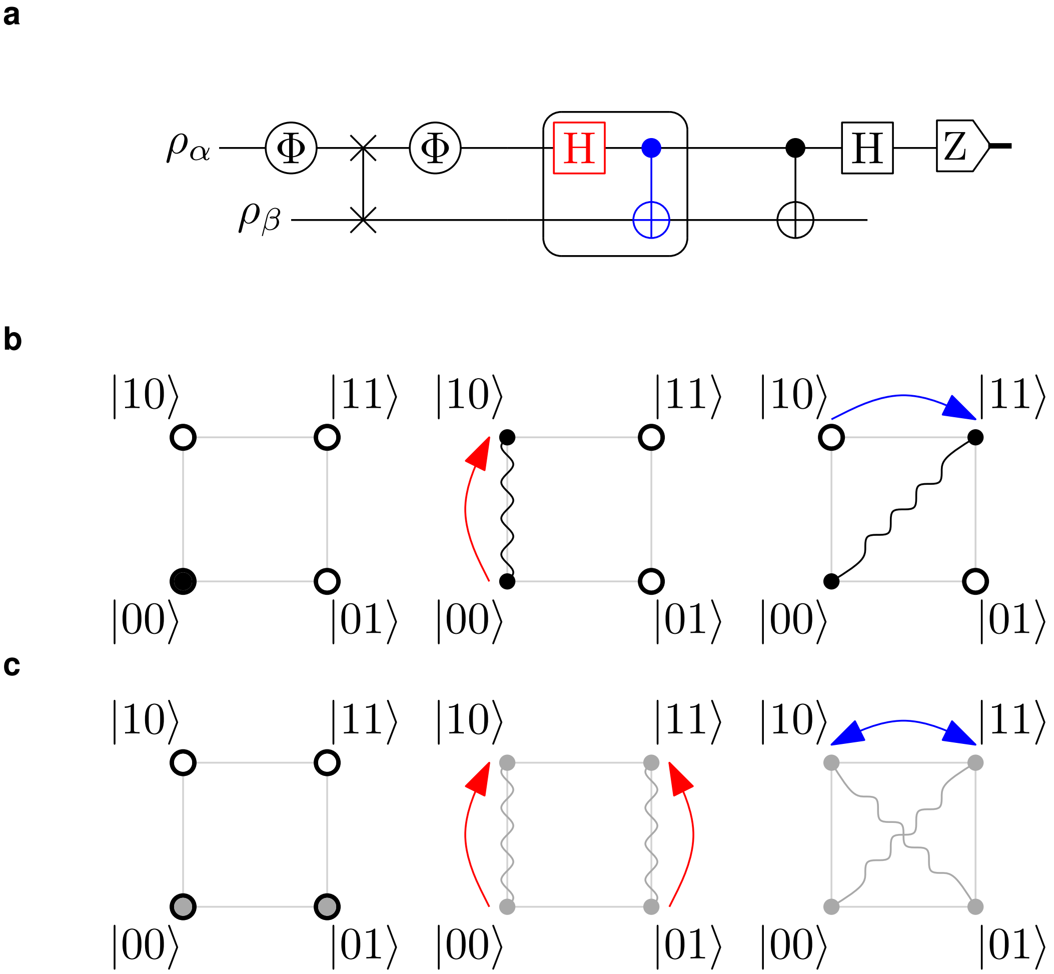

Figure 4-12: **Create entangled states of two electron spins in diamond. a**, Quantum circuit to create entangled states of two electron spins with the entangling gate enclosed in a black box. **b**, The population of the two-qubit polarized state is first converted into single-spin coherence on the NV electron spin with a Hadamard gate and then transferred into two-spin (double quantum) coherence with a controlled-not gate. Applying the entangling gate starting from the polarized state $|00\rangle$ creates the Bell state $\Phi = (|00\rangle + |11\rangle)/\sqrt{2}$. **c**, Applying the entangling gate to the X electron spin prepared in a mixed state creates a quantum state corresponding to a statistical mixture of zero-quantum ($|\Psi\rangle\langle\Psi|$) and double-quantum ($|\Phi\rangle\langle\Phi|$) coherences.

We confirm the creation of entangled states of two electron spins by performing state tomography in the subspace of the Hilbert space spanned by the two-qubit Bell states. The phases of the microwave pulses implementing the disentangling gate are modulated at $\nu_\alpha = 500$ kHz and $\nu_\beta = 300$ kHz to simulate the evolution of the entangled state under the Zeeman Hamiltonian $\mathcal{H}/h = \nu_\alpha S_z + \nu_\beta I_z$, where α and β denotes the electron spins of the NV center and paramagnetic center respectively. The occupation probability of the entangled state in the subspaces associated with the Bell states $|\Phi\rangle$ and $|\Psi\rangle$ is captured by spectral components at $\nu_\Sigma = \nu_\alpha + \nu_\beta = 800$ kHz and $\nu_\Delta = \nu_\alpha - \nu_\beta = 300$ kHz. Figure 4-13 shows that we can efficiently create and detect bipartite entangled states of electron spins after initializing the state of the X electron spin in a pure state.

Imperfect recoupling to the X electron spin, e.g., when driving only one of the two possible hyperfine transitions, creates single-spin coherence terms on the NV electron spin that modulates the fluorescence signal at ν_α. These coherence terms are eliminated by averaging over two symmetric realizations of the experiment obtained with and without shifting by π the phase of all of the pulses implementing the disentangling gate [81]. This phase cycling technique is commonly used in quantum sensing protocols to cancel out common mode noise and nuclear magnetic resonance to isolate spectral components associated with specific coherence terms in the many-body Hamiltonian.

4.3.3 Create and detect entangled states of three electron spins

We create entangled states of three electron spins associated with a single nitrogen-vacancy center (NV) and two paramagnetic centers (Fig. 4-14). The quantum system of three electron is prepared in a pure state with a series of optical pulses acting on the NV center and cross-polarization sequences acting on both the NV electron spin and X electron spins. Specifically, we transfer polarization from the NV electron spin to the X electron spins with a series of four Hartmann-Hahn cross-polarization sequences resonantly driving each one of the four hyperfine transitions of the two paramagnetic centers.

We create the entangled state $|GHZ\rangle = (|000\rangle + |111\rangle)/\sqrt{2}$ with an entangling operation composed of a Hadamard gate and two controlled-not gates. The entangling gate consists in a Hadamard gate applied on the first qubit and two controlled-not

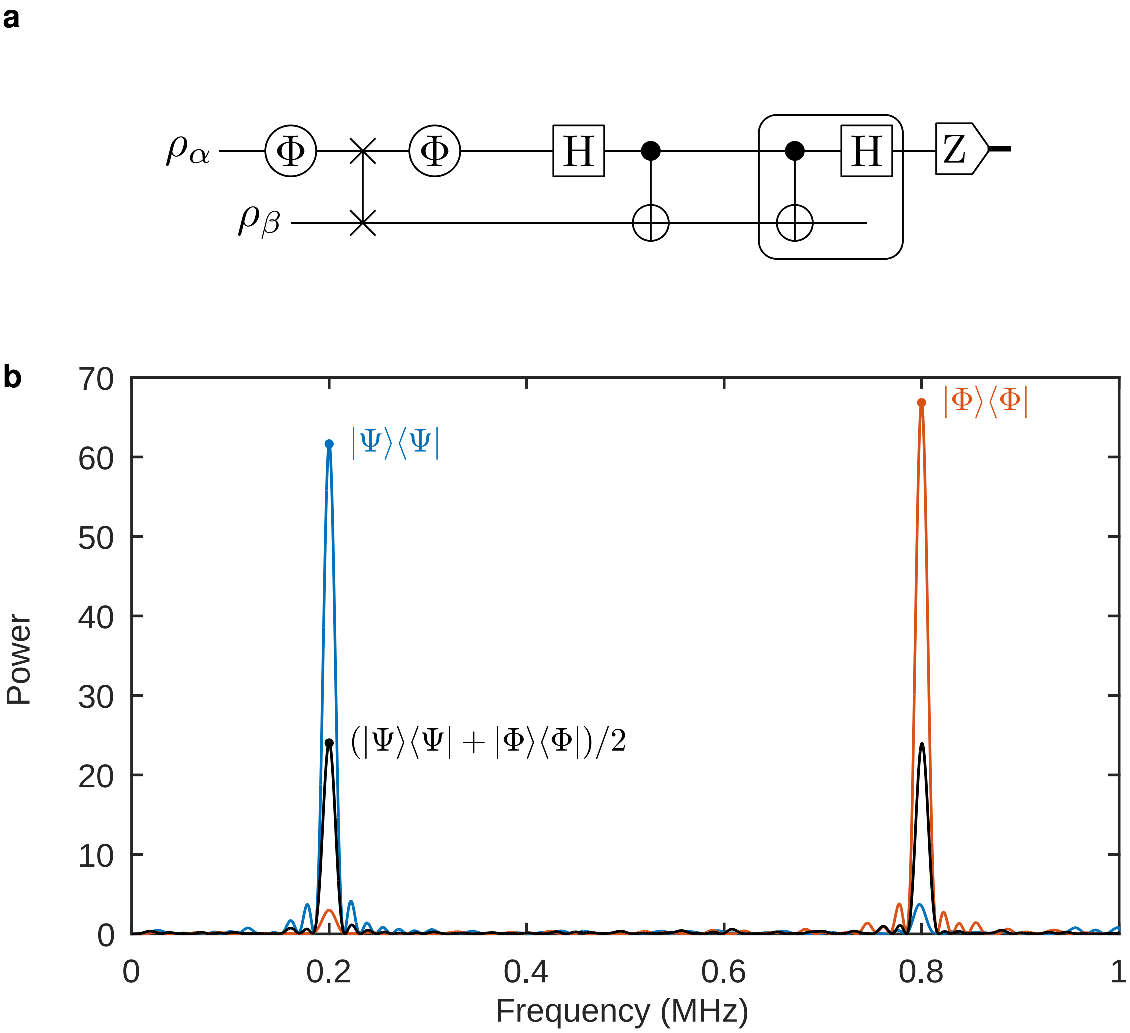

Figure 4-13: **Detect entangled states of two electron spins in diamond.** **a**, Quantum circuit with the disentangling gate enclosed in a black box. **b**, Applying an entangling gate to an unpolarized spin (black) creates a statistical mixture of maximally mixed states $\rho_{\alpha\beta} = (\rho_\Psi + \rho_\Phi)/2$. Applying an entangling gate after polarizing the electron spin in the state $|0\rangle$ or $|1\rangle$ creates the bipartite entangled states $|\Phi\rangle = (|00\rangle + |11\rangle)/\sqrt{2}$ or $|\Psi\rangle = (|01\rangle + |10\rangle)/\sqrt{2}$. The phases of the pulses driving the disentangling gate are modulated at $\nu_{NV} = 500$ kHz, $\nu_X = 300$ kHz, so that the bipartite entangled states $|\Psi\rangle = (|01\rangle+|10\rangle)/\sqrt{2}$ and $|\Phi\rangle = (|00\rangle+|11\rangle)/\sqrt{2}$ oscillates at $\nu_\Delta = 200$ kHz and $\nu_\Sigma = 800$ kHz.

gates applied on the first and second qubits and the first and third qubits. The Hadamard gate prepares the NV electron spin into a coherent superposition of states; then, the first $\mathrm{C}_{NV}\mathrm{NOT}_{X_1}$ gate converts the single-spin coherence on the NV electron spin into two-spin coherence in the double-quantum subspace; finally, the second $\mathrm{C}_{NV}\mathrm{NOT}_{X_2}$ gate converts the two-spin coherence in the double-quantum subspace

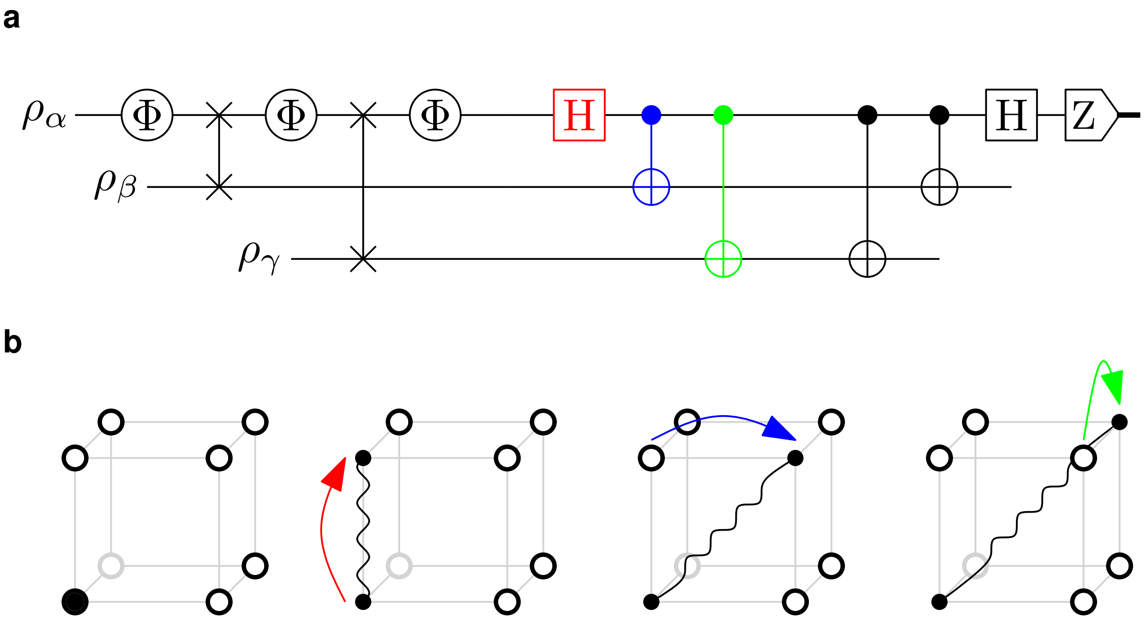

Figure 4-14: **Create and detect entangled states of three electron spins in diamond.** **a**, Quantum circuit to create and detect entangled states of three electron spins. **b**, The population of the three-qubit polarized state is first converted into single-spin coherence on the NV electron spin with a Hadamard gate and then transferred into three-spin coherence with a series of two controlled-not gates to create the tripartite entangled state $|\mathrm{GHZ}\rangle = (|000\rangle + |111\rangle)/2$.

into three-spin coherence in the triple-quantum subspace.

We detect the tripartite entangled state by converting the three-spin coherence back into a population state on the three qubits and performing a projective measurement on the NV electron spin. Figure 4-15 shows the creation of a tripartite entangled state of three electrons. The signal is modulated at $\nu_\Sigma = \nu_\alpha + \nu_\beta + \nu_\gamma = 800$ kHz for the $|\mathrm{GHZ}\rangle$ state when the phases of the pulses of the distentangling gate are modulated at $\nu_\alpha = 500$ kHz, $\nu_\beta = 200$ kHz, and $\nu_\gamma = 100$ kHz.

4.3.4 Measure magnetic fields with entangled states of electron spins

We estimate the amplitude of a sinusoidal waveform oscillating at 100 kHz with entangled states of two electron spins. The entangled state is decoupled from external sources of noise by simultaneously applying two decoupling π pulses on both the NV

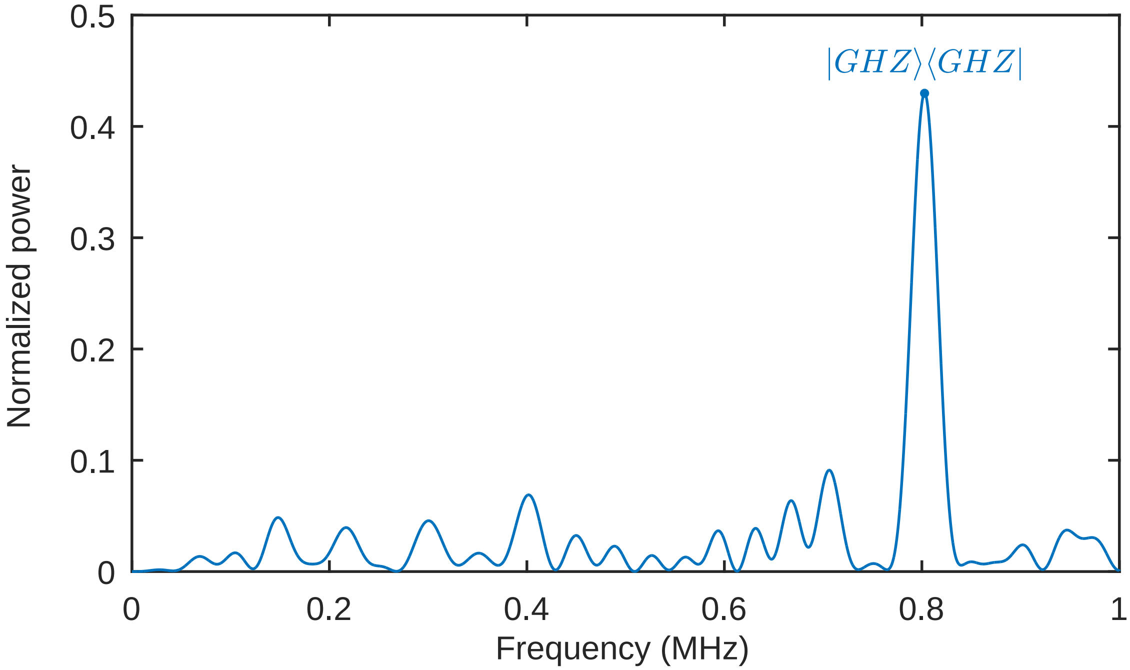

Figure 4-15: **Create and detect entangled states of three electron spins in diamond.** Normalized spectrum of the tomography signal after applying an entangling operation between the NV electron spin and two X electron spins. The phase of the readout pulses for the disentangling operation is modulated at $\nu_\alpha = 0.5$ MHz, $\nu_\beta = 0.2$ MHz, and $\nu_\gamma = 100$ kHz for the NV electron spin and the two X electron spins respectively. The coherent modulation at $\nu_\Sigma = \nu_\alpha + \nu_\beta + \nu_\gamma = 800$ kHz indicates the creation of the tripartite entangled state $|GHZ\rangle = (|000\rangle + |111\rangle)/\sqrt{2}$.

electron spin and the first X electron spin during the sensing period. The relative delay between the sinusoidal waveform and the sampling sequence is calibrated so as to maximize the phase acquired by the entangled state of two electron spins.

After initializing the state of the NV electron spin and the first X electron spin with a cross-polarization sequence, we create the entangled state $\Phi = (|00\rangle + |11\rangle)/\sqrt{2}$, let it interact with the sinusoidal waveform for a single period $T = 1/\nu = 10$ μs, and convert the acquired phase $\phi_\Sigma = \phi_\alpha + \phi_\beta$ into a measurable population difference onto the NV electron spin. The signal measured for a coherent superposition of state on the NV electron spin and an entangled state of the NV electron and X electron spin is shown in Fig 4-16.

The interferometric signal for the bipartite entangled state precesses at twice the rate as the coherent state, but its visibility is about thrice as small. The decrease in

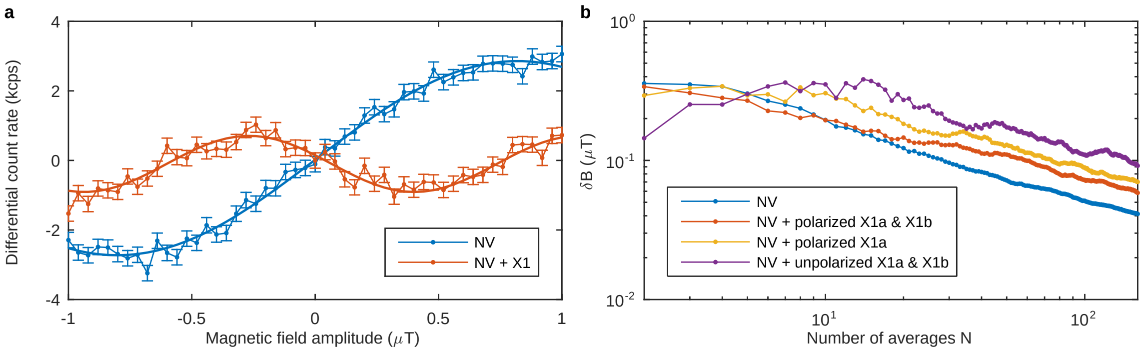

Figure 4-16: **Measure magnetic fields with entangled states of two electron spins in diamond. a,** Differential fluorescence signal as a function of the amplitude of a sinusoidal field oscillating at 100 kHz. The bipartite entangled state $|\Phi\rangle = (|00\rangle + |11\rangle)/\sqrt{2}$ oscillates at twice the rate than the coherent superposition of states $(|0\rangle + |1\rangle)/\sqrt{2}$. **b,** The decrease in the smallest field as a function of the number of repetitions shows that the coherent superposition of states of the single NV electron spin outperforms the bipartite entangled state of two electron spins by a factor of 1.4 due to control imperfections and dissipation during state preparation and readout. Each average consists in $1e4$ repetitions of the measurement sequence.

visibility of the interferometric signal is caused by coherent and incoherent sources of errors. Coherent sources of errors are associated with the creation of unwanted coherence terms due to imperfect control pulses. Incoherent sources of errors are associated with dissipation due to imperfect decoupling from external sources of noise during control operations and sensing, as well as spin relaxation during the whole duration of the sensing protocol.

We quantify the performance of our method by computing the sensitivity, which measures the smallest change in amplitude that can be estimated with a finite amount of resources, e.g., the total number of measurements or the number of entangled quantum probes. The sensitivity to small variations in amplitude of the time-varying magnetic field b_0 is experimentally obtained by $\delta B = \sigma_N/dS_B$, where σ_N is the standard deviation of the measured signal after averaging the outcomes of a series of N measurements and dS_B is the maximum slope of the signal variation with b_0 [2].

The scaling of the sensitivity as a function of the number of averages is shown in Fig. 4-16 for a coherent superposition of states of the NV electron spin and for a bipartite entangled state between the NV electron spin and the first X electron spin, which was created from an initially polarized and unpolarized X electron spin. Recoupling the NV electron spin to the two hyperfine transitions of the first X electron spins increases the sensitivity over recoupling only one hyperfine transition of the first X electron spin. The coherent superposition of state on the NV electron spin performs better than the bipartite entangled state by a factor of 1.4.

The sensitivity can be increased by performing repetitive measurements of the electron spins, implementing numerically optimized pulses, and driving simultaneously multiple resonance transitions to reduce relaxation during the state preparation step.

4.3.5 Perform repetitive quantum measurements of electron spins

To increase the sensitivity of the interferometric signal obtained with entangled states of electron spins, we map the phase information acquired by the entangled state as a population difference onto the X electron spin and perform repetitive quantum measurements of the X electron spin [82] with the NV electron spin. These measurements take advantage of the X electron spins being stable under optical illumination.

We calibrate the repetitive readout sequence by measuring the increase in SNR on the estimate of the polarization of the X electron spin after initializing its quantum state with a cross-polarization sequence. We demonstrate a relative improvement in SNR by a factor of 1.6 after $M = 32$ repetitions (Fig. 4-17).

The cumulative weighted signal after M repetitions of the quantum measurement (signal) and its associated statistical error (noise) are given by [82]

$$S_M = \sum_{m=1}^{M} w_m \, |S_m| \tag{4.71}$$

$$\sigma_M = \sqrt{\sum_{m=1}^{M} w_m^2 \sigma_m^2}, \tag{4.72}$$

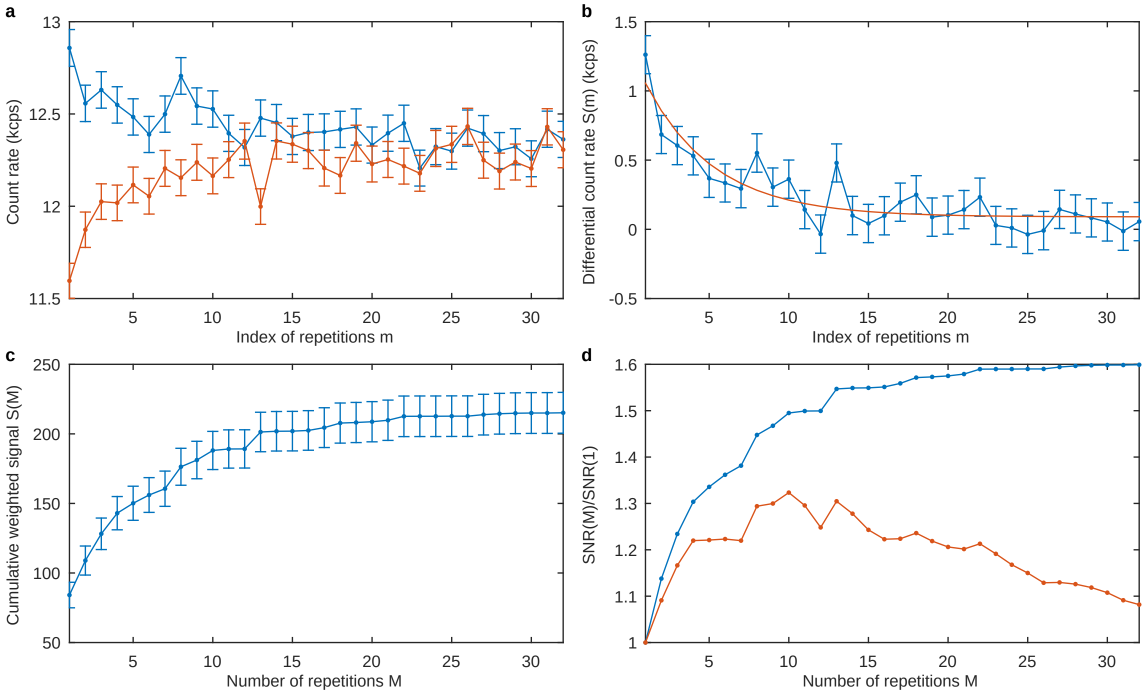

Figure 4-17: **Perform repetitive quantum measurements of the polarization of the first X electron spin.** **a**, Fluorescence signal for each repetition measured after a series of repetitive quantum measurements of the X electron spin with the NV electron spin measured along $\pm S_z$. **b**, Differential signal for each repetition obtained after computing the difference of the two fluorescence curves. The solid line is a fit to a decaying exponential function with half-life equal to $m = 3.0$. **c**, Cumulative weighted signal computed for an increasing number of repetitions. The figure of merit is the SNR, which corresponds to the ratio between the signal and its standard deviation (noise). **d**, Improvement in SNR over a single repetition for an increasing number of repetitions computed for the weighted signal (blue) and the unweighted signal (red). Assigning a lower weight to realizations of the signal with a smaller SNR maximizes the SNR of the cumulative signal.

where the weights $w_m = |S_m|/\sigma_m^2$ are chosen so as to maximize the SNR,

$$\begin{aligned} \mathrm{SNR}(M) &= S_M/\sigma_M && (4.73)\\ &= \sqrt{\sum_{m=1}^{M} |S_m|/\sigma_m}^{\,2} . && (4.74) \end{aligned}$$

The signal decreases exponentially with the number of repetitions with a decay rate equal to $\lambda = 0.23$, which correspond to a half-life of $m_{1/2} = \log 2/\lambda = 3.0$. The decrease in signal is attributed to the depolarization of the X electron spin after repeating the quantum measurement. Possible mechanisms for depolarization of electron spins during repetitive measurements are imperfect control pulses converting population of the X electron spin into single-spin coherences that is dissipated under free evolution, imperfect recoupling sequences converting population of the X electron spin into two-spin coherences that is dissipated under projective measurements on the NV electron spin, light-induced photoionization of the paramagnetic center, incoherent spin flips of the X nuclear spin, homonuclear spin diffusion with weakly coupled electron spins of the same species and spin-lattice relaxation.

To confirm the proper conversion and storage of coherence into population onto the X electron spin, we create an entangled state of two electron spins and performed a tomographic measurement of the quantum state assisted with repetitive measurements of the electron spins. Figure 4-18 shows a relative increase in the spectral power (area under the spectral peak) by 4.05 for $M = 4$ repetitions.

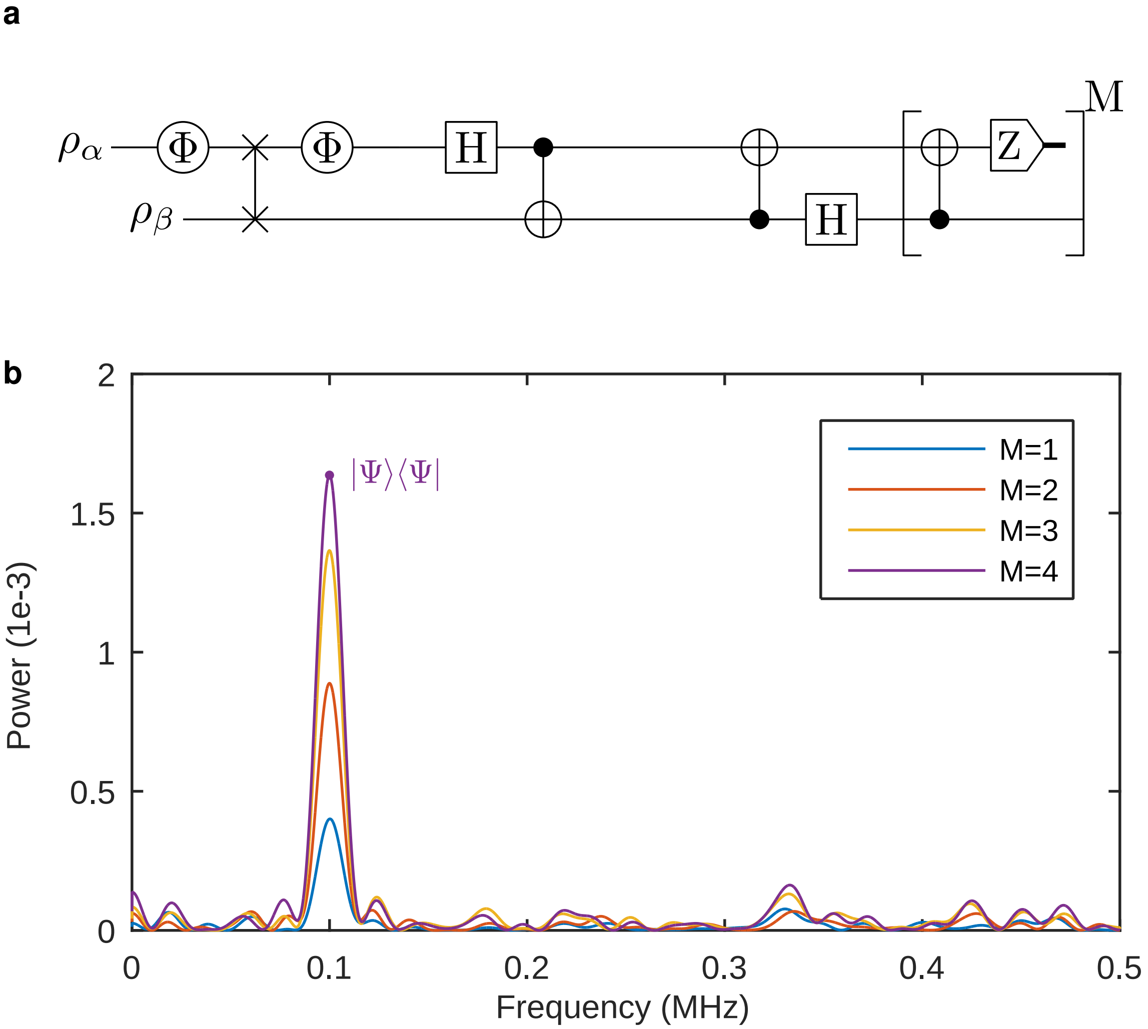

Figure 4-18: **Perform repetitive quantum measurements of the coherence stored in the bipartite entangled state formed by the NV electron spin and the first X electron spin.** **a**, Quantum circuit to initialize, entangle, disentangle, and repetitively measure the bipartite quantum system of two electron spins. **b**, Power spectrum of the cumulative weighted signal for up to $M = 4$ repetitions. The phases of the pulses of the disentangling gate are modulated at $\nu_\alpha = 250$ kHz and $\nu_\beta = 150$ kHz, such that the entangled state $|\Psi\rangle = (|01\rangle + |10\rangle)/\sqrt{2}$ produces a modulation at $\nu_\Delta = \nu_\alpha - \nu_\beta = 100$ kHz.

4.4 Conclusion and outlook

In conclusion, we introduced coherent control techniques to manipulate electron spins in diamond and experimentally demonstrated an approach to environment-assisted quantum sensing and quantum-enhanced metrology.

We first identified two hybrid-electron nuclear spin systems associated with unknown paramagnetic centers in the environment of a single nitrogen-vacancy center in diamond. We estimated the components of their hyperfine tensor by monitoring the change in the resonance frequencies of the esr spectrum as a function of the strength and orientation of the static magnetic field.The large hyperfine coupling strength enabled selectively addressing each hyperfine transitions and effectively protecting the electron spins against spin diffusion with free electrons. The nuclear spins will provide additional quantum resources for storing quantum information and assisting in implementing quantum protocols.

We then introduced magnetic double-resonance techniques to initialize, manipulate, and measure the quantum states of single electron spins through quantum control on the NV electron spin. Electron spins associated with unknown paramagnetic centers were initialized in a pure state using coherent feedback and cross-polarization in the rotating frame. The increase in polarization was measured by performing a quantum measurement on the electron spins with the NV electron spin acting as a quantum probe.

We further created entangled states of two and three electron spins between the NV electron spin and two X electron spins, taking advantage of our ability to efficiently initialize their quantum state using coherent feedback control techniques and cross-polarization techniques. These entangled states of two electron spins were used to detect time-varying magnetic fields, thus demonstrating an approach to environment-assisted quantum sensing. To increase the visibility of the interferometric signal obtained with entangled states, we implemented repetitive readout of the X electron spins, taking advantage of their stability under optical illumination.

Future work will exploit the nuclear spins associated with these paramagnetic centers as robust long-lived quantum registers (memories) suitable for storing quantum information, suppressing errors, and assisting in performing quantum logic operations [83, 84, 85].

Combining these spectroscopic techniques with the deterministic fabrication of spatially-confined ensembles of interacting electron spins in diamond will enable studying nonequilibrium dynamics in many-body correlated states of electron and nuclear spins at the atomic scale. Coherent control of interacting spins on discrete arrays embedded in photonics structures or combined with cold atomic systems will enable exploring fundamental ideas in quantum simulation of topological matter.

Chapter 5

Conclusion and outlook

In this thesis, we introduced and experimentally demonstrated coherent control techniques to initialize, manipulate, and measure the quantum state of single and multiple electron spins in diamond for applications in quantum information science and quantum sensing. We developed control sequences to modulate the evolution of electron spins and gain spectral information about time-varying fields and unknown quantum systems. We first showed how a series of time-inverting π pulses generate digital filters that are naturally described by Walsh functions, which form a complete basis of orthonormal functions suitable for sampling and reconstructing deterministic and stochastic time-varying fields with improved efficiency. We then showed how driving the resonant transitions of the spin environment enables identifying and converting unknown quantum systems into quantum resources useful for processing quantum information and sensing time-varying fields with improved efficiency, e.g., by creating entangled states of many electron spins. Scaling up the size of quantum systems by integrating quantum resources from the environment of a quantum probe is a promising approach to improve the performance of quantum sensors when deterministically fabricating an ensemble of interacting quantum probes is prohibitively difficult.

We first introduced in Chapter 2 and Chapter 3 the Walsh reconstruction method to reconstruct the temporal profile of deterministic fields and perform spectral measurements of stochastic fields with a single quantum probe. This method provides a general framework for quantum parameter estimation, e.g., to identify control sequences that provide the best performance in terms of information extraction vs. noise suppression and design sampling strategies that maximize the information extracted during each sampling step. The Walsh reconstruction method can be generalized to sample higher cumulants of the probability distribution associated with non-gaussian stochastic processes or probe the dynamics of multipartite quantum systems. Practical applications of this method include measuring action potentials at the level of single neurons, characterizing the transmission properties of microwave structures, or studying the many-body dynamics of ensembles of interacting spins.

We then located and identified in Chapter 4 two hybrid electron-nuclear spin systems in the environment of a single NV center by measuring the dipolar coupling constant and the hyperfine spectrum for different values of the strength and orientation of the static magnetic field. Performing quantum measurements on these two hybrid electron-nuclear spin systems made it possible to initialize and measure their quantum state using the NV center as an auxiliary quantum system. We finally created entangled states of two and three electron spins to measure the amplitude of time-varying magnetic fields with improved sensitivity. We showed that repetitive measurements of the electron spins provide a gain in signal-to-noise that is greater than the loss caused by imperfections in state preparation and readout. Combining these techniques will provide the gain in sensitivity needed to demonstrate quantum-enhanced magnetic sensing with quantum probes in solid-state materials.

Perfoming quantum measurements on the nuclear spins using electron-nuclear double-resonance sequences will enable identifying the gyromagnetic ratio of the nuclear spin and improving the estimates of the hyperfine components. Measuring the hyperfine spectrum for additional orientations of the external magnetic fields will shine light on the possible existence of a third paramagnetic center in the vicinity of a single NV center, which may be useful in creating quadripartite entangled states of electron spins and implementing quantum algorithms with spin systems of higher dimension. Characterizing the physical properties of these unknown defects, including their physical structure and photoionization properties, will facilitate modeling their dynamics and fabricating similar defects on demand. In addition, the efficiency of the initialization process, especially in systems requiring repetitive polarization injection steps, will be improved by implementing entangling gates, adiabatic operations and driving protocols with shortcuts to adiabaticity, and algorithmic cooling techniques.

Future work will focus on creating hybrid electron-nuclear spin systems of increasing dimension to study spin diffusion and non-equilibrium dynamics in many-body interacting spin systems, explore the limits on the efficiency of cooling quantum systems, and implement novel strategies for improving the sensitivity of quantum sensors for applications in quantum information science and quantum sensing.

Bibliography

[1] J. M. Taylor, P. Cappellaro, L. Childress, L. Jiang, D. Budker, P. R. Hemmer, A. Yacoby, R. Walsworth, and M. D. Lukin. High-sensitivity diamond magnetometer with nanoscale resolution. *Nat Phys.*, 4(10):810–816, 2008.

[2] J. R. Maze, P. L. Stanwix, J. S. Hodges, S. Hong, J. M. Taylor, P. Cappellaro, L. Jiang, A.S. Zibrov, A. Yacoby, R. Walsworth, and M. D. Lukin. Nanoscale magnetic sensing with an individual electronic spin qubit in diamond. *Nature*, 455:644–647, 2008.

[3] Gopalakrishnan Balasubramanian, I Y Chan, Roman Kolesov, Mohannad Al-Hmoud, Julia Tisler, Chang Shin, Changdong Kim, Aleksander Wojcik, Philip R Hemmer, Anke Krueger, Tobias Hanke, Alfred Leitenstorfer, Rudolf Bratschitsch, Fedor Jelezko, and Jörg Wrachtrup. Nanoscale imaging magnetometry with diamond spins under ambient conditions. *Nature*, 455(7213):648–51, October 2008.

[4] F. Dolde, H. Fedder, M. W. Doherty, T. Nobauer, F. Rempp, G. Balasubramanian, T. Wolf, F. Reinhard, L. C. L. Hollenberg, F. Jelezko, and J. Wrachtrup. Electric-field sensing using single diamond spins. *Nat Phys*, 7(6):459–463, June 2011.

[5] David M Toyli, Charles F de Las Casas, David J Christle, Viatcheslav V Dobrovitski, and David D Awschalom. Fluorescence thermometry enhanced by the quantum coherence of single spins in diamond. *Proceedings of the National Academy of Sciences of the United States of America*, 110(21):8417–8421, May 2013.

[6] G Kucsko, P C Maurer, N Y Yao, M Kubo, H J Noh, P K Lo, H Park, and M D Lukin. Nanometre-scale thermometry in a living cell. *Nature*, 500(7460):54–8, August 2013.

[7] P. Neumann, I. Jakobi, F. Dolde, C. Burk, R. Reuter, G. Waldherr, J. Honert, T. Wolf, A. Brunner, J. H. Shim, D. Suter, H. Sumiya, J. Isoya, and J. Wrachtrup. High-precision nanoscale temperature sensing using single defects in diamond. *Nano Letters*, 13(6):2738–2742, 2013.

[8] Yi-Ren Chang, Hsu-Yang Lee, Kowa Chen, Chun-Chieh Chang, Dung-Sheng Tsai, Chi-Cheng Fu, Tsong-Shin Lim, Yan-Kai Tzeng, Chia-Yi Fang, Chau-

Chung Han, Huan-Cheng Chang, and Wunshain Fann. Mass production and dynamic imaging of fluorescent nanodiamonds. *Nat Nano*, 3(5):284–8, May 2008.

[9] L. P. McGuinness, Y. Yan, A. Stacey, D. A. Simpson, L. T. Hall, D. Maclaurin, S. Prawer, P. Mulvaney, J. Wrachtrup, F. Caruso, R. E. Scholten, and L. C. L. Hollenberg. Quantum measurement and orientation tracking of fluorescent nanodiamonds inside living cells. *Nat Nano*, 6(6):358–363, 2011.

[10] D Le Sage, K Arai, D R Glenn, S J DeVience, L M Pham, L Rahn-Lee, M D Lukin, A Yacoby, A Komeili, and R L Walsworth. Optical magnetic imaging of living cells. *Nature*, 496(7446):486–9, April 2013.

[11] Vadym N Mochalin, Olga Shenderova, Dean Ho, and Yury Gogotsi. The properties and applications of nanodiamonds. *Nat Nano*, 7(1):11–23, January 2012.

[12] Viva R Horowitz, Benjamín J Alemán, David J Christle, Andrew N Cleland, and David D Awschalom. Electron spin resonance of nitrogen-vacancy centers in opticallytrapped nanodiamonds. *Proc. Nat Acad. Sc.*, 109(34):13493–13497, August 2012.

[13] Michael Geiselmann, Mathieu L Juan, Jan Renger, Jana M Say, Louise J Brown, F Javier García de Abajo, Frank Koppens, and Romain Quidant. Three-dimensional optical manipulation of a single electron spin. *Nat Nano*, 8(3):175–179, February 2013.

[14] Gopalakrishnan Balasubramanian, Philipp Neumann, Daniel Twitchen, Matthew Markham, Roman Kolesov, Norikazu Mizuochi, Junichi Isoya, Jocelyn Achard, Johannes Beck, Julia Tissler, Vincent Jacques, Philip R. Hemmer, Fedor Jelezko, and Jorg Wrachtrup. Ultralong spin coherence time in isotopically engineered diamond. *Nat Mater*, 8(5):383–387, 2009.

[15] A. Cooper, E. Magesan, H. N. Yum, and P. Cappellaro. Time-resolved magnetic sensing with electronic spins in diamond. *Nat Commun*, 5, Jan 2014. Article.

[16] Easwar Magesan, Alexandre Cooper, Honam Yum, and Paola Cappellaro. Reconstructing the profile of time-varying magnetic fields with quantum sensors. *Phys. Rev. A*, 88(3):032107, September 2013.

[17] Easwar Magesan, Alexandre Cooper, and Paola Cappellaro. Compressing measurements in quantum dynamic parameter estimation. August 2013.

[18] H. Y. Carr and E. M. Purcell. Effects of diffusion on free precession in nuclear magnetic resonance experiments. *Phys. Rev.*, 94(3):630–638, 1954.

[19] K. Khodjasteh and D. A. Lidar. Fault-tolerant quantum dynamical decoupling. *Phys. Rev. Lett.*, 95(18):180501, 2005.

[20] Vittorio Giovannetti, Seth Lloyd, and Lorenzo Maccone. Advances in quantum metrology. *Nat Photon*, 5(4):222–229, 2011.

[21] L. T. Hall, G. C. G. Beart, E. A. Thomas, D. A. Simpson, L. P. McGuinness, J. H. Cole, J. H. Manton, R. E. Scholten, F. Jelezko, JÃűrg Wrachtrup, S. Petrou, and L. C. L. Hollenberg. High spatial and temporal resolution wide-field imaging of neuron activity using quantum nv-diamond. *Sci. Rep.*, 2:–, May 2012.

[22] L. Viola and S. Lloyd. Dynamical suppression of decoherence in two-state quantum systems. *Phys. Rev. A*, 58:2733, 1998.

[23] C. A. Ryan, J. S. Hodges, and D. G. Cory. Robust decoupling techniques to extend quantum coherence in diamond. *Phys. Rev. Lett.*, 105(20):200402, 2010.

[24] Boris Naydenov, Florian Dolde, Liam T. Hall, Chang Shin, Helmut Fedder, Lloyd C. L. Hollenberg, Fedor Jelezko, and Jörg Wrachtrup. Dynamical decoupling of a single-electron spin at room temperature. *Phys. Rev. B*, 83:081201, 2011.

[25] G. de Lange, D. Ristè, V. V. Dobrovitski, and R. Hanson. Single-spin magnetometry with multipulse sensing sequences. *Phys. Rev. Lett.*, 106:080802, Feb 2011.

[26] Masashi Hirose, Clarice D. Aiello, and Paola Cappellaro. Continuous dynamical decoupling magnetometry. *Phys. Rev. A*, 86:062320, Dec 2012.

[27] Jonas Bylander, Simon Gustavsson, Fei Yan, Fumiki Yoshihara, Khalil Harrabi, George Fitch, David G Cory, and William D Oliver. Noise spectroscopy through dynamical decoupling with a superconducting flux qubit. *Nat Physics*, 7:565–570, 2011.

[28] Gonzalo Álvarez and Dieter Suter. Measuring the spectrum of colored noise by dynamical decoupling. *Phys. Rev. Lett.*, 107(23), November 2011.

[29] N. Bar-Gill, L.M. Pham, C. Belthangady, D. Le Sage, P. Cappellaro, J.R. Maze, M.D. Lukin, A. Yacoby, and R. Walsworth. Suppression of spin-bath dynamics for improved coherence of multi-spin-qubit systems. *Nat Commun.*, 3:858, 2012.

[30] Shlomi Kotler, Nitzan Akerman, Yinnon Glickman, Anna Keselman, and Roee Ozeri. Single-ion quantum lock-in amplifier. *Nature*, 473(7345):61–65, 2011.

[31] J. L. Walsh. A closed set of normal orthogonal functions. *Amer. J. Math.*, 45(1):5–24, 1923.

[32] Emmanuel J. Candés, Justin K. Romberg, and Terence Tao. Stable signal recovery from incomplete and inaccurate measurements. *Comm. Pure App. Math.*, 59(8):1207–1223, 2006.

[33] Rolf Simon Schoenfeld and Wolfgang Harneit. Real time magnetic field sensing and imaging using a single spin in diamond. *Phys. Rev. Lett.*, 106:030802, 2011.

[34] A. Dreau, M. Lesik, L. Rondin, P. Spinicelli, O. Arcizet, J.-F. Roch, and Jacques V. Avoiding power broadening in optically detected magnetic resonance of single nv defects for enhanced dc magnetic field sensitivity. *Phys. Rev. B*, 84:195204, 2011.

[35] David Hayes, Kaveh Khodjasteh, Lorenza Viola, and Michael J. Biercuk. Reducing sequencing complexity in dynamical quantum error suppression by walsh modulation. *Phys. Rev. A*, 84:062323, 2011.

[36] Kaveh Khodjasteh, Jarrah Sastrawan, David Hayes, Todd J. Green, Michael J. Biercuk, and Lorenza Viola. Designing a practical high-fidelity long-time quantum memory. *Nat Commun*, 4, Jun 2013. Article.

[37] F. Schipp, W.R. Wade, and P. Simon. *Walsh series: an introduction to the dyadic harmonic analysis*. Adam Hilger, 1990.

[38] B.I. Golubov, A.V. Efimov, V.A. Skvortïÿăsïÿąov, and V. Skvortsov. *Walsh series and transforms: theory and applications*. Mathematics and its applications (Kluwer Academic Publishers).: Soviet series. Kluwer Academic Publishers, 1991.

[39] Lizann Bolinger and John S Leigh. Hadamard spectroscopic imaging (hsi) for multivolume localization. *Journal of Magnetic Resonance (1969)*, 80(1):162 – 167, 1988.

[40] ÄŠriks KupÄŊe and Ray Freeman. Two-dimensional hadamard spectroscopy. *Journal of Magnetic Resonance*, 162(2):300 – 310, 2003.

[41] Assaf Tal and Lucio Frydman. Single-scan multidimensional magnetic resonance. *Progress in Nuclear Magnetic Resonance Spectroscopy*, 57(3):241 – 292, 2010.

[42] Clarice D. Aiello, Masashi Hirose, and Paola Cappellaro. Composite-pulse magnetometry with a solid-state quantum sensor. *Nat Commun*, 4:1419–, January 2013.

[43] Mankei Tsang, Howard M. Wiseman, and Carlton M. Caves. Fundamental quantum limit to waveform estimation. *Phys. Rev. Lett.*, 106:090401, Mar 2011.

[44] D. Le Sage, L. M. Pham, N. Bar-Gill, C. Belthangady, M. D. Lukin, A. Yacoby, and R. L. Walsworth. Efficient photon detection from color centers in a diamond optical waveguide. *Phys. Rev. B*, 85:121202, 2012.

[45] J. Wikswo, J. Barach, and J. Freeman. Magnetic field of a nerve impulse: first measurements. *Science*, 208(4439):53–55, April 1980.

[46] Henrik Alle, Arnd Roth, and Jörg R P Geiger. Energy-efficient action potentials in hippocampal mossy fibers. *Science*, 325(5946):1405–8, 2009.

[47] Dominique Debanne. Information processing in the axon. *Nature reviews. Neuroscience*, 5(4):304–16, April 2004.

[48] K. R. Swinney and J. P. Wikswo. A calculation of the magnetic field of a nerve action potential. *Biophysical Journal*, 32(2):719–31, November 1980.

[49] James K. Woosley, Bradley J. Roth, and John P. Wikswo. The magnetic field of a single axon: A volume conductor model. *Mathematical Biosciences*, 76(1):1–36, September 1985.

[50] Kenichi Ohno, F. Joseph Heremans, Lee C. Bassett, Bryan A. Myers, David M. Toyli, Ania C. Bleszynski Jayich, Christopher J. PalmstroÌÿm, and David D. Awschalom. Engineering shallow spins in diamond with nitrogen delta-doping. *Appl. Phys. Lett.*, 101(8):082413, August 2012.

[51] T. Staudacher, F. Ziem, L. Häussler, R. Stöhr, S. Steinert, F. Reinhard, J. Scharpf, A. Denisenko, and J. Wrachtrup. Enhancing the spin properties of shallow implanted nitrogen vacancy centers in diamond by epitaxial overgrowth. *Appl. Phys. Lett.*, 101(21):212401, 2012.

[52] T. Staudacher, F. Shi, S. Pezzagna, J. Meijer, J. Du, C. A. Meriles, F. Reinhard, and J. Wrachtrup. Nuclear magnetic resonance spectroscopy on a (5-nanometer)3 sample volume. *Science*, 339(6119):561–563, 2013.

[53] H. J. Mamin, M. Kim, M. H. Sherwood, C. T. Rettner, K. Ohno, D. D. Awschalom, and D. Rugar. Nanoscale nuclear magnetic resonance with a nitrogen-vacancy spin sensor. *Science*, 339(6119):557–560, 2013.

[54] L M Pham, D Le Sage, P L Stanwix, T K Yeung, D Glenn, A Trifonov, P Cappellaro, P R Hemmer, M D Lukin, H Park, A Yacoby, and R L Walsworth. Magnetic field imaging with nitrogen-vacancy ensembles. *New J. Phys.*, 13(4):045021, April 2011.

[55] William F. Koehl, Bob B. Buckley, F. Joseph Heremans, Greg Calusine, and David D. Awschalom. Room temperature coherent control of defect spin qubits in silicon carbide. *Nature*, 479(7371):84–87, Nov 2011.

[56] Jarryd J. Pla, Kuan Y. Tan, Juan P. Dehollain, Wee H. Lim, John J. L. Morton, Floris A. Zwanenburg, David N. Jamieson, Andrew S. Dzurak, and Andrea Morello. High-fidelity readout and control of a nuclear spin qubit in silicon. *Nature*, 496(7445):334–338, Apr 2013. Letter.

[57] Kristiaan De Greve, Peter L. McMahon, David Press, Thaddeus D. Ladd, Dirk Bisping, Christian Schneider, Martin Kamp, Lukas Worschech, Sven Hofling, Alfred Forchel, and Yoshihisa Yamamoto. Ultrafast coherent control and suppressed nuclear feedback of a single quantum dot hole qubit. *Nat Phys*, 7(11):872–878, Nov 2011.

[58] B Van Waeyenberge, A Puzic, H Stoll, K W Chou, T Tyliszczak, R Hertel, M Fähnle, H Brückl, K Rott, G Reiss, I Neudecker, D Weiss, C H Back, and G Schütz. Magnetic vortex core reversal by excitation with short bursts of an alternating field. *Nature*, 444(7118):461–4, November 2006.

[59] V. Uhlir, M. Urbanek, L. Hladik, J. Spousta, M-Y. Im, P. Fischer, N. Eibagi, J. J., Kan, E. E., Fullerton, and T. Sikola. Dynamic switching of the spin circulation in tapered magnetic nanodisks. *Nat Nano*, 8(5):341–346, May 2013.

[60] Michael J Biercuk, Hermann Uys, Aaron P VanDevender, Nobuyasu Shiga, Wayne M Itano, and John J Bollinger. Optimized dynamical decoupling in a model quantum memory. *Nature*, 458(7241):996–1000, April 2009.

[61] L. T. Hall, J. H. Cole, C. D. Hill, and L. C. L. Hollenberg. Sensing of fluctuating nanoscale magnetic fields using nitrogen-vacancy centers in diamond. *Phys. Rev. Lett.*, 103:220802, Nov 2009.

[62] Liam T Hall, Charles D Hill, Jared H Cole, Brigitte Städler, Frank Caruso, Paul Mulvaney, Jörg Wrachtrup, and Lloyd C L Hollenberg. Monitoring ion-channel function in real time through quantum decoherence. *Proc. Nat Acad. Sc.*, 107(44):18777–18782, November 2010.

[63] Jonathan Welch, Daniel Greenbaum, Sarah Mostame, and Alan Aspuru-Guzik. Efficient quantum circuits for diagonal unitaries without ancillas. *New Journal of Physics*, 16(3):033040, 2014.

[64] D. Hayes, S. M. Clark, S. Debnath, D. Hucul, I. V. Inlek, K. W. Lee, Q. Quraishi, and C. Monroe. Coherent error suppression in multiqubit entangling gates. *Phys. Rev. Lett.*, 109(2):020503, July 2012.

[65] L. Marseglia, J. P. Hadden, A. C. Stanley-Clarke, J. P. Harrison, B. Patton, Y.-L. D. Ho, B. Naydenov, F. Jelezko, J. Meijer, P. R. Dolan, J. M. Smith, J. G. Rarity, and J. L. O'Brien. Nanofabricated solid immersion lenses registered to single emitters in diamond. *Appl. Phys. Lett.*, 98(13):133107, 2011.

[66] N. Bar-Gill, L.M. Pham, A. Jarmola, D. Budker, and R.L. Walsworth. Solid-state electronic spin coherence time approaching one second. *Nature Communications*, 4:1743, April 2013.

[67] Jacob T Robinson, Marsela Jorgolli, Alex K Shalek, Myung-Han Yoon, Rona S Gertner, and Hongkun Park. Vertical nanowire electrode arrays as a scalable platform for intracellular interfacing to neuronal circuits. *Nature Nanotechnology*, 7(3):180–4, March 2012.

[68] J. E. Gibbs and H. A. Gebbie. Application of walsh functions to transform spectroscopy. *Nature*, 224(5223):1012–1013, December 1969.

[69] G. Robinson. Logical convolution and discrete walsh and fourier power spectra. *IEEE Transactions on Audio and Electroacoustics*, 20(4):271–280, Oct 1972.

[70] J. E. Gibbs and F. R. Pichler. Comments on transformation of "fourier" power spectra into "walsh" power spectra. *IEEE Transactions on Electromagnetic Compatibility*, EMC-13(3):51–54, Aug 1971.

[71] M. Gulamhusein and F. Fallside. Short-time spectral and autocorrelation analysis in the walsh domain. *IEEE Trans. Inf. Theor.*, 19(5):615–623, September 1973.

[72] Kevin C. Young and K. Birgitta Whaley. Qubits as spectrometers of dephasing noise. *Phys. Rev. A*, 86:012314, 2012.

[73] P. Lopresti and H. Suri. A fast algorithm for the estimation of autocorrelation functions. *IEEE Transactions on Acoustics, Speech, and Signal Processing*, 22(6):449–453, Dec 1974.

[74] P. Cappellaro, L. Jiang, J. S. Hodges, and M. D. Lukin. Coherence and control of quantum registers based on electronic spin in a nuclear spin bath. *Phys. Rev. Lett.*, 102(21):210502, 2009.

[75] G. Goldstein, P. Cappellaro, J. R. Maze, J. S. Hodges, L. Jiang, A. S. Sørensen, and M. D. Lukin. Environment assisted precision measurement. *Phys. Rev. Lett.*, 106(14):140502, 2011.

[76] Arthur Schweiger and Gunnar Jeschke. *Principles of Pulse Electron Paramagnetic Resonance*. Oxford University Press, 2001.

[77] Kurt Jacobs. *Quantum Measurement Theory and its Applications*. Cambridge University Press, 2014.

[78] Leonard J. Schulman, Tal Mor, and Yossi Weinstein. Physical limits of heat-bath algorithmic cooling. *Phys. Rev. Lett.*, 94(12):120501, 2005.

[79] Shlomi Kotler, Nitzan Akerman, Nir Navon, Yinnon Glickman, and Roee Ozeri. Measurement of the magnetic interaction between two bound electrons of two separate ions. *Nature*, 510(7505):376–380, Jun 2014. Letter.

[80] D. Leibfried, M. D. Barrett, T. Schaetz, J. Britton, J. Chiaverini, W. M. Itano, J. D. Jost, C. Langer, and D. J. Wineland. Toward heisenberg-limited spectroscopy with multiparticle entangled states. *Science*, 304(5676):1476–1478, 2004.

[81] M. Mehring, J. Mende, and W. Scherer. Entanglement between an electron and a nuclear spin $\frac{1}{2}$. *Phys. Rev. Lett.*, 90:153001, Apr 2003.

[82] L. Jiang, J. S. Hodges, J. R. Maze, P. Maurer, J. M. Taylor, D. G. Cory, P. R. Hemmer, R. L. Walsworth, A. Yacoby, A. S. Zibrov, and M. D. Lukin. Repetitive readout of a single electronic spin via quantum logic with nuclear spin ancillae. *Science*, 326(5950):267–272, 2009.

[83] Masashi Hirose and Paola Cappellaro. Coherent feedback control of a single qubit in diamond. *Nature*, 532(7597):77–80, April 2016.

[84] E. M. Kessler, I. Lovchinsky, A. O. Sushkov, and M. D. Lukin. Quantum error correction for metrology. *Phys. Rev. Lett.*, 112:150802, Apr 2014.

[85] Thomas Unden, Priya Balasubramanian, Daniel Louzon, Yuval Vinkler, Martin B. Plenio, Matthew Markham, Daniel Twitchen, Alastair Stacey, Igor Lovchinsky, Alexander O. Sushkov, Mikhail D. Lukin, Alex Retzker, Boris Naydenov, Liam P. McGuinness, and Fedor Jelezko. Quantum metrology enhanced by repetitive quantum error correction. *Phys. Rev. Lett.*, 116:230502, Jun 2016.